

POLITECNICO DI TORINO

**MASTER OF SCIENCE Degree in
ELECTRONIC ENGINEERING**



MASTER OF SCIENCE Degree Thesis

**LoRa®Enabled IoT Node With
Integrated PCB Antenna**

Supervisors

Prof. Daniele TRINCHERO

Dr. Giovanni COLUCCI

Ing. Elena FILIPESCU

Candidate

JUAN CAMILO MORA ZOPPI

APRIL 2023

Summary

This thesis describes the design, test, and validation of a LoRa enabled IoT sensor node that interfaces with The Thing's Network to track meteorological conditions for agricultural applications. The sensor node is a portable weatherproof modular weather station that can be connected to up to six different weather sensors, acquire and process the sensor data, and transmit the results at 868 MHz using the LoRaWAN protocol. This PCB uses the Murata 1SJ LoRa module, exploiting its low power characteristics to be able to be battery powered and deployable anywhere. The proposed design is an evolution of a previous version, where the PCB was connected to an external antenna to transmit the data, which meant hardware assembly complications to accommodate the antenna while maintaining the system weatherproof, and increased costs due to the need of one antenna and one pigtail for each sensor node. For this reason, a planar inverted F antenna was integrated into the sensor node's PCB. The sensor node was then fabricated, assembled, tested, and validated to verify its functionality and capability to be deployed as a product.

Acknowledgements

The past eight years have been an eye-opening experience, dedicated to completing my education as an electronic engineer. This path started in middle school when I programmed my first Lego NXT robot and fell in love with how I could express my creativity through electronics. As I write this, I realize that this road is coming to an end, and can look back and remember key figures along the way that I would like to thank for making me the engineer that I am today.

First of all, I would like to thank prof. Daniele Trincherò and the entirety of the iXem Labs team for welcoming me. The challenge set by professor Trincherò to go beyond my comfort zone and immerse myself in radio-frequency was a great experience. I learned so much during the development of this thesis and overcoming it fills me with confidence for the future.

I would also like to thank engineer Gianluca Dassano, the PoliTo's anechoic chamber technician, and prof. Riccardo Maggiora for giving me access to their CST Studio license, as without them, this thesis would not have been possible

My gratitude also goes to the Pontificia Universidad Javeriana, my home University, which allowed me to do this double degree in PoliTo, and specially Prof. Juan Carlos Giraldo for teaching me the value of being an engineer and giving 110% in all of my projects, and professors Yahmure, Perilla, and Melchior for teaching me the basics of electronic design and polishing my skills as a hardware designer.

Last but not least, I would like to express my gratitude to the people dearest to me. My family, for all of their love and help through the years. My girlfriend, Natalia, who supported me when the road became harsh. Finally, and most importantly, I would like to thank my parents, who have done even the impossible to give me the opportunities that led to me being here today.

Thanks to every single one of you for being a part of this journey and the lasting effects you've had on my path.

Table of Contents

List of Tables	VII
List of Figures	VIII
Acronyms	XIII
1 Introduction	1
1.1 iXem Wine	2
1.2 An Introduction to LoRa®	2
1.3 An Introduction to The Things Network	3
1.4 State of the Art of the iXem Wine Project	4
1.4.1 Compatible sensors	5
1.4.2 Shortcomings	6
1.5 Project Requirements and Research Objectives	7
1.6 Structure	9
2 Background	11
2.1 A deeper dive into the LoRaWAN® protocol and regional regulations	12
2.1.1 The LoRa® Modulation Technique	12
2.1.2 EU868	17
2.2 Working Principle of PCB Antennas	21
2.2.1 What is an Antenna?	21
2.2.2 Main Antenna Topologies	23
2.2.3 Making Antennas Planar	28
2.3 Product-Specific Hardware Requirements	31
3 Research and Development Methodology	32
4 Design of PCB Antennas for LoRa EU868	35
4.1 Validation of CST Studio as an antenna CAD and simulation tool .	36
4.2 Planar dipole antenna with Balun	41

4.3	Planar monopole antenna	50
4.4	Offset planar monopole antenna	54
4.5	Planar inverted-L antenna	58
4.6	Planar bent inverted-L antenna	63
4.7	Planar inverted-F antenna	66
5	Validation of Designed PCB Antennas	71
5.1	Planar dipole antenna	72
5.2	Planar monopole antenna	77
5.3	Planar inverted-L antenna	80
5.4	Planar inverted-F antenna	83
5.5	PCB Chip antenna	86
5.6	Choosing the antenna topology for the sensor node PCB	89
6	Mechanical Design of the sensor node enclosure	91
7	Design of the Sensor Node PCB	95
7.1	Definition of the board outline	95
7.2	Definition of the PCB Antenna's Footprint	97
7.3	Creation of PCB Schematics	99
7.4	Design of the PCB	100
8	Validation of the Sensor Node	102
8.1	Anechoic chamber testing	102
8.2	Lab tests without enclosure	104
8.3	Field test	107
9	Conclusions and Future Work	109
9.1	Conclusions	109
9.2	Improvement opportunities	111
A	Matlab code: generate radiation pattern from anechoic chamber data	112
B	Radiation patterns: Cartesian representation	122
C	Sensor node PCB schematics and BOM	127
	Bibliography	130

List of Tables

1.1	List of iXem Wine compatible sensors	6
4.1	Dimensions of 2.4 GHz antenna with Balun	44
4.2	Dimensions of 868 MHz antenna with Balun	48
4.3	Dimensions of initial Monopole antenna	50
4.4	Dimensions of optimized Monopole antenna	52
4.5	Dimensions of optimized offset Monopole antenna	55
4.6	Dimensions of initial inverted-L antenna	58
4.7	Dimensions of modified inverted-L antenna	60
4.8	Dimensions of initial bent inverted-L antenna	63
4.9	Dimensions of initial bent inverted-L antenna	64
4.10	Dimensions of optimized inverted-F antenna	67
7.1	Dimensions of PCB inverted-F antenna	97
8.1	Comparison of SNR and RSSI of external and integrated antenna	108

List of Figures

1.1	LoRa®: Technological gap filled	3
1.2	Current generation of sensor node PCB	5
2.1	Example of BPSK modulation format	12
2.2	Constellation diagram of 8-PSK modulation	13
2.3	Chirp waveform	13
2.4	Frequency and time visualization of symbol 33 of SF7	14
2.5	Spectrogram view of a LoRa transmission	14
2.6	LoRa®: SNR for different Spreading Factors	15
2.7	LoRa® packet format	16
2.8	Spectrogram view of a LoRa® packet	16
2.9	Default channels for the EU868 regional parameter	18
2.10	Bit Rates for different Data Rate categories in EU868	19
2.11	EIRP values allowed by TTN in EU868	20
2.12	Maximum payload size in EU868 for different data rates	20
2.13	Two Wire Transmission Line	23
2.14	Flared transmission line	24
2.15	Two wire dipole	24
2.16	3D radiation pattern of a $\lambda/2$ dipole	25
2.17	Quarter-wave monopole antenna and equivalent dipole	26
2.18	Omnidirectional wire antenna topologies	27
2.19	Loop and Hoop antennas	28
2.20	Planar Dipole Antenna	28
2.21	Planar Monopole Antenna	29
2.22	Planar antennas	30
2.23	Other planar antennas	30
2.24	IP Rating Table	31
4.1	Dimensions of a Half wavelength dipole	36
4.2	Half wavelength dipole in CST Studio	37
4.3	Port for half wavelength dipole	37

4.4	Simulation results of Wire dipole antenna	38
4.5	Simulated radiation pattern of wire dipole antenna	39
4.6	Simple planar dipole antenna	40
4.7	S_{11} of simple planar dipole antenna	40
4.8	S_{11} of optimized simple planar dipole antenna	41
4.9	Initial geometry of printed dipole antenna with Balun	42
4.10	Dimensions of initial dipole antenna with Balun	42
4.11	Initial geometry: 2.4 GHz antenna with Balun	43
4.12	Simulation results of 2.4 GHz dipole antenna with Balun	45
4.13	Simulated radiation pattern of 2.4 GHz dipole antenna with Balun	46
4.14	Optimized 868 MHz antenna with Balun	47
4.15	Simulation results of planar dipole antenna with balun	49
4.16	Simulated radiation pattern of planar dipole antenna with Balun	50
4.17	Planar monopole antenna	51
4.18	Simulation results of initial planar monopole antenna	51
4.19	Simulation results of optimized planar monopole antenna	52
4.20	Simulated radiation pattern of planar monopole antenna	53
4.21	Offset planar monopole antenna	54
4.22	Simulation results of initial planar monopole antenna	55
4.23	Simulation results of optimized offset monopole antenna	56
4.24	Simulated radiation pattern of offset monopole antenna	57
4.25	Initial planar inverted-L antenna	58
4.26	Simulation results of initial planar monopole antenna	59
4.27	Modified planar inverted-L antenna	60
4.28	Simulation results of optimized inverted-L antenna	61
4.29	Simulated radiation pattern of inverted-L antenna	62
4.30	Bent inverted-L antenna	63
4.31	Simulation results of initial bent inverted-L antenna	64
4.32	Simulation results of bent inverted-L antenna	65
4.33	Smith chart of simulated bent inverted-L antenna	66
4.34	Inverted-F topology and equivalent circuit	67
4.35	Optimized inverted-F antenna	68
4.36	Simulation results of optimized inverted-F antenna	69
4.37	Simulated radiation pattern of inverted-F antenna	70
5.1	PCB Design: Dipole Antenna with Balun	73
5.2	PCB Design: Dipole Antenna with Balun	74
5.3	Test setup: Dipole Antenna with Balun	74
5.4	S_{11} of Dipole antenna with Balun	75
5.5	Simulated S_{11} of Dipole antenna with cutouts	76
5.6	Approximate 3D radiation pattern of Dipole antenna with Balun	76

5.7	Radiation pattern cuts of Dipole antenna with Balun	77
5.8	PCB Design: Monopole Antenna	77
5.9	PCB Design: Monopole Antenna	78
5.10	Test setup: Monopole Antenna	78
5.11	S_{11} of Monopole Antenna	79
5.12	Radiation pattern cuts of Monopole Antenna	79
5.13	Approximate 3D radiation pattern of Monopole Antenna	80
5.14	PCB Design: Inverted-L Antenna	80
5.15	PCB Design: Inverted-L Antenna	81
5.16	Test setup: Inverted-L Antenna	81
5.17	S_{11} of Inverted-L Antenna	82
5.18	Radiation pattern cuts of Inverted-L Antenna	82
5.19	Approximate 3D radiation pattern of Inverted-L Antenna	83
5.20	PCB Design: Inverted-F Antenna	83
5.21	PCB Design: Inverted-F Antenna	84
5.22	Test setup: Inverted-F Antenna	84
5.23	S_{11} of Inverted-F Antenna	85
5.24	Radiation pattern cuts of Inverted-F Antenna	85
5.25	Approximate 3D radiation pattern of Inverted-F Antenna	86
5.26	PCB Design: Chip Antenna	86
5.27	PCB Design: Chip Antenna	87
5.28	Test setup: Chip Antenna	88
5.29	S_{11} of Chip Antenna	88
5.30	Radiation pattern cuts of Monopole Antenna	89
5.31	Approximate 3D radiation pattern of Inverted-F Antenna	89
6.1	Proposed connection interface	91
6.2	Female terminal mounting method of metric connector	92
6.3	Spelsberg TK PC 1309-6-tm enclosure	93
6.4	Male terminal mounting method of metric connector	94
7.1	Technical drawing of Spelsberg TK PC 1309-6-tm enclosure	96
7.2	Board shape for sensor node PCB	96
7.3	4 layer board stackup in CST Studio of the sensor node PCB	97
7.4	Simulation results of PCB inverted-F antenna	98
7.5	Antenna PCB component in Altium	99
7.6	Sensor node PCB design	100
7.7	Sensor node PCB after manufacturing and assembly	101
8.1	Test setup: Full PCB with inverted-F antenna	103
8.2	S_{11} of Sensor Node PCB	103
8.3	Approximate 3D radiation pattern of Sensor Node PCB	104

8.4	Radiation pattern cuts of Dipole antenna with Balun	104
8.5	Initial Test: Setup	105
8.6	Initial Test: Results	106
8.7	Field Test: Setup	107
8.8	Field Test: Results	108

Acronyms

IoT

Internet of Things

LPWAN

Low Power Wide Area Network

FOTA

Firmware Over the Air

TTN

The Things Network

TTS

The Things Stack

PCB

Printed Circuit Board

Chapter 1

Introduction

Culturally, wine in Italy is one of the most important, if not the most important, products, being a source of pride throughout the country. It is so intertwined in Italian culture that it is not only a drink, but also a reflection of the ethical and aesthetic values, culture, and traditions of the people that make it. This all starts in the vineyard. As Giacomo Tachis described, "the territory is a collection of wine components and its image: quality of the terrain, weather, exposure of the vineyard, tradition, myth, agriculture, and culture of the winemaker" [1, Giacomo Tachis]. As such, the care of the grape vine, maintaining it at its optimal conditions throughout its life cycle, is not only important for the characteristics of the final product, but also as evidence of the winegrower's patience, diligence, and power of observation.

Knowing the cultural importance of the vineyard and correctly identifying its conditions, the iXem Wine project was born as a way to bring the technological advantages of the Internet of Things (IoT) into the (literal) hands of wine producers throughout Italy to improve their agency over their vineyards, and ultimately, the quality of their product.

We live in an age where information surrounds us. We wake up every day, grab our smartphones and suddenly we have an astounding amount of data at our fingertips: the weather forecast for the day, news from around the globe, unlimited amounts of entertainment. The integration of the Internet of Things into daily life has increased the amount of control we have over our lives. Smart rings with biometric sensors that track our sleep patterns, smart fridges that make our shopping lists for us, doorbells with cameras that can be answered from across the globe, and many more. As such, the iXem project aims to take advantage of the increased ease of access to data to help wine growers.

1.1 iXem Wine

iXem Wine [2] is being developed in Turin, Italy by iXem Labs, a research group established in 2004 at Politecnico di Torino. The main research activity of iXem Labs is the development of products that reduce the technology gap in rural and peripheral areas, mostly concentrating on the introduction of innovative solutions using the Internet of Things to precision agriculture applications.

iXem Wine is one such project. It was born in 2013 as a platform that enables the visualization and sharing of meteorological data acquired from vineyards and transmitted wirelessly. That same year, the first sensor nodes were deployed for the acquisition of data in the Barbaresco vineyards in Piedmont. In 2016 the platform was applied to acquired data from experiments done in the Montalcino and Montepulciano zones in Tuscany. In 2017 the platform was tested with new sensor nodes that used the innovative LoRaWAN protocol, able to transmit data across distances larger than 50 km.

Since then, the platform and sensor nodes have received constant updates and support, and still ongoing currently, becoming a tool for the free sharing and visualization of meteorological data of agricultural applications acquired by sensors developed in house as well as developed by third parties. With over 250 sensor nodes installed in the Italian territory, the project has been a success and a source of pride for all past and present iXem Labs team members. This thesis is, essentially, the research and development of the new generation of sensor nodes to be deployed to vineyards across Italy.

1.2 An Introduction to LoRa®

LoRa®, short for "Long Range", is a set of physical layer parameters that enable long range transmissions with low power consumption. This technology, developed by Cycleo and then acquired by Semtech, is a modulation technique that enables long-range transmissions with low power consumption [3]. The main advantage of LoRa® wireless modulation is the ability to recover data that would normally fall below the noise floor. This allows for long-range transmissions, at the cost of bandwidth. However, LoRa has become the de facto wireless platform for IoT applications [4], which require low power, low cost, and low bandwidth solutions, with transmission range flexibility. As such, it fills the gap left by BLE (short range, low power, and wide range of bandwidths), and cellular (Long range, high power, and high bandwidth).

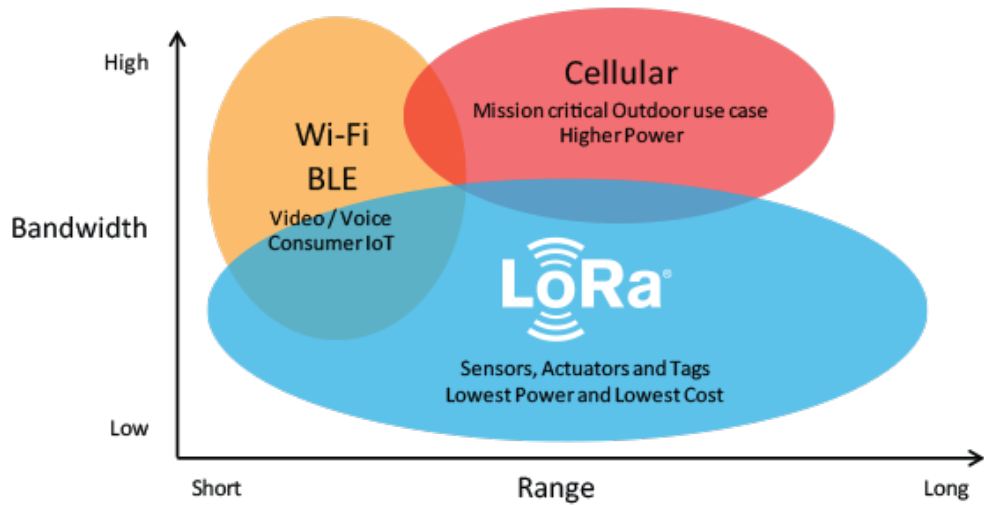


Figure 1.1: LoRa®: Technological gap filled

Taking the LoRa® modulation techniques, Semtech founded the LoRa Alliance, an open, non-profit organization dedicated to supporting the LoRaWAN® standard. LoRaWAN® is a Low Power Wide Area Network (LPWAN) which uses LoRa® as its physical layer, and expands on it to define a complete network standard for interoperability among LoRa® devices, as well as defining the parameters for each region in the world where LoRaWAN® is to be deployed.

As such, the usual setup of an IoT application using LoRaWAN® is to have end nodes or sensor devices with embedded transceivers capable of LoRa® modulation, which send their data to a receiver, or gateway. The gateway sends information via Wi-Fi, Ethernet or Cellular to a network server, which is responsible for network management functions. Then an application can be developed to interpret the data collected and use it for the target use case. LoRaWAN® is also bi-directional, which allows for Firmware Over-The-Air (FOTA) updates [5].

1.3 An Introduction to The Things Network

The Things Network (TTN) is a global, open workbench that facilitates building IoT ecosystems that use LoRaWAN®. It is powered by The Things Stack (TTS), an open source LoRaWAN® Network Server designed for various deployment scenarios, supporting all existing LoRaWAN versions [6]. Gateways are configured to interface

with The Things Stack through standard IP connections. These gateways give coverage and relay information to and from any LoRa® device in its reception area to the TTS network server [7]. As it is open source, any device that can transmit data to any gateway is connected to TTS, even if the gateway was installed by a third party. Due to this characteristic, TTS offers a wide coverage for the deployment of LoRa® devices.

TTS also offers a console as the main user interface, where a user can create applications. Devices connected to TTS through gateways can be added to user applications on The Things Network, which will allow users to visualize and control the traffic between the device and the network server. Applications on TTN also allow for further development by allowing cloud integrations with popular IoT platforms, as well as in-built Webhooks and MQTT servers, making it possible to analyze the data transmitted by end devices for visualization, machine-learning or even triggering events for automation purposes [8].

1.4 State of the Art of the iXem Wine Project

The current version of the iXem Wine project is a platform where winegrowers across Italy can monitor the weather conditions of their vineyard in real time. The acquisition of weather data is performed by portable meteorological stations that can be installed in any area covered by a LoRaWAN® gateway connected to The Things Stack network server. These stations are comprised by the meteorological sensors and a central unit, hereinafter referred to as sensor node. The sensors measure different types of data pertaining to the weather conditions of the vineyard, which are collected by the sensor node and transmitted through LoRa® to a gateway. This gateway will then upload the data to the The Things Stack network server, where a dashboard can be accessed to visualize the acquired data in real time by any user with an internet connection. The sensor node will be the focus of this thesis.

The sensor node is comprised of two parts: The sensor node board or sensor node PCB, and the mechanical fixtures of the PCB. The sensor node PCB is a LoRa® enabled device that has a Murata 1SJ module on board which manages the acquisition of data from the sensors, and then generates a signal to be transmitted with the LoRa® modulation technique. The transmission method of the current version of the sensor node is through the use of an external antenna. To connect to this antenna, the PCB includes a UFL type connector where a pigtail is connected. This pigtail then feeds the external antenna input, which transmits the data at 868 MHz

according to the EU868 LoRa® regional parameters. The current implementation of this connection interface with the external antenna can be seen in Figure 1.2.

The connection interface of the current sensor node with the meteorological sensors is done through Wago 250-20X terminal blocks (Grey connectors seen in Figure 1.2). These connectors have a button that can be pressed to open the contact and insert the cable termination. When the button is released, the connector clamps around the exposed conductor of the cable, securing it and making an electrical connection to the board.

The way the sensor node PCB is installed in the vineyards is by using a generic weatherproof junction box made of plastic. This box, however, does not provide any type of opening for the sensor cables to be passed through. Due to this, to assemble a current version sensor node, holes have to be drilled through the plastic enclosure to pass the sensor cables to connect to the PCB, as well as the hole needed for mounting the antenna. To increase the ingress protection of the sensor node, the sensor cables are passed through cable glands which clamp around the cables' insulator and decrease the risk of dust and water entering the enclosure and affecting the PCB. The cable glands and mounted antenna can be seen in Figure 1.2.



Figure 1.2: Current generation of sensor node PCB

1.4.1 List of Compatible sensors

The following table shows all the sensors that are being used with the current generation of sensor nodes. Although any sensor that uses I2C, ADC, GPIO or UART to send their data could be connected to the sensor node, the current

firmware supports exclusively the sensors in Table 1.1 for data processing.

Sensor Model	Measured value	Communication Method
Navis WSS 100	Wind Speed	Pulses (1 pulse per rotation)
?	Wind Direction	?
Pronamic Tower Rain Gauge 9602	Precipitation	Pulses (1 pulse per mm of rain)
DeltaOhm HD3901	Leaf Wetness	Analog (0.5 - 3 V)
iXem Labs Leaf	Leaf Wetness	I2C Serial
?	Air T/H	I2C Serial
?	Ground T/H	Analog(?????)

Table 1.1: List of iXem Wine compatible sensors

1.4.2 Shortcomings of the current design

Now, we will delve into the shortcomings of the current implementation of the sensor node, which were the inspiration for the conception of this thesis and its objectives. The first issue with the current design is the use of the external antenna, which is a twofold problem.

- **The Pigtail** The UFL connector is not the most mechanically secure connector. Due to this, during assembly off the sensor node, the pigtail is secured to the board with the use of liquid electrical tape. This fixes the pigtail to the board, but in the case the pigtail is damaged, the whole board has to be replaced. The pigtail also increases the mechanical part count of the device which is already elevated.
- **Mounting the Antenna** The second problem is the mounting method of the antenna. As described previously, a hole has to be drilled in the plastic enclosure to fix the antenna. The pigtail's SMA connector is secured to the enclosure with the use of nuts. However, this mounting mechanism does not guarantee that the enclosure keeps protecting the board from the environment. The band-aid "fix" to this was mounting the antenna on the bottom of the sensor node enclosure which reduced the risk of water entering the enclosure. This method does not guarantee the safety of the electronics of the sensor node as it voids any level of IP rating that the enclosure had prior to drilling the hole.

Shortcomings can also be found in the current connection interface with the sensors.

- **The Wire to Board Connectors** By using the Wago 250-20X connectors, as the way to connect the sensors to the board, even if they are easy to connect

and disconnect, the enclosure must be opened to be able to reach the PCB and the connectors. This makes service labors on installed sensor nodes difficult. If a technician is performing a sensor substitution, they must open the enclosure and have direct access to the PCB which puts the electronics in risk of being damaged.

- **The Cable Glands** To pass the sensor cables to the inside of the enclosure, more holes have to be drilled. As with the external antenna, this voids any weatherproof rating that the enclosure had. This compounds on the issue of keeping the board protected. However, the most glaring issue is how it makes the iXem wine stations non modular. The PCB has available connectors for all possible sensors, but if a client wants to have a sensor on a station that is already installed then the technician must have a drill and cable glands to install it. This complicates the installation of new sensors and harms modularity. What harms modularity the most is the fact that not have a cable inside it, it does not protect against the ingress of water and dust; a direct hole is left in the enclosure. As such the worst case scenario is needing to remove sensors from a station. Since the sensors cannot be disconnected without leaving the enclosure with holes, any station that needs to have a sensor removed needs to be completely replaced with a new sensor node that has less holes drilled through the enclosure.

The main effect of all these shortcomings is on the difficulty of assembly of the sensor nodes, which requires an excessive amount of time, the lack of modularity of the sensors, and the difficulty of maintenance of the stations.

1.5 Project Requirements and Research Objectives

The objective of this thesis is to design, test, and validate a prototype for the net generation of the iXem Wine sensor node. To achieve this, a set of design requirements for the project will be proposed. These objectives derive entirely from the state of the art of the project presented in section 1.4 and its current shortcomings. The project's requirements can be divided into two main categories: electrical and mechanical.

The mechanical requirements of the project pertain to the mounting mechanisms of the sensor node PCB and its connectivity with the meteorological sensors:

- **Ensure a weatherproof mounting mechanism of the PCB.** As discussed in section 1.4, the current mounting mechanism for the iXem Wine sensor

node PCB is a generic electrical box with holes drilled into it, and cable glands are used to pass the sensor cables to the board. By drilling holes into the box any IP rating it may have is voided and the risk of having water and dust enter the box and affecting the PCB increases. Due to this, a new enclosure must be proposed where the mechanism of passing cables through does not compromise the PCB to the weather.

- **Increase the easiness of assembly of the sensor node.** This addresses the high assembly time of the current generation of the sensor node. The proposed enclosure and mounting mechanisms must reduce assembly time and complexity of the sensor node. The aim is to reduce the use of specialized tools and improve the consistency of the assemblies.
- **Increase the modularity of the sensor node.** As discussed in section 1.4, currently there is no way of disconnecting individual sensors from the sensor node without accessing the PCB directly, and cable glands that are left empty no longer have any kind of weather protection. A new connection interface with the sensors must be proposed to increase the modularity of the sensor node while maintaining its weatherproof rating.

The electrical requirements of the project pertain to the design of the next generation sensor node PCB. As such, the new PCB must:

- **Conform to the chosen enclosure's dimensions.** The chosen enclosure will determine the dimension and mounting mechanisms of the PCB. Due to this, the design must take the mechanical characteristics of the enclosure to produce a PCB that fits inside the enclosure and is mounted securely during its operation.
- **Conform to the proposed connection interface.** The PCB must be designed to conform to the chosen connection interface with the sensors. The PCB should facilitate the modularity requirement as well as maintaining the simplicity of assembly, as discussed in the mechanical project requirements. As such it must maintain the compatibility to all the sensors that are compatible with the current version.
- **Integrate a 868 MHz planar antenna.** The main improvement of the PCB is to integrate a planar antenna within the printed circuit's footprint. This will avoid all complications from the use of the external antenna in the current design.
- **Include necessary hardware for firmware compatibility.** Compatibility with the current version of the firmware must be guaranteed, as well as being

compatible with the short to medium term firmware updates that have been proposed by the iXem Labs team.

To accomplish these requirements, a set of research objectives will be set:

- Research the working principle and possible topologies of planar antennas that work at 868 MHz. Using CAD and simulation programs, design the possible topologies based on electromagnetic principles and fabricate the antennas to be tested in an anechoic chamber for validation. Analyze the results and select an antenna that satisfies the project requirements.
- Research the weatherproof mechanisms and ratings of enclosures and propose a mounting mechanism aimed at eliminating the shortcomings of the current mechanism. Afterwards, validate its functionality with stress tests and use-case scenarios that prove it satisfies the project requirements.
- Using previous knowledge of PCB design principles and the chosen antenna, design a prototype for the new generation of the sensor node PCB that fulfills all electrical project requirements. Validate the functionality of the proposed design by testing in multiple scenarios, as well as validating the correct behavior of the integrated antenna.

1.6 Structure

The remainder of this thesis will be structured as follows:

- **Background:** Presents the theoretical foundations that were required for the development of the sensor node.
- **Research and development methodology:** Outlines the methodology to be used for the design, implementation, validation, and subsequent operation of the sensor node
- **Design of PCB antennas for LoRa EU868:** Presents the design process and simulation results of multiple planar antenna topologies.
- **Validation of designed PCB antennas:** Presents the testing methodologies and test results of the designed PCB antennas. The antennas will be compared, and one will be chosen to be integrated in the sensor node PCB according to their characteristics.
- **Mechanical design of the sensor node enclosure:** A mounting method for the PCB will be proposed as well as a connection interface to increase modularity and ensure a weatherproof vessel for the sensor node.

- **Design of the sensor node PCB:** Presents the design process of the sensor node PCB.
- **Validation of the sensor node:** Presents the testing methodologies and test results of the designed sensor node's mechanical characteristics and use-case behavior.
- **Conclusions and future work:** Concludes this thesis by verifying if all the goals were accomplished, and presents improvement opportunities for future versions of the iXem Wine sensor node.

Chapter 2

Background

This chapter presents the theoretical background needed to support this work. The knowledge needed is wide, as the goal of this thesis is a holistic hardware design of the prototype for the next generation of the iXem Wine sensor node that accomplishes all the objectives set in section 1.5.

This analysis starts with a deeper view into the LoRaWAN® protocol, regional parameters, and project requirements for our LoRa® device. The main focus will be on explaining the working principle of the LoRa® physical layer, as well as presenting the EU868 regional parameters and their influence over the project requirements, specifically, the influence over the design requirements of the integrated PCB antenna.

Having obtained the knowledge on the regulations for the design of a LoRaWAN® enabled device, the theory needed for the design of a EU868 compliant antenna will be presented. The aim is to analyze the working principle of antennas, how these translate when designing a PCB antenna, and the main types of PCB antenna topologies and their characteristics.

Lastly, the project-specific requirements with regards to the weatherproof ratings needed for an outdoors sensor node.

2.1 A deeper dive into the LoRaWAN[®] protocol and regional regulations

As we briefly touched upon in section 1.2, LoRaWAN[®] is an LPWAN that uses LoRa[®] as its physical layer, and expands on it to define a complete network standard for interoperability among LoRa[®] devices. The main characteristic of LoRa[®] is its ability to transmit data across long ranges. Here we will present the working principle of the LoRa[®] modulation technique and the regional parameters that are defined by the LoRa[®] Alliance for Europe.

2.1.1 The LoRa[®] Modulation Technique

Initially, when the LoRa[®] modulation technique was first released, Semtech did not give a mathematical definition based on signal theory. It was until 2017 when Lorenzo Vangelista, from the University of Padova, published his IEEE paper *Frequency Shift Chirp Modulation: The LoRa Modulation* [9] that the technique for modulation and demodulation in LoRa was described.

Traditional radio transmission techniques like AM and FM transmit the analogical information of a signal by modulating it with a carrier wave. In the case of AM, the carrier wave's signal is modulated, and in FM the frequency is modulated. As such, to recover the original wave, an AM demodulator must identify the changes in the transmitted signal's amplitude, while an FM demodulator should identify the frequency changes. Other types of analog modulation include PM and QAM.

For the modulation technique of digital signals the term keying is used, where a digital message is represented as an analog waveform. Here, a finite number of symbols can be represented according to the characteristics of the analog waveform. For example, Phase Shift Keying (PSK) encodes information into the phase of the carrier wave. BPSK (2-ary PSK) can represent 2 symbols according to phase changes.

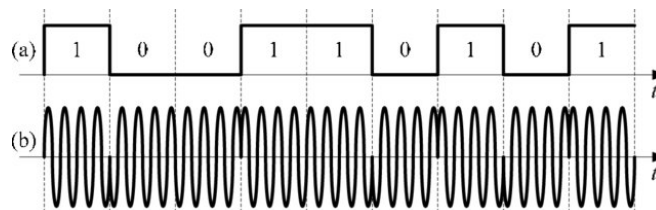


Figure 2.1: Example of BPSK modulation format, (a) binary signal, and (b) BPSK modulated signal [10]

As we can see in Figure 2.1, the phase of the carrier signal changes by 180° for the two symbols to be represented. This is expanded upon by M-ary PSK, where M symbols are represented with $360^\circ/M$ degrees of phase difference between each key. More symbols represent a higher number of information being transmitted with the same carrier wave. For example, Figure 2.2 shows the constellation diagram of an 8-PSK modulated digital signal, where 3 bits can be modulated at the same time with 8 symbols.

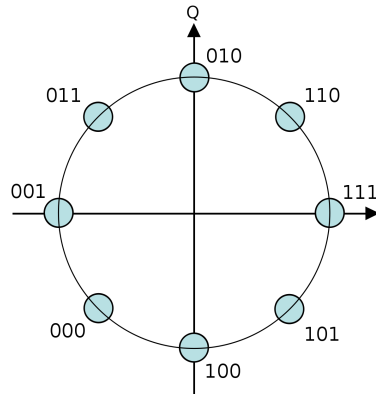


Figure 2.2: Constellation diagram of 8-PSK modulation [11]

As such, keying allows an analog carrier wave to transmit digital information.

In his paper, Vangelista describes LoRa[®] as a Frequency Shift Chirp Modulation (FSCM) [9], where symbols are keyed with a frequency chirp signal. A chirp is a sine wave whose frequency changes or decreases linearly in time. In LoRa[®], chirps are the carriers of data.

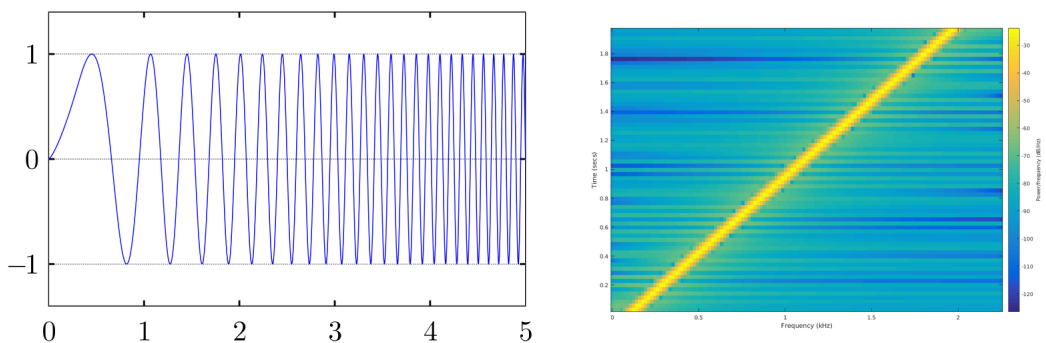


Figure 2.3: Chirp waveform represented in a) Time, b) Frequency spectrum [12]

A chirp can be defined as an upchirp when the frequency increases linearly as in Figure 2.3, and a downchirp when the frequency decreases linearly. LoRa® defines Spreading Factor (SF) as a representation of chirp rate where SF can take values of 7 to 12, being this number the amount of bits per symbol. As such, the Number of Symbols (S) that can be represented by the keying is defined by $S = 2^{SF}$. Due to this, the number of symbols that can be represented for SF7 would be 128, while SF12 has 4096 symbols. The time that takes to transmit one full symbol or Symbol Duration (T_s) is unique for each SF and the sampling period $T = 1/B$ according to $T_s = 2^{SF} * T$, so lower Spreading Factors have a higher bit rate. The way that different symbols are defined is by the starting frequency of the chirp.

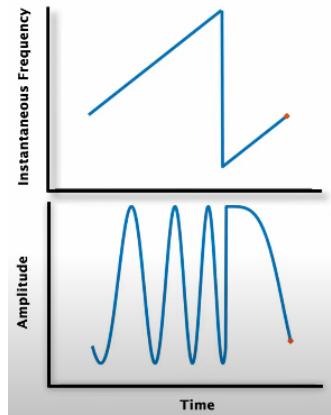


Figure 2.4: Frequency and time visualization of symbol 33 of SF7

We can see in Figure 2.4 that a symbol is characterized by the start and end frequency of the chirp, but most importantly, by the position of the discontinuity of the symbol. Therefore, the task of a LoRa® demodulator is to identify the position of the discontinuity within a symbol frame, translate it to a symbol number, and finally decode the information from the symbol number to bits.

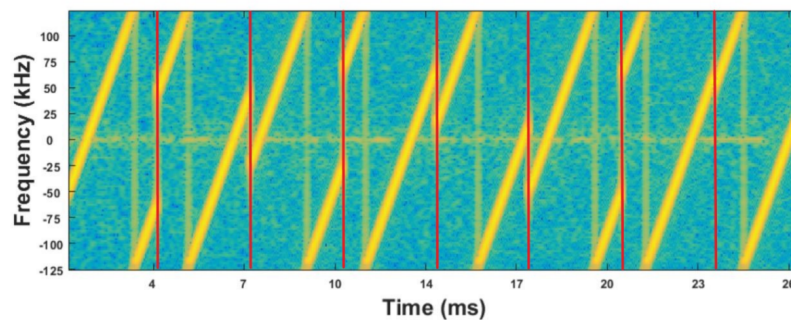


Figure 2.5: Spectrogram view of a LoRa transmission [13]

However, what makes LoRa® special in its ability to recover signals from below the noise floor is the interesting way the demodulator identifies the correct symbol. Analysing the symbol's frequency spectrum and finding the timing at which the discontinuity happens in LoRa works with the principle of correlation.

Instead of directly measuring the time of the discontinuity, the demodulator compares the frequency spectrum of the sampled symbol to a local copy of the frequency spectrum of all LoRa® symbols for the specific spreading factor. Then a value of how similar the received symbol to each of the symbols, called correlation strength, is found and the received symbol is interpreted as the symbol to which it had the most similarity. It follows that for each received symbol, the demodulator generates a vector of 2^{SF} of correlation strength values, and then selects the highest value as the interpreted symbol. For a more in depth mathematical explanation of how the demodulator does this exactly while maintaining computational efficiency, please refer to Lorenzo Vangelista's paper [9].

The correlation demodulator is the main reason for the incredible performance of LoRa® for signals with low and negative Signal to Noise Ratio (SNR). Even if the signal is below the noise floor, the symbol's samples can still be compared and a correlation strength calculated.

SpreadingFactor (RegModulationCfg)	Spreading Factor (Chips / symbol)	LoRa Demodulator SNR
6	64	-5 dB
7	128	-7.5 dB
8	256	-10 dB
9	512	-12.5 dB
10	1024	-15 dB
11	2048	-17.5 dB
12	4096	-20 dB

Figure 2.6: LoRa®: SNR for different Spreading Factors [14]

Figure 2.6 shows a table extracted from the SX1276-7-8-9 datasheet, a LoRa transceiver by Semtech, that describes the theoretical minimum SNR required at the demodulator at which symbols can still be demodulated. The table also shows that for higher SF values, the minimum SNR decreases due to the fact that a larger amount of samples per symbol generates better correlation association. The performance increases, arriving to -20 dB at SF12. This type of performance is remarkable and shows why LoRaWAN® has become the IoT powerhouse it is today.

Knowing how the demodulator identifies the correct symbols, the only thing left is to understand how the demodulator knows where a symbol starts and where it ends. The Spreading Factor at which both devices work is known a priori, so the demodulator knows the Symbol Time (T_s). The timing synchronization of the demodulator is done through the LoRa packet format.



Figure 2.7: LoRa® packet format [15]

The preamble is a set of repeated symbols sent one after the other. Let's assume that an SF8 system has a 4 symbol preamble that is symbol number 0. At any point during operation the demodulator can receive a preamble. Let's assume the demodulator's frame is offset by 33 samples with respect to the received preamble. With this offset, the sample at which the continuity happens is not sample 0 but sample 33. As such, when the preamble arrives, the demodulator will associate the four received symbols to symbol number 33. Since receiving the same symbol continuously is very improbable, the demodulator will identify four straight S33 as a preamble, and that it must shift its frame by 33 samples to correctly synchronize with the incoming packet. This is the way the demodulator syncs its frame acquisition to the received data stream.

After synchronization, the sync message is received, which indicates the start of the payload. In Figure 2.8, the spectrogram view of a packet with 4 preamble symbols is visualized.

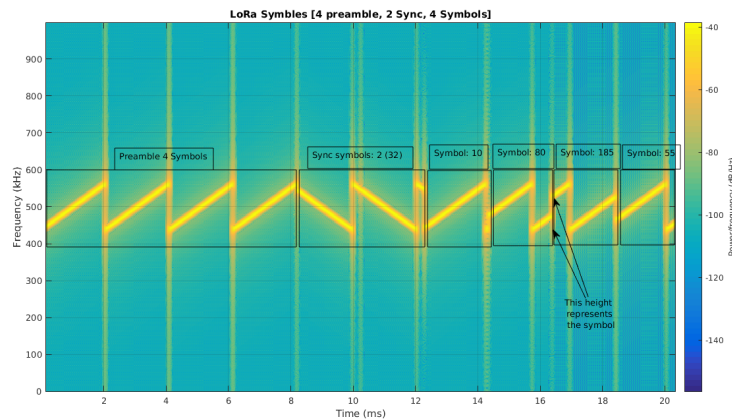


Figure 2.8: Spectrogram view of a LoRa® packet [15]

2.1.2 EU868

LoRaWAN® operates in the unlicensed radio spectrum, allowing for users to profit from the advantages of long range communication without paying large sums of money. Similar to Wi-Fi, anyone is allowed to setup devices and transmit signals without licenses or permits. However, as opposed to Wi-Fi, LoRaWAN® uses sub-gigahertz frequencies for its communication. This clashes with some regional limitations on the use of lower frequencies. This presents a difficulty for LoRaWAN® since it can't be a universal protocol. Due to this, the LoRa® Alliance specifies certain regional specifications called Regional Parameters, which delimit the overall characteristics for communications worldwide, divided in the regions:

- Europe
- The Americas
- China
- Australia
- Asia 1: Japan, Malaysia, and Singapore
- Asia 2: Brunei, Cambodia, Hong Kong, Indonesia, Laos, Taiwan, Thailand, and Vietnam
- South Korea
- India
- Russia

As this thesis is being developed in Italy for products to be deployed within the Italian territory, the applicable regional parameter is the EU863-870MHz frequency plan, mostly known as EU868, used in most countries in Europe and some countries outside Europe like Bahrain.

This regional parameter uses a frequency band from 863MHz to 870MHz, using 868MHz as the frequency where its default channels are located. The default channels are:

Channel Frequency (MHz)	Bandwidth (kHz)	LoRa data rate	Bit rate
868.10	125	DR0 - DR5	0.3 - 5 kbps
868.30	125	DR0 - DR5	0.3 - 5 kbps
868.50	125	DR0 - DR5	0.3 - 5 kbps

Figure 2.9: Default channels for the EU868 regional parameter [16]

These default channels must be implemented into any EU868 conforming device. EU868 also supports a maximum of 16 channels, for example, The Things Network uses five additional channels for uplink transmission:

- 867.1
- 867.3
- 867.5
- 867.7
- 867.9

The remaining 8 channels can be populated by the user through TTN and used by user devices.

The EU868 regional parameters also include other limitations on the transmission. Since it operates under the jurisdiction of the European Telecommunications Standards Institute (ETSI), the duty cycle of EU868 transmissions is limited to 1%. This limits the maximum allowed daily time on air of any one device to 1% of the day, or 864 seconds per day [16]. However, LoRaWAN® network operators can limit device maximum allowed daily time on air according to the Fair Access Policies. In the case of TTN, any one device is limited to 30 seconds per day for uplink messages, and only 10 downlink messages per day.

As we touched upon in subsection 2.1.1, LoRa® can work in a range of Spreading Factor configurations, which determines the data rates according to the selected transmission bandwidth. For EU868, the Data Rates are defined in TTN as follows:

Data Rate	Configuration (SF + BW)	Bit rate (bit/s)
0	LoRa: SF12 / 125 kHz	250
1	LoRa: SF11 / 125 kHz	440
2	LoRa: SF10 / 125 kHz	980
3	LoRa: SF9 / 125 kHz	1760
4	LoRa: SF8 / 125 kHz	3125
5	LoRa: SF7 / 125 kHz	5470
6	LoRa: SF7 / 250 kHz	11000

Figure 2.10: Bit Rates for different Data Rate categories in EU868 [16]

As we discussed in subsection 2.1.1, higher spreading factors cause lower bit rates, but improve performance for signals with negative SNR. LoRa® devices in EU868 must also implement one of the following Data Rates:

- DR0 to DR5: Minimal data rate set to obtain the LoRaWAN® certification
- DR0 to DR7
- DR0 to DR11: All data rates implemented

Another limitation set by the Eu868 regional parameters is the Effective Isotropic Radiated Power (EIRP), which is the total power radiated by an Isotropic antenna in a single direction. The EIRP values that a LoRa® device can use to transmit data are:

TX Power	EIRP	Calculated value
0	Max EIRP	+16 dBm
1	Max EIRP - 2 dB	+16 dBm - 2 dB = +14 dBm
2	Max EIRP - 4 dB	+16 dBm - 4 dB = +12 dBm
3	Max EIRP - 6 dB	+16 dBm - 6 dB = +10 dBm
4	Max EIRP - 8 dB	+16 dBm - 8 dB = +8 dBm
5	Max EIRP - 10 dB	+16 dBm - 10 dB = +6 dBm
6	Max EIRP - 12 dB	+16 dBm - 12 dB = +4 dBm
7	Max EIRP - 14 dB	+16 dBm - 14 dB = +2 dBm

Figure 2.11: EIRP values allowed by TTN in EU868 [16]

The max antenna gain for any device is also limited. In the case of EU868, it is limited to 2.15 dBi.

Lastly, the maximum payload size is also limited according to EU868 for each different data rate:

Data Rate	Configuration (SF+BW)	Maximum application payload size (bytes)
0	LoRa: SF12 / 125 kHz	51
1	LoRa: SF11 / 125 kHz	51
2	LoRa: SF10 / 125 kHz	51
3	LoRa: SF9 / 125 kHz	115
4	LoRa: SF8 / 125 kHz	242
5	LoRa: SF7 / 125 kHz	242
6	LoRa: SF7 / 250 kHz	242

Figure 2.12: Maximum payload size in EU868 for different data rates [16]

2.2 Working Principle of PCB Antennas

This section will provide a brief introduction to antennas and a summary of their history. Afterwards, the theory of the antenna working principle will be described, the main characteristics of an antenna, and how it translates to circuit printed resonant structures. Finally, the main PCB antenna topologies will be presented.

2.2.1 What is an Antenna?

An antenna is the interface between radio waves propagating through space and electric currents. An antenna transmits and receives electromagnetic waves to and from space. In transmission, a radio transmitter supplies an electric current to the terminals of the antenna through conducting elements, which is then radiated by the antenna as radio waves. In reception, the antenna intercepts radio waves traveling through the space it occupies and generates an electric current at its terminals. A receiver will then take these currents and apply signal processing techniques to recover the information transmitted by the radio waves [17].

There are two main types of antennas: aperture and resonant. Aperture antennas have guiding structures that guide radio waves from a feed antenna in a particular direction. Since LoRaWAN® devices are meant to be implemented in a star of stars topology, where one node can connect to multiple gateways that can be installed in any direction respective to the node, antennas that are used in LoRa® devices should be as isotropic as possible. Because of this, this thesis will only describe resonant antennas that have radiation patterns as close to an isotropic antenna as possible.

The first experiments that proved the existence of electromagnetic induction and created the first spark for the development of radio technology were carried out by Michael Faraday in the early 1830s. He discovered that moving a magnet through a coil of wires caused electric currents to pass through the wires. The coil acted as what we know today as a loop antenna and received the electromagnetic flux caused by the time-varying magnetic field of the moving magnet. This experiment eventually led to the development of the cornerstone of electromagnetism: The Maxwell equations [18].

James C. Maxwell was inspired by Faraday's experiment and description of *Lines of Force*, as well as Lenz's work on defining the direction of the induction and Neumann's equation to calculate the induced force according to the change in magnetic flux. This led to him working on a comprehensive summary of the electrodynamic principles, which he published in papers from the 1850s to the 1870s.

The culmination of his work was the 1873 publication *A Treatise on Electricity and Magnetism* in which he unified the theories of light and electromagnetism. Further work by Oliver Heaviside synthesized the original 20 Maxwell equations into the 4 Maxwell-Heaviside equations that are in use by physicists today [19].

The experimental proof of the Maxwell equations was developed in 1886 by Heinrich Hertz. He manufactured what would later be called a dipole antenna, and forced an electrical spark to occur in its gap. Of course, by our understanding today, we know that this spark was generating a current in the dipole's terminals and created a resonance through its arms, generating an electromagnetic wave. Hertz identified this electromagnetic wave with the use of a coil (loop antenna) as a receiver, generating a spark at its terminal whenever the dipole transmitted [20]. With this setup he proved that Maxwell's equations were true with regard to electromagnetic waves travelling at the speed of light. He also proved that electromagnetic waves also succumb to the phenomena of reflection, refraction, polarization, and interference. However, when his students asked about what was next after proving the existence of the then called *Hertzian waves*, Hertz famously answered [21]

Nothing, I guess

Some years later, a young man vacationing in the Alps read Hertz's publication on the *Hertzian Waves* and was inspired. This report gave him an idea to use Hertz's waves as a signaling method. This young man was Guglielmo Marconi [21]. In 1895 he would start developing structures that would be practical for long-distance, wireless telegraphy. He gave these structures the name of *Antenna*, marking the birth of long distance radio transmissions.

The first breakthrough in antenna transmission distance came in 1895, where Marconi discovered that grounding the antennas and raising the height of the structure increased the transmission range of the antennas from 0.8 km to 3.2 km. By grounding his antennas, Marconi created a monopole antenna, that would radiate at higher frequencies and have a larger range. After travelling to Britain and patenting his work, Marconi demonstrated that Morse code could be transmitted over a distance of 6 km by sending the first ever wireless communication over open sea across the Bristol Channel. Having gained the interest of the British government and other nations worldwide, Marconi was able to improve his transmission systems until, in 1901, Marconi was able to send signals over the Atlantic, from Cornwall, England to Signal Hill, Canada at 850 kHz for a total distance of about 3,500 km [22]. Since then, Antenna development and theory has continued to advance, being an essential component of modern technologies.

2.2.2 Main Antenna Topologies

The main physical mechanism by which a resonant antenna produces a radio wave is the radiation mechanism. Taking an open ended wire as an example, when it is initially energized, the charges in the wire are set in motion. The acceleration of the charges by the source's electric field, as well as the deceleration produced by the reflection at its open end, produce electromagnetic radiation from the wire. The acceleration and deceleration of the charges describe an oscillating movement, which, according to the wire's geometry, has a specific oscillating frequency.

When applying the same idea to two wires, by connecting a voltage source to their end points as in Figure 2.13, a traveling wave current of magnitude $I_o/2$ is created along both wires. When the wave current arrives at the end of each of the wires, it undergoes a complete reflection, resulting in a reflection with 180° phase difference. When combined with the original wave, a sinusoidal wave pattern is generated and radiated. However, since the second wire has the inverted signal of the first wire, the radiated fields are cancelled since they both generate fields with the same magnitude but of opposite phase. This structure is an ideal transmission line, where the wave is guided along the line with no radiation losses.

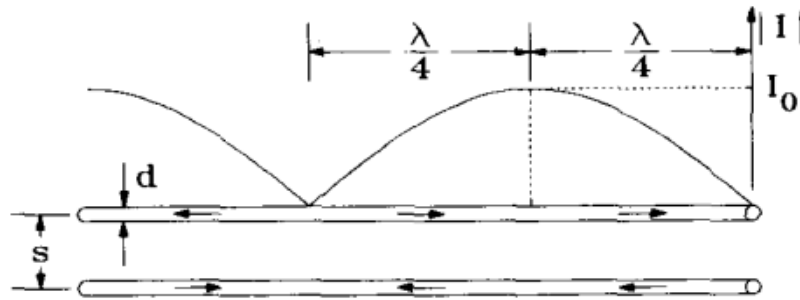


Figure 2.13: Two Wire Transmission Line [20]

To achieve a radiating structure with two wires, they must be flared out as in Figure 2.14. By flaring out the structures at a length of $\lambda/4$ (being λ the wavelength for a given frequency) from the end point of the wire the structure starts to radiate. Since the current distribution in each wire is unaltered, the field is radiated equally to the parallel wire example in Figure 2.13. However, since the flared section of the transmission line is not parallel to each other, the fields will not cancel each other out completely any more, leaving the non-cancelled part as a radiated field.

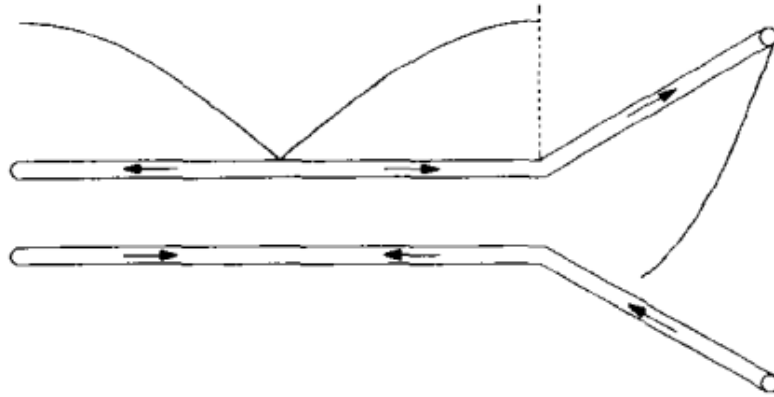


Figure 2.14: Flared transmission line [20]

This phenomenon can be further exploited by arriving to a structure like the one shown in Figure 2.15, which is more commonly known as a Half-Wave (or $\lambda/2$) Dipole. By making the flared sections, now called the *arms* of the dipole, parallel with each other, will radiate fields that have the same phase and are oriented spatially in the same direction. As such, the fields of both arms will reinforce each other, creating a radiation pattern [20].

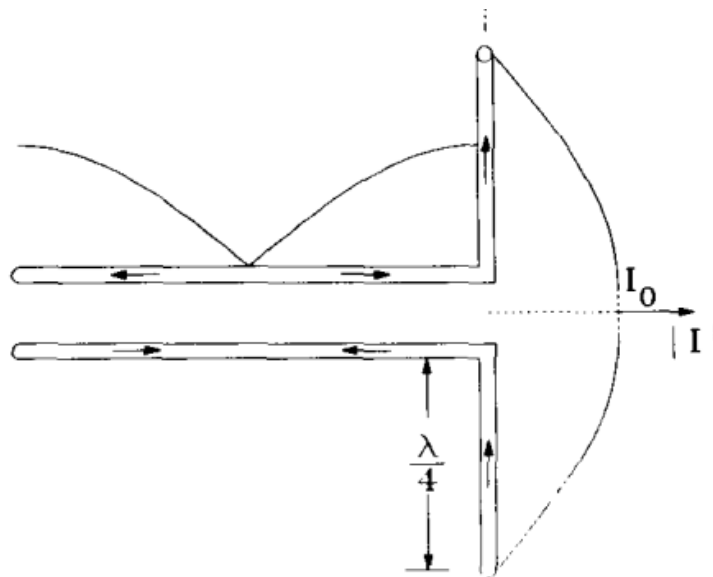


Figure 2.15: Two wire dipole [20]

By revolving the radiation pattern of the $\lambda/2$ dipole shown in Figure 2.15 in 3 dimensions we can obtain the amplitude radiation pattern of the antenna:

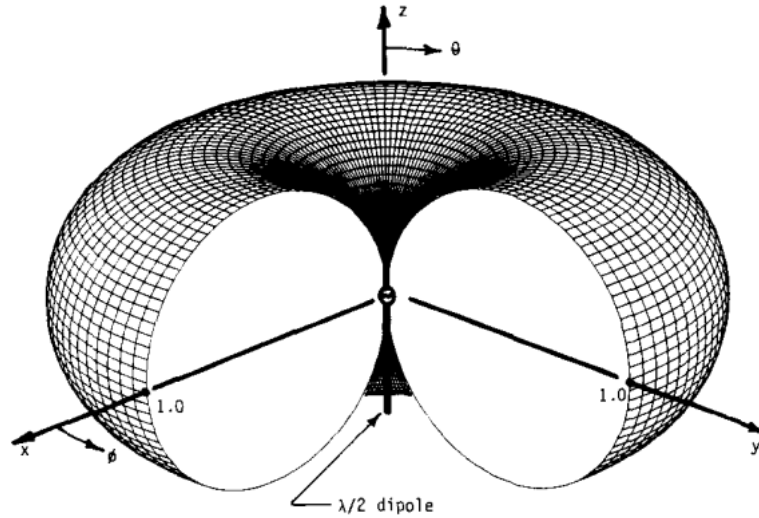


Figure 2.16: 3D radiation pattern of a $\lambda/2$ dipole [20]

The 3-Dimensional pattern shown in Figure 2.16 is called a Toroidal pattern. This type of pattern is the closest to an isotropic antenna (one that radiates equally in all directions) that can be achieved with real antennas. However, for our specific use case, LoRaWAN® Gateways are very improbable to be installed directly above or directly below sensor nodes since these are installed in vineyards in open field. The toroidal radiation pattern is also good enough for the common case in which gateways are installed at the top of hills or mountains, while sensor nodes are installed in valleys. Due to this, this thesis will concentrate only on antennas with toroidal radiation patterns, also called Omnidirectional Antennas.

Another factor that is pertinent when designing real antennas is the so called *End Effect*. This effect happens in real conductors and results from the fact that the signal travels through a finite conductor. Specifically, at the ends of a real finite wire there is a decrease in inductance and an increase in capacitance. This, effectively, lengthens the antenna, and results in a decrease of resonant frequency. An adjustment factor must be applied to the length of a real dipole due to the end effect of about 0.952. Due to this the length of a real dipole wire antenna should be calculated with:

$$L = \frac{c}{2f} \times 0.952 \quad (2.1)$$

The other main wire antenna topology that has an omnidirectional radiation pattern is the Quarter Wave Monopole. This is an arrangement derived from the $\lambda/2$ dipole antenna. One $\lambda/4$ arm of the dipole is kept, and the other arm is grounded, usually turning into a ground plane. The $\lambda/4$ arm is mounted perpendicular over the

ground plane and the antenna is fed the same way as the dipole, but since one side is grounded, the source is no longer differential but single ended. This antenna exploits the phenomenon of reflection of the electromagnetic waves on the ground plane to replicate the monopole's current distribution, which will generate a field in exactly the same way as a complete half-wave dipole as shown in Figure 2.17. Therefore, we can obtain an antenna of half the physical length as a dipole that radiates in exactly the same way, as long as the ground plane can be accommodated.

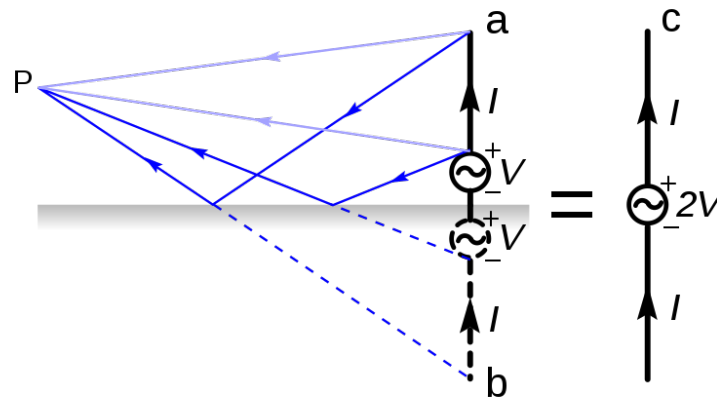


Figure 2.17: Quarter-wave monopole antenna and equivalent dipole [23]

Another advantage of the monopole antenna is that it is easier to feed than the dipole antenna. The majority of modern embedded applications have radio sources that are single ended, or unbalanced sources. Since dipole antennas are balanced, a balun, or balancing unit, is required to feed the antenna properly by turning the unbalanced input to a balanced one. Since the monopole antenna is single ended, there is no need for a balun, simplifying the antenna feeding. The main disadvantage when comparing to a dipole antenna is that monopole antennas have a lower radiation efficiency due to imperfect ground planes. In static applications where the antenna does not move the earth is used as ground plane, while in most mobile applications a virtual ground plane is used by using the body of the device as ground. This body must be electrically conductive to be able to work as a ground plane.

Other omnidirectional wire topologies are mostly evolutions of the monopole antenna such as:

- **Whip and Short Whip:** The name whip derives from their main characteristic: their flexibility. They are usually made of interlocking telescopic metal tubes, or flexible fiberglass rods around conductive cores, and have a $\lambda/4$

length. Short whips have the same characteristic but have an inductive coil in series with the radiation structure to be able to shorten the antenna's length.

- **Rubber Ducky:** Takes the short whip concept further by coiling the entire antenna structure. This distributes the inductance of the coil along the length of the antenna and shortens it even more.
- **Inverted L:** A monopole antenna that is bent at some point along its length to be parallel with the ground plane. This makes it more compact while the radiation pattern is kept the same, but at the cost of having very low impedance, which makes impedance matching more difficult.
- **Inverted F:** An inverted L antenna with intermediate feeding. The short circuit stub behaves as an impedance matching circuit, where its length changes the input impedance of the whole antenna. Can be tuned to any input impedance without changing the antenna's resonant frequency or radiation pattern.

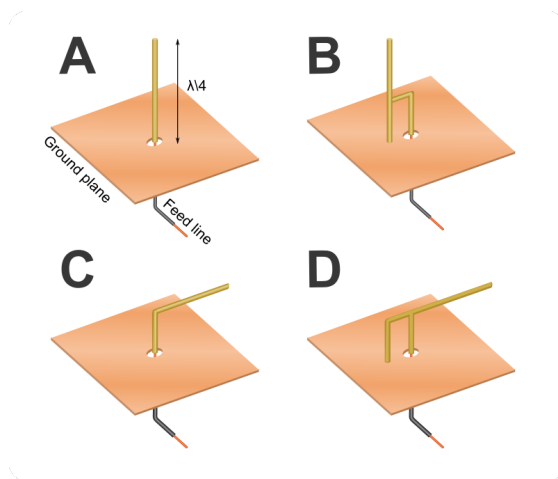


Figure 2.18: Omnidirectional wire antenna topologies. a) quarter-wave monopole, b) intermediate-fed quarter-wave monopole, c) inverted-L antenna, d) inverted-F antenna [24]

Other types of omnidirectional antennas that are not monopoles are:

- **Loop:** Balanced antenna consisting of a loop of wire whose perimeter dictates its resonant frequency. Very efficient, but can occupy a very large space.
- **Halo:** A half wave dipole where the arms are bent circularly. This achieves a loop-like structure but with a gap in the circle's perimeter.

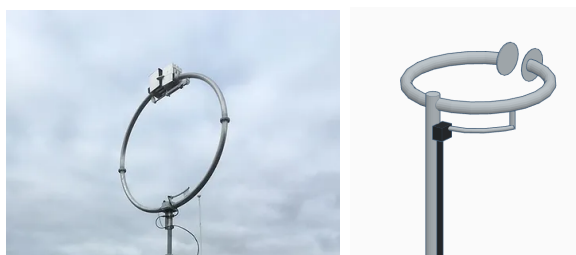


Figure 2.19: Antennas: a) Loop, b) Hoop

2.2.3 Making Antennas Planar

As technology becomes a part of our every day lives, portability is one of the most researched aspects nowadays. Such an effort has also been applied to antenna investigation to develop smaller antennas that can fit any type of device. A part of these developments, a substantial effort has gone into planarizing antennas so that they can be printed as part of a Printed Circuit Board (PCB), reducing costs and footprint of the device. Recent developments have even produced Flexible Substrate Antennas (FSAs) that are in great demand for next generation wireless devices.

Knowing this, the question arises on how the antenna's working principles presented in subsection 2.2.2 can be translated to a planar structure. The easiest structure to understand in a planar way is the half-wave dipole.

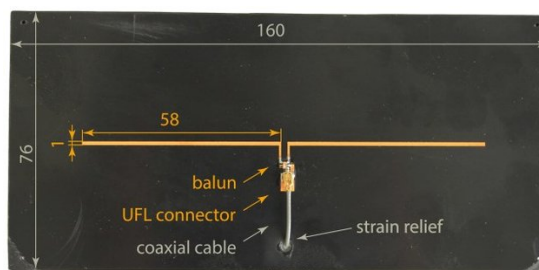


Figure 2.20: Planar Dipole Antenna [25]

As we can see in Figure 2.20, a planar dipole's structure is identical to a wire dipole since it is not ground plane dependent. As such, the same radiation mechanisms of the wire dipole apply to the planar dipole and the radiation pattern and efficiency will be the same. However, the fact that the copper traces are printed on top of a dielectric substrate means that some of the antenna's radiation characteristics change. The presence of the substrate changes the wavelength of the radiated wave. In the case of most printed circuits, the selected substrate is FR-4, a dielectric

composed by fiberglass bound with resin. Radio waves that are transmitted through FR-4 see a reduction in their wavelength of around 10 to 20 %, depending on the board thickness. This changes the transmission frequency of the antenna to a range of 110 to 120 % the nominal frequency of the wire dipole equivalent. To be able to design a PCB dipole antenna at a desired frequency, the arms must be designed around 10 to 20 % shorter than the nominal $\lambda/4$ of the wire dipole.

This same phenomenon applies for the planar version of the monopole antenna, at times called the printed circuit whip or stub antenna. In this adaptation of the wire monopole antenna, the radiating structure is not normal to the ground plane any more, but it is all kept in one plane.

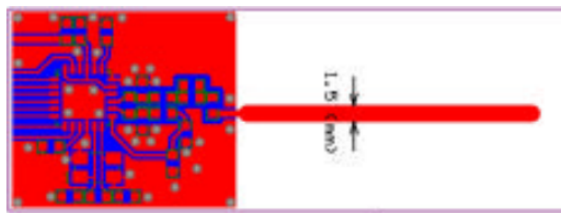


Figure 2.21: Planar Monopole Antenna [26]

As shown in Figure 2.21 the radiating arm and the ground plane are in the same plane and printed on top of FR-4 substrate. The length of the arm has to be 20 to 30 % smaller to accommodate for the frequency shift due to the substrate's effect on the radiated wave. The important distinction to be made is that even if the ground plane is not perpendicular to the antenna, the virtual ground phenomenon and reflection of the current distribution still happens in this configuration. Even if it will not be as efficient as a wire monopole antenna, a planar monopole antenna will still radiate omnidirectionally and at the frequency given by its length.

Due to the monopole being possible in a planar configuration, most of the same evolutions as discussed in subsection 2.2.2 can be carried out for planar monopoles:

- **Planar Inverted L:** Due to the current distribution being strongest near the feed point of the planar monopole antenna, the monopole's structure can be bent at a point in its length to become an inverted L antenna. Here, the section parallel to the ground plane will not radiate as it behaves as a transmission line, but the overall length of the antenna will remain unchanged. As such the resonant frequency of the structure will be the same.
- **Planar Short Whip:** By including a discrete inductor between the antenna and the feed point of the inverted L antenna, the length of the antenna can be decreases as in the wire short whip.

- **Inverted F:** An inverted L antenna with intermediate feeding. The short circuit stub to the ground plane behaves as an impedance matching circuit, where its length changes the input impedance of the whole antenna.

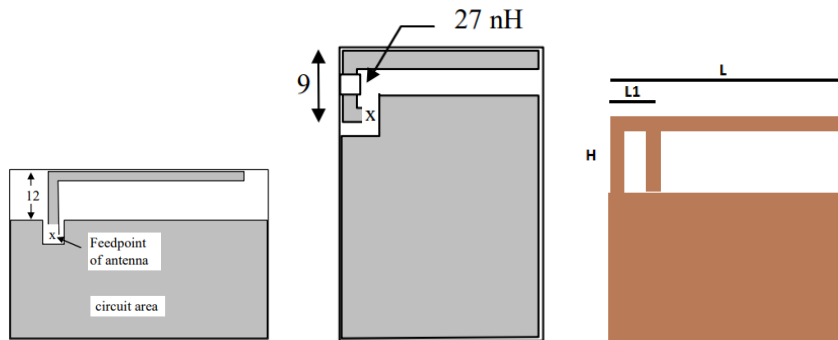


Figure 2.22: Planar Antennas: a) Inverted-L, b) Printed Short Whip, c) Inverted-F

Other printed antennas include:

- Loop
- Semiloop
- Patch

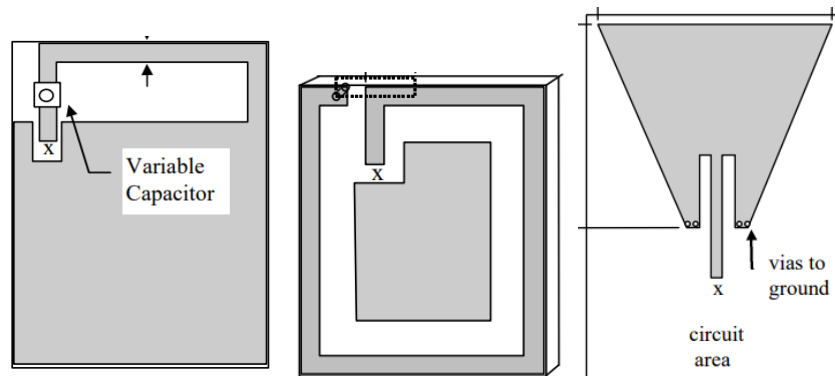


Figure 2.23: Planar Antennas: a) Loop, b) Semiloop, c) Trapezoidal patch

2.3 Product-Specific Hardware Requirements

The main objective of the iXem Wine project is the production of LoRa® sensor nodes to be installed in vineyards in Italy. Because of this, there are some additional considerations that must be taken into account for this thesis.

First of all, since the sensor nodes are installed in open fields and subject to rain, wind dust, and UV rays, weatherproof enclosures and cable management techniques must be implemented to protect the sensor node PCB. The protection capacities of an enclosure are specified according to its IP rating. The IP code is a two digit code that indicates how well a device is protected against water and dust. The IP ratings define protection as follows:

IP..	First digit: Ingress of solid objects	Second digit: Ingress of liquids
0	No protection	No protection
1	Protected against solid objects over 50mm e.g. hands, large tools.	Protected against vertically falling drops of water or condensation.
2	Protected against solid objects over 12.5mm e.g. hands, large tools.	Protected against falling drops of water, if the case is disposed up to 15 from vertical.
3	Protected against solid objects over 2.5mm e.g. wire, small tools.	Protected against sprays of water from any direction, even if the case is disposed up to 60 from vertical.
4	Protected against solid objects over 1.0mm e.g. wires.	Protected against splash water from any direction.
5	Limited protection against dust ingress. (no harmful deposit)	Protected against low pressure water jets from any direction. Limited ingress permitted.
6	Totally protected against dust ingress.	Protected against high pressure water jets from any direction. Limited ingress permitted.
7	N/A	Protected against short periods of immersion in water.
8	N/A	Protected against long, durable periods of immersion in water.
9k	N/A	Protected against close-range high pressure, high temperature spray downs.

Figure 2.24: IP Rating Table [27]

For example, an IP26 rated enclosure would be protected against solid objects over 12.5 mm and high pressure water jets. Taking this into consideration, for a vineyard which is exposed to dust and rain, an IP66 rating is the minimum required. Since the device won't be submerged at any point during normal operation, any ratings IP67 or higher would not be necessary.

Chapter 3

Research and Development Methodology

As a student with a bachelors degree from the Pontificia Universidad Javeriana in Bogota, Colombia, the author of this thesis has had a CDIO-based education throughout his whole career. CDIO stands for Conceive, Design, Implement, and Operate, and is an education standard with member schools throughout the world, being the Javeriana one of them since 2010. This initiative seeks to teach engineering students to identify possible solutions for a real life problem (**Conceive**), **Design** a system that could solve this problem based on theoretical fundamentals, **Implement** the solution with a prototype-test cycle, and finally be able to **Operate** their system in real use-case scenarios. Due to this, the research and development methodology of this thesis will be carried out under this paradigm.

The conception of the thesis happened due to the reasons discussed in subsection 1.4.2. There was a need to update the current version of the iXem Wine sensor node and this became the objective of the thesis. The output of the conception phase of a project is a set of requirements and objectives to be able to solve the proposed problem. As already laid out in section 1.5, our objective with this thesis is to redesign the electrical and mechanical aspects of the iXem Wine sensor node to improve on its shortcomings and provide future proofing mechanisms for future firmware updates.

The design phase then splits into three phases:

- **Design of the PCB antenna:** Using the electromagnetic simulator CST studio, a set of PCB antennas that transmit at 868 MHz for the LoRa® EU868 standards will be designed and simulated. Six different topologies of planar PCB antennas will be designed. The output of this design phase will be the

CAD files for the designed topologies as well as their simulation results.

- **Design of the PCB mounting and installation method:** Before the design of the PCB, the mounting mechanism and connection interface were decided upon. To fulfill the objectives in section 1.5, an enclosure and connector interface will be proposed to increase modularity of the station while ensuring a minimal IP rating of IP66. The output of this stage is a Bill of Materials (BOM) for the selected enclosure and connectors, as well as a description of the output interface.
- **Redesign of the sensor node PCB:** Using Altium Designer as a schematic and PCB CAD program, the PCB for the sensor node with the integrated 868 MHz antenna will be designed. Using the generated schematics and PCB design, this design phase will produce fabrication outputs, and Bill of Materials (BOM) of the sensor node PCB for its fabrication and assembly.

These design outputs will then be implemented in the following manner:

- **Implementation of the PCB antenna:** Using the CAD data of the designed PCB antennas, using Altium designer, a selection of the proposed geometries will be designed into mock PCBs. These will be fabricated and tested in the Politecnico di Torino's anechoic chamber to verify their performance. Once validated, an analysis on which antenna is the best for our specific use case will be selected.
- **Implementation of the sensor node PCB:** Using the fabrication outputs and BOM of the PCB, the PCB will be sent to fabrication at manufacturing house Eurocircuits. The result of this phase will be the fabricated and assembled PCB. This PCB will be tested in the anechoic chamber to verify the correct implementation of the PCB antenna. The PCB will then be loaded with the current version of the firmware and tested in the lab for core functionality.
- **Implementation of the sensor node enclosure:** With the BOM of the mechanical parts of the sensor node from the design phase, the parts will be acquired and the connectors and PCB will be installed. An initial test for weatherproof capabilities will be carried out to verify the effectiveness of the enclosure at keeping the PCB safe from the weather. Then the whole sensor node will be installed in a real use case scenario and tested with the sensors to verify its functionality as a LoRaWAN® sensor node.

After the implementation of the sensor node, the operating phase of the device will be carried out by checking regularly on its performance and comparing it to the current version of the sensor node. The verification of the prototype's functionality

will be the final step inside the scope of this thesis. However, the operating phase will continue afterwards when, according to the results obtained by this work, the decision to rollout the new generation sensor node in future installations of the iXem Wine station will be taken. If this is the case then the operating phase of the device will continue during its life cycle.

Chapter 4

Design of PCB Antennas for LoRa EU868

This chapter presents the design process of six different planar antenna topologies using the CAD and simulation tool CST Studio using the theoretical background on planar antennas presented in subsection 2.2.2 as a basis. The design methodology will be divided in three phases:

1. **Validation of the simulation tool.** To validate that CST Studio is simulating basic structures correctly, a simple 868 MHz wire half-wave dipole is designed and simulated. The simulation results will then be compared to the resonant frequency and radiation pattern of a theoretical wire dipole antenna.
2. **Design of the geometry of planar antennas.** After validating that CST Studio is an appropriate simulation tool, the planar antennas will be designed. The geometries of six different planar antenna topologies will be designed inside CST Studio.
3. **Simulation and optimization of the planar antennas.** After finishing the design of each planar antenna, the geometry will be simulated by feeding it through a $50\ \Omega$ port. The results of this initial simulation will show the reflection coefficient of the input port or S_{11} which shows the accepted power by the antenna and the resonant frequency, the input impedance of the antenna to see if the antenna is impedance-matched to the $50\ \Omega$ port, and the radiation pattern to prove the antenna is omnidirectional. Based on these initial results, the antenna's geometry will then be optimized and tuned to have the best performance possible. The final geometry of the antenna will be presented with its simulation results.

Having established this design structure, steps two and three will be repeated for each of the six following topologies:

- Planar dipole antenna
- Planar monopole antenna
- Offset planar monopole antenna
- Planar inverted-L antenna
- Planar meandered inverted-L antenna
- Planar inverted-F antenna

4.1 Validation of CST Studio as an antenna CAD and simulation tool

For the CAD and simulation tool CST Studio Suite 2022 will be used with the Academic Research license, which allows the export of .DXF files to then be imported into a PCB CAD tool. From Dassault Systemes’s website [28], CST Studio is a high-performance 3D electromagnetic analysis software package for designing, analyzing, and optimizing electromagnetic components and systems. This initial description promises all the desired characteristics needed for this research, nonetheless, a validation of its simulation capabilities and the conformity of its solving mechanisms to antenna theory was carried out before choosing it as the main simulation tool.

The validation methodology for the software was to design the geometry for a simple half-wave dipole wire antenna, simulate its electromagnetic properties, and compare the results to a theoretical dipole. To do this the dimensions of the antenna must be calculated. By the formula of dipole length in Equation 2.1.

$$L = \frac{299,792,458 \text{ m s}^{-1}}{868 \text{ MHz}} \times 0.952 = 0.164,4 \text{ m} \quad (4.1)$$

This value corresponds to the overall length (L) of the dipole, while the length of a single arm (l) will be $l = L/2 - g/2$, where g is the gap between conductors.

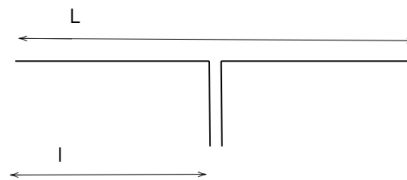


Figure 4.1: Dimensions of a Half wavelength dipole

As seen in Figure 4.2 the dipole antenna was designed in CST using two cylinders as the wires of the half-wave dipole. The total length (L) was set as 164.4 mm with a gap of 4 mm. Due to this the arm length (l) is 80.2 mm. The radius of the wires is set to 0.1 mm as a thin wire antenna to avoid frequency changes from the thickness of the conductor.

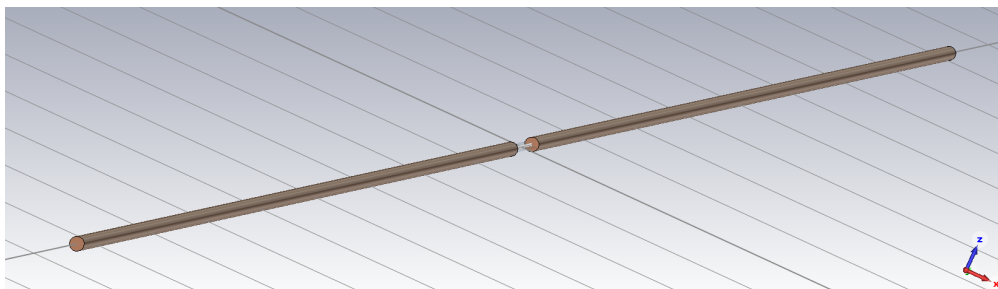


Figure 4.2: Half wavelength dipole in CST Studio

To simulate in CST studio a feed port must be declared. In this case, due to the balanced nature of the dipole antenna, a discrete port was declared between the two wires of the antenna so as to feed the antenna differentially. Due to the nominal impedance of a wire dipole being $73\ \Omega$, the port was declared with this impedance to have maximum impedance matching at the resonant frequency. The declared port (Port 1) is shown in Figure 4.3.

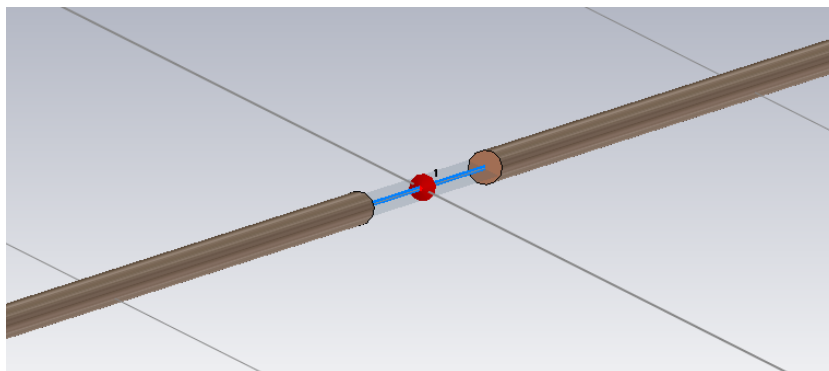


Figure 4.3: Port for half wavelength dipole

The simulation for this and all the antennas designed in this chapter will have the same simulation setup:

- **Frequency Range:** 200 to 2,000 MHz
- **Environment:** Open space on all directions

- **Mesh:** Hexahedral
- **Accuracy:** -40 dB
- **Frequency for radiation pattern monitor:** 868 MHz

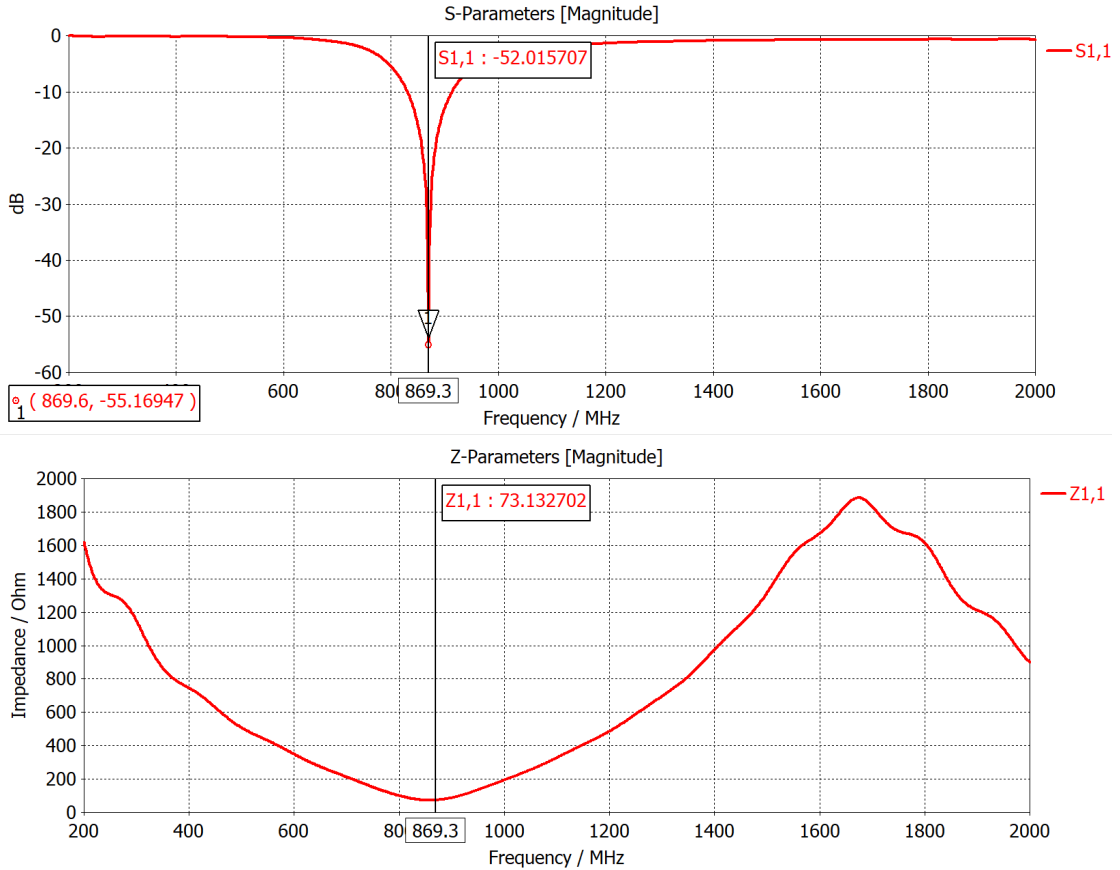


Figure 4.4: Simulation results a) S_{11} b) Input impedance

Figure 4.4 shows that the antenna resonates correctly at 869.6 MHz which is a 0.18 % error from the theoretical frequency of 868 MHz. Also the input impedance is shown to be 73.13Ω which is a 0.18 % error from the theoretical frequency of 73Ω .

Figure 4.5 shows the radiation pattern of the simulated wire dipole. We can see that the shape matches the radiation pattern of an omnidirectional antenna and proves the accuracy of the simulation of wire antennas along with the small errors to theoretical resonant frequency and input impedance.

After proving the functionality of the simulation tool for wire antennas, we needed

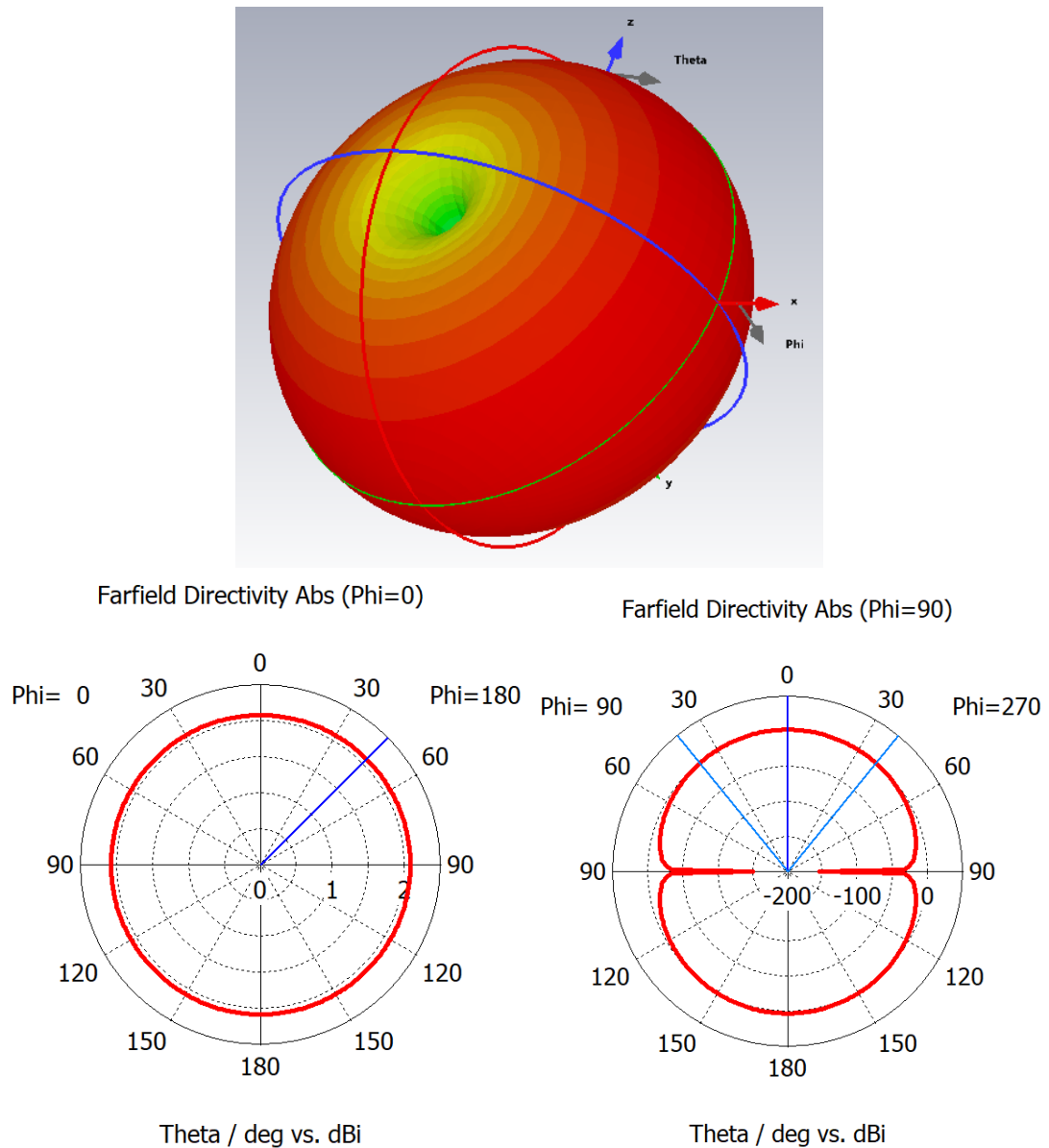


Figure 4.5: Simulated radiation pattern of wire dipole antenna. a) 3D radiation pattern. b) 2D cut of radiation pattern - XZ plane c) 2D cut of radiation pattern - YZ plane

to prove the functionality for planar antennas and if the effect of the dielectric is correctly simulated. As presented in subsection 2.2.2 we must first determine the scaling value necessary for the antenna geometry due to the effect of the dielectric. To determine this in the simulation software, an initial simple planar dipole antenna

was designed with the same dimensions as the wire dipole antenna.

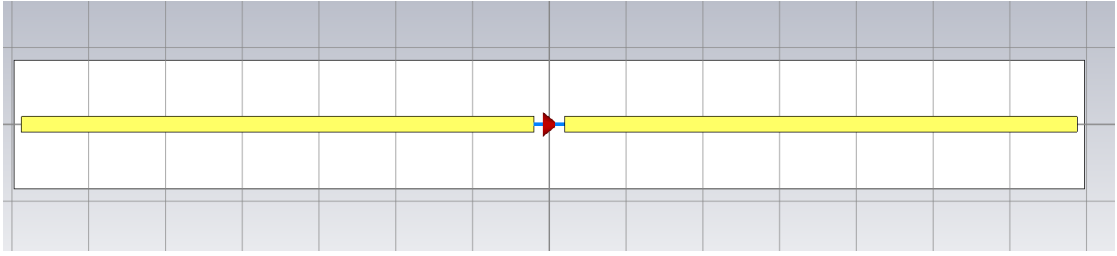


Figure 4.6: Simple planar dipole antenna

Figure 4.6 shows an antenna designed with overall length $L = 164.4$ mm and gap $G = 4$ mm, which corresponded to the wire antenna previously simulated. On simulation, the resonant frequency of this antenna was 738.2 MHz as shown in Figure 4.7.

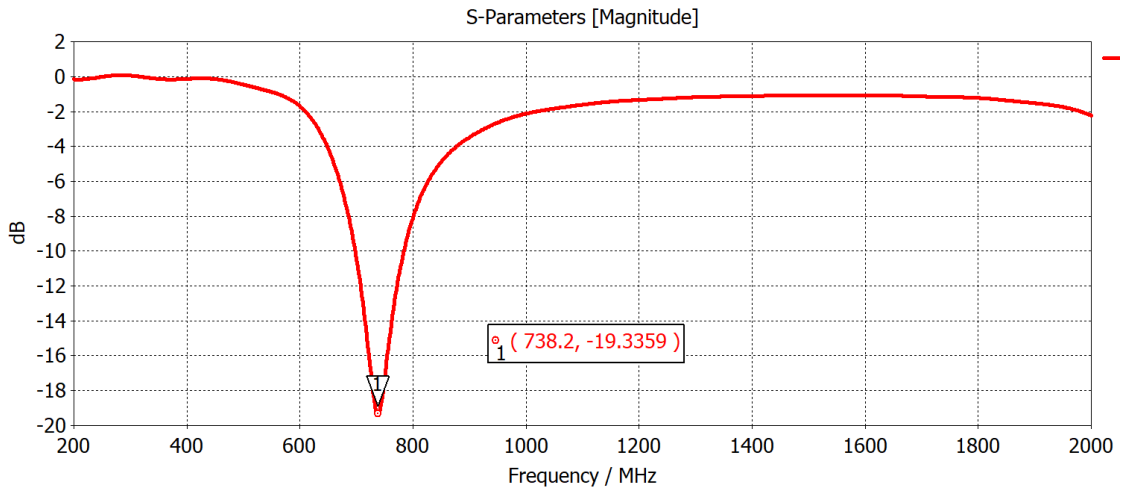


Figure 4.7: S_{11} of simple planar dipole antenna

With a resonant frequency of 738.2 MHz, the resonant frequency is 84.89% smaller than the nominal resonant frequency of 868 MHz. This means that the effect of the dielectric, in this case simulated as FR-4 with a thickness of 1.43 mm, is to virtually lengthen the antenna's geometry by about 15%. When applying a correction factor of 0.848896 to the dipole length, as well as to the dielectric's dimensions so as to keep the aspect ratio of the antenna constant, a resonant frequency of 867.8 MHz was achieved as shown in Figure 4.8. This proves that the dielectric is being simulated correctly and leads to the conclusion that CST studio is an appropriate simulation tool.

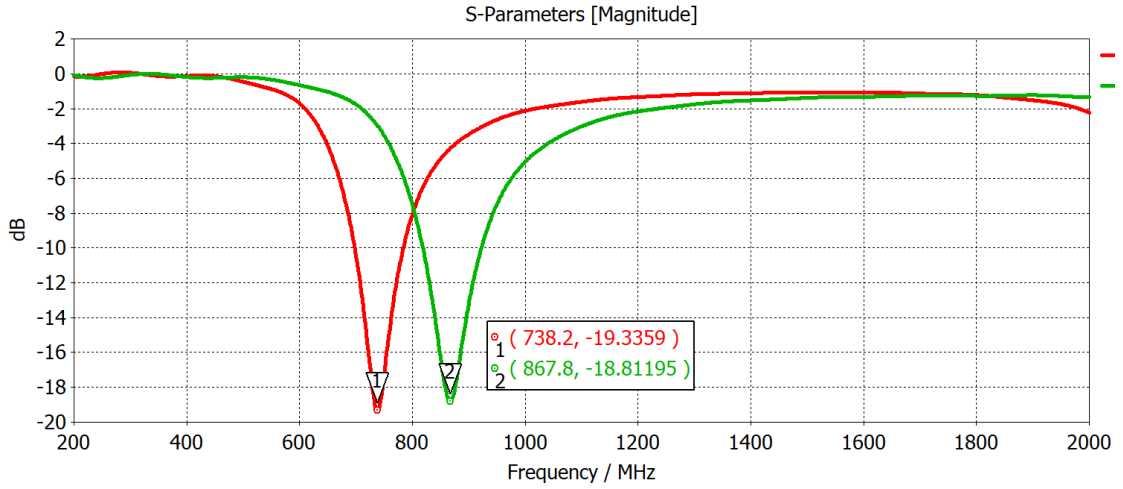


Figure 4.8: S_{11} of optimized simple planar dipole antenna (green) vs. before optimization (red)

4.2 Design of a planar dipole antenna with Balun

After proving that CST Studio Suite is an appropriate simulation tool for this research, the design phase of the six antenna topologies began, starting by the planar dipole antenna. The simple planar dipole antenna that was previously designed does not work in a real life testing environment because the tests carried out in chapter 5 will be done in an anechoic chamber. The feeding of the mock PCBs to be tested will be fabricated from the geometries simulated in this chapter and will be fed through 50 Ohm coaxial cables. These cables are naturally an unbalanced structure, and cannot be connected to a balanced structure, such as a dipole antenna, without using a Balun. Here we will design a planar dipole antenna with an integrated balun.

Initial geometry

The initial geometry of the antenna was taken from an article by Votis and Christofilakis[29]. In this article, the authors describe the design and experimental results of a planar 2.4 GHz dipole antenna. This dipole antenna integrates the Balun into the same printed circuit as the dipole and will be the base for our geometry. The objective is to use this geometry in CST Studio to validate their design. Once verified, the design will be scaled to 868 MHz and simulated again.

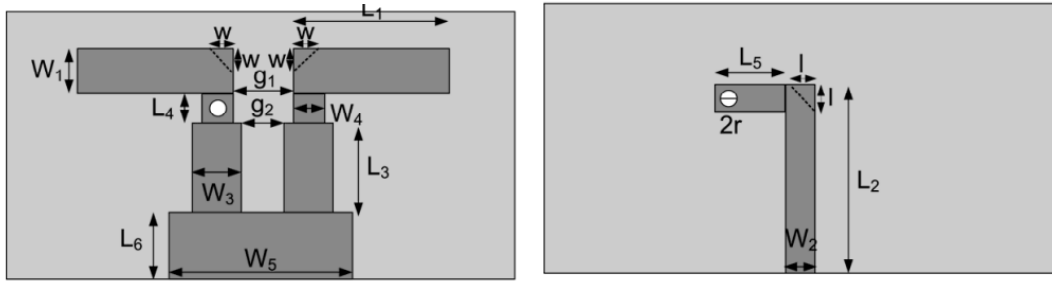


Figure 4.9: Antenna geometry a) Top Side b) Bottom Side

Parameter	Values
Dipole strips	L1 = 20.8 mm W1 = 6 mm g1 = 3 mm
Microstrip Balun	L2 = 32 mm L3 = 16 mm L4 = 3 mm L5 = 3 mm W2 = 2 mm W3 = 5 mm W4 = 3 mm g2 = 1 mm
Via radius	r = 0.375 mm
Ground plane	L6 = 12 mm W5 = 17 mm
Side of microstrip bend	l variable (0 mm – 3 mm)
Side of dipole's arms in the gap	w variable (0 mm – 3 mm)

Figure 4.10: Dimensions of initial dipole antenna with Balun

The geometry, described in Figure 4.9 and with its dimensions in Figure 4.10, was modeled in CST Studio exactly as described in the article, making sure to center the feed line on the Balun arm so it behaves correctly as a microstrip with the Balun arm as its ground plane. This model, shown in Figure 4.11, was then simulated.

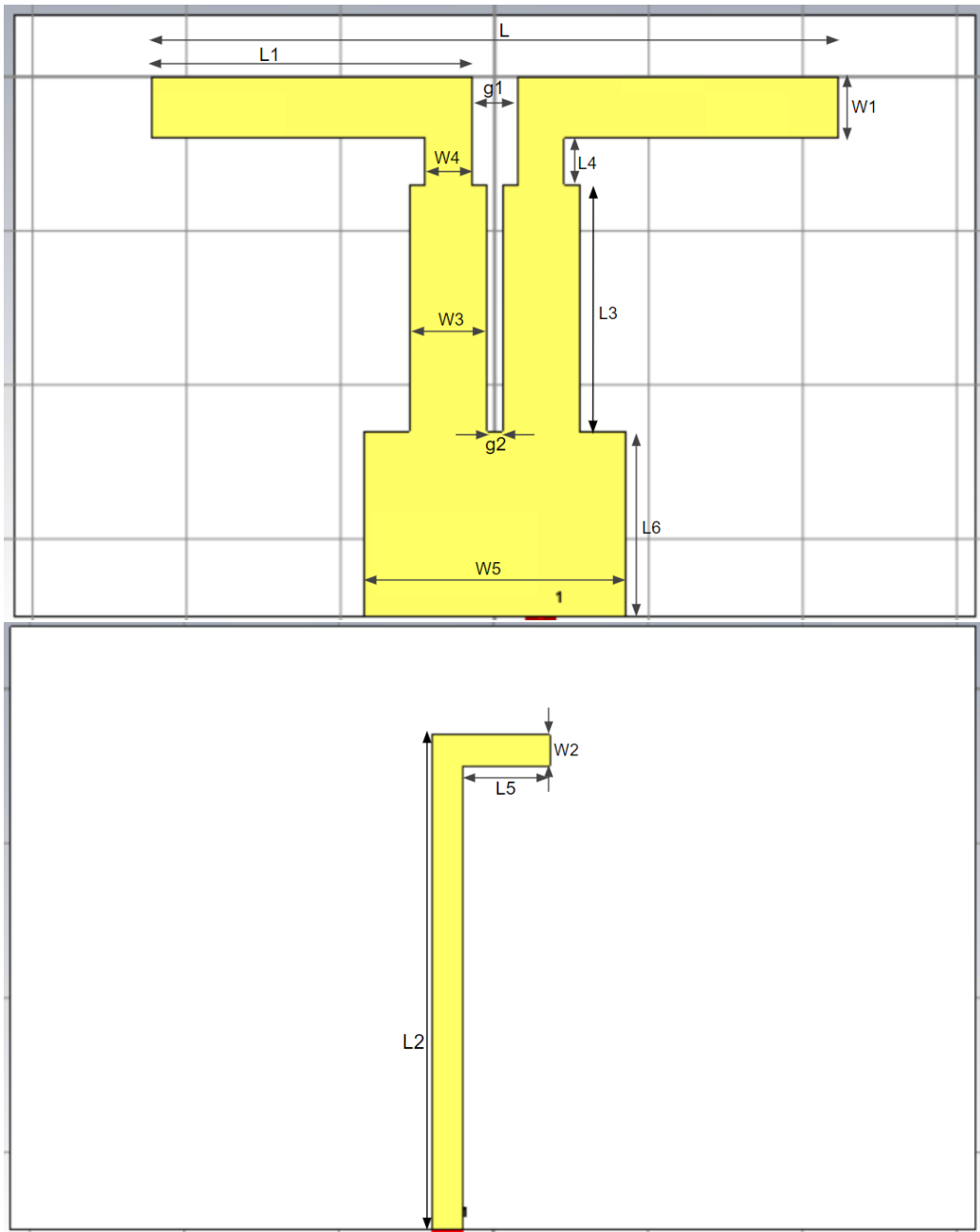
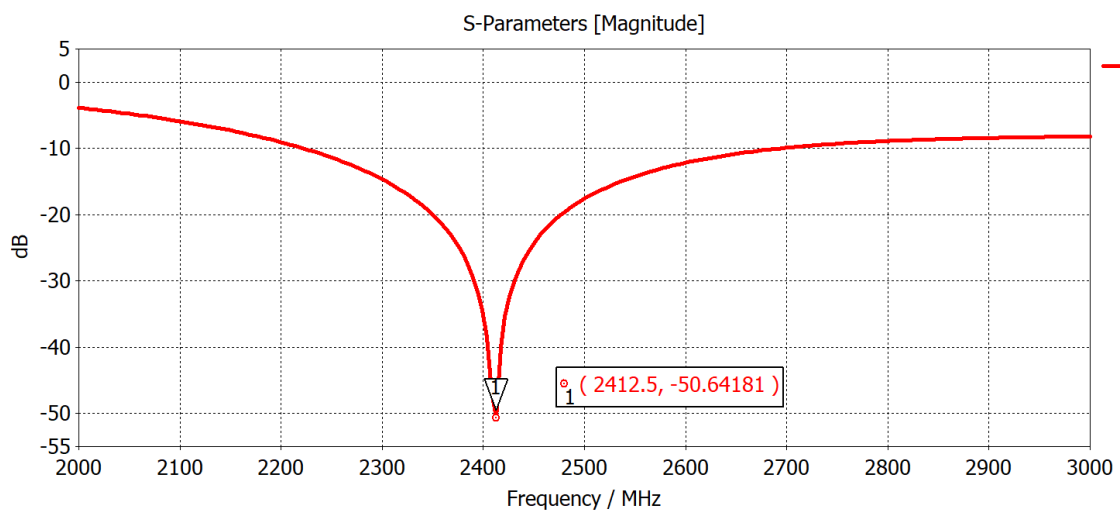


Figure 4.11: Initial geometry: 2.4 GHz antenna with Balun

Parameter	Dimension (mm)
Overall Dipole Length (L)	133.449
g1	5.156
g2	1.718
Length of each arm (L1)	20.8
L2	32
L3	16
L4	3
L5	5.667
L6	12
W1	4
W2	2
W3	5
W4	3
W5	17

Table 4.1: Dimensions of 2.4 GHz antenna with Balun



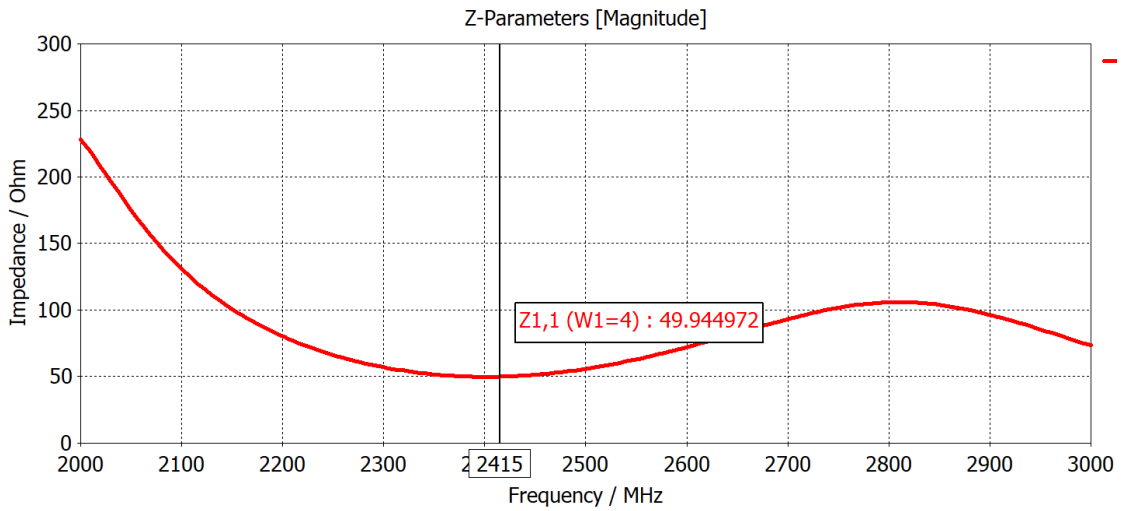
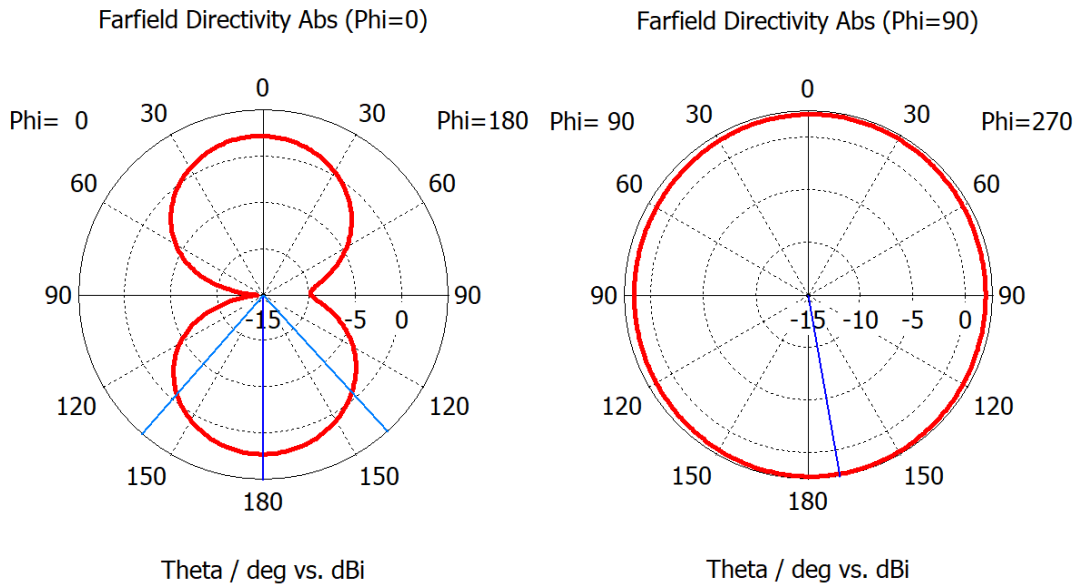


Figure 4.12: Simulation results a) S_{11} b) Input impedance

As seen in Figure 4.12, the antenna's resonant frequency is at 2.415 GHz and the input impedance at this frequency is $49.94\ \Omega$. This proves the design's validity as the obtained results match those described by Votis and Christofilakis[29]. In Figure 4.13 we can see that the antenna's radiation pattern matches that of an omnidirectional antenna. With these results in mind we will attempt to scale the design for the same performance but at a resonant frequency of 868 MHz



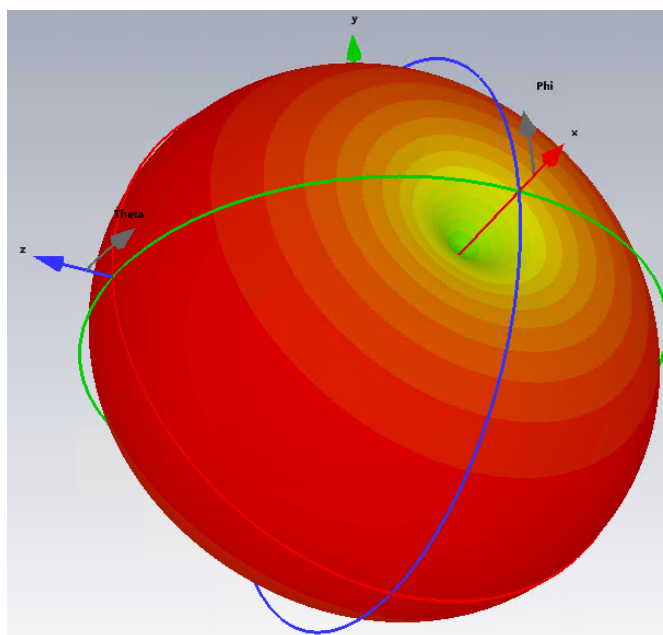


Figure 4.13: Simulated radiation pattern: a) 2D cut of radiation pattern - XY plane b) 2D cut of radiation pattern - YZ plane c) 3D radiation pattern.

Scaling, optimization and final results

After proving that the 2.4 GHz antenna's simulation gave desired results, the whole antenna was scaled up to 868 MHz, by scaling the geometry by a factor of 2.76 given from $2.4 \text{ GHz} / 868 \text{ MHz} = 2.76$, while maintaining the aspect ratio of the initial antenna. After initial simulations, we observed that the antenna no longer had the same performance as the 2.4 GHz antenna, and an optimization of the dimensions had to be carried out. This was because the antenna's sections no longer had the same impedance due to their width being scaled as well. The final antenna dimensions are presented in Table 4.2, and refer to Figure 4.14.

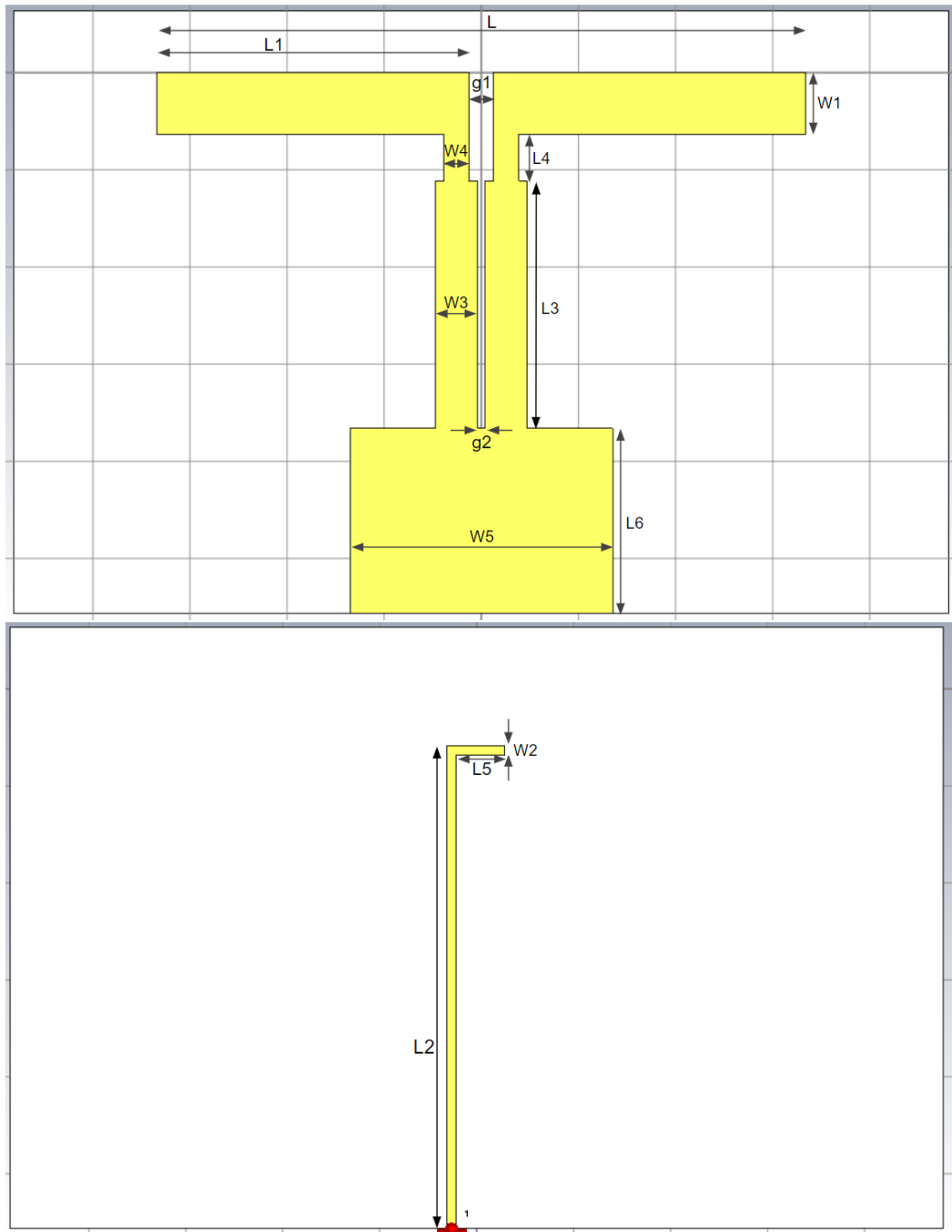
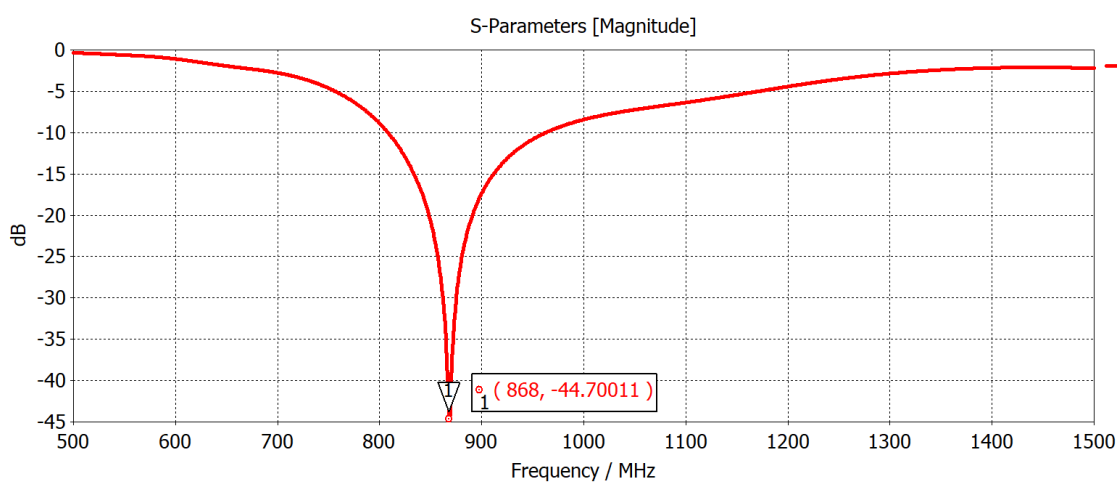


Figure 4.14: Optimized 868 MHz antenna with Balun

Parameter	Dimension (mm)
Overall Dipole Length (L)	133.449
g1	5.156
g2	1.718
Length of each arm (L1)	64.147
L2	101.809
L3	50.905
L4	9.545
L5	9.991
L6	38.179
W1	12.726
W2	1.905
W3	8.590
W4	5.154
W5	54.986

Table 4.2: Dimensions of 868 MHz antenna with Balun

When simulating this antenna geometry we got a resonant frequency of exactly 868 MHz with a S_{11} of -44.7 dB, and an input impedance of 50.29Ω at that frequency:



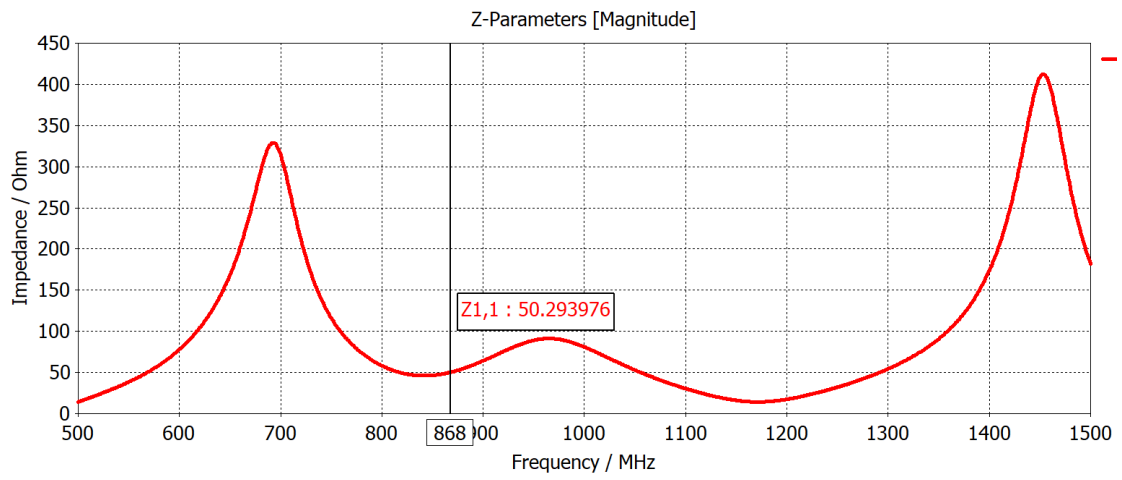
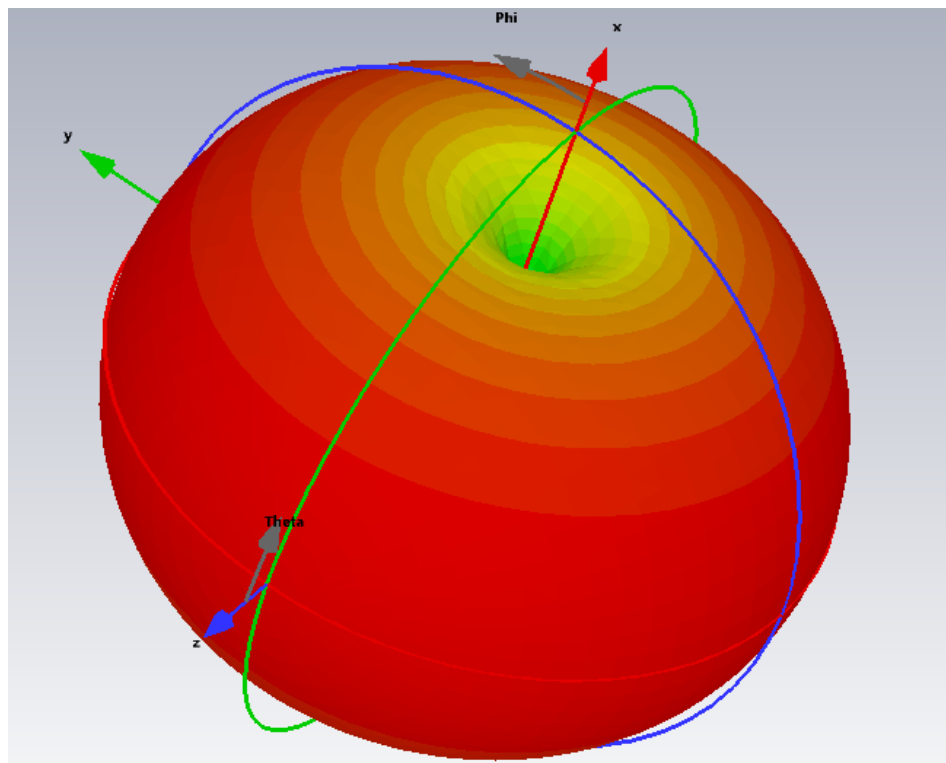


Figure 4.15: Simulation results a) S_{11} b) Input impedance

And a quasi omnidirectional radiation pattern:



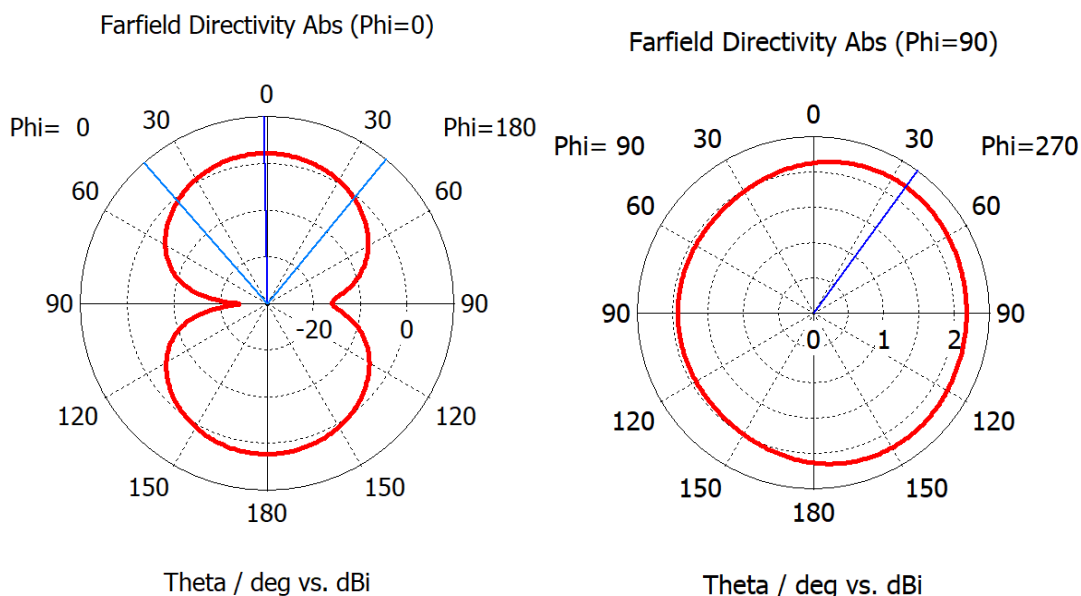


Figure 4.16: Simulated radiation pattern a) 3D radiation pattern. b) 2D cut of radiation pattern - XY plane c) 2D cut of radiation pattern - YZ plane

4.3 Design of a planar monopole antenna

Next, a planar monopole antenna was designed. This model will be the basis for all other topologies since they will all be modifications of the monopole. Note that all following topologies will have a ground plane in the bottom layer that mirrors the one on the top layer.

Initial geometry and simulation

The initial geometry was taken from the simple planar dipole simulated previously in section 4.1. Taking into account the adjustment factor of 0.848896 the antenna in Figure 4.17 was designed with the following dimensions:

Parameter	Dimension (mm)
X	80
Y	80
L	69.78
W	0.8

Table 4.3: Dimensions of initial Monopole antenna

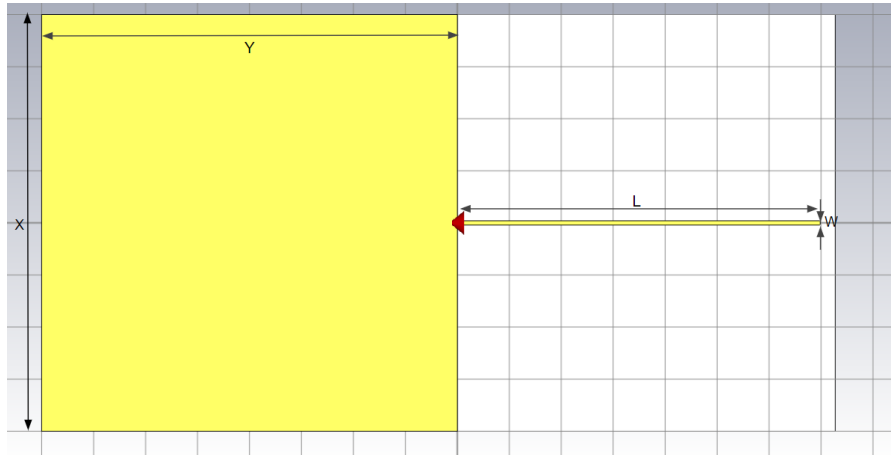


Figure 4.17: Planar monopole antenna

The X and Y values were chosen to reflect an appropriate size relative to the sensor node PCB, as well as being big enough to provide a sufficient ground plane for the monopole. For this initial topology, the length of the monopole arm L was chosen to be the same as the planar dipole arm length, or $\lambda/4 * 0.952 * 0.848896$.

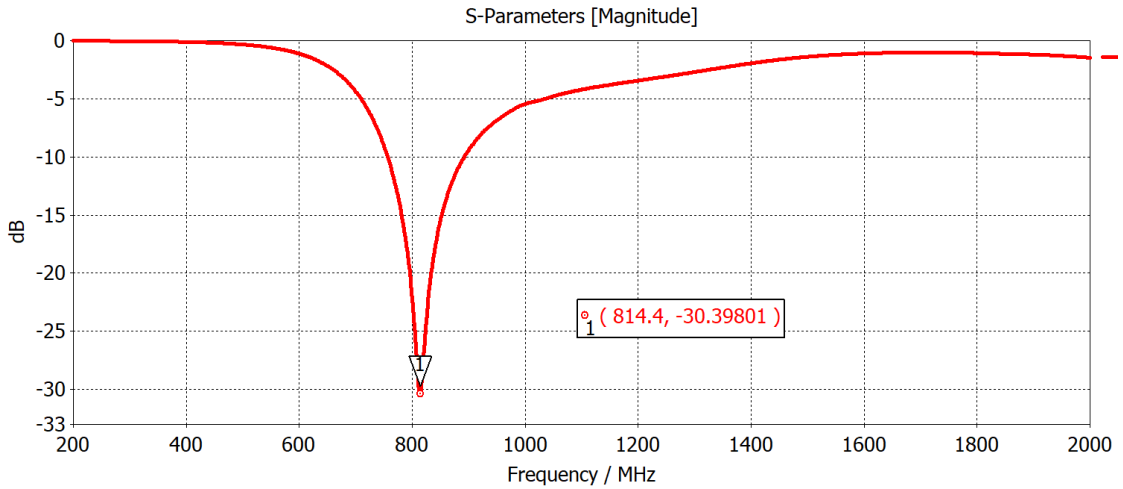


Figure 4.18: S_{11} of initial planar monopole antenna

Figure 4.18 shows that the initial structure for the planar monopole antenna is not resonant at 868 MHz, but at 814.4 MHz. This can be explained by the change in dielectric dimension when compared to the planar dipole antenna in Figure 4.6. By having a bigger dielectric with respect to the radiating element, the length of the antenna is virtually elongated even more. Due to this, the antenna length must be scaled to optimize the antenna to resonate at 868 MHz.

Optimization and final results

To optimize the monopole antenna to be resonant at 868 MHz, the arm length (L) was scaled by a factor of 0.92 to correct the frequency offset. Table 4.4 shows the final dimensions, and Figure 4.19 the obtained simulation results.

Parameter	Dimension (mm)
X	80
Y	80
L	64.15
W	0.8

Table 4.4: Dimensions of optimized Monopole antenna

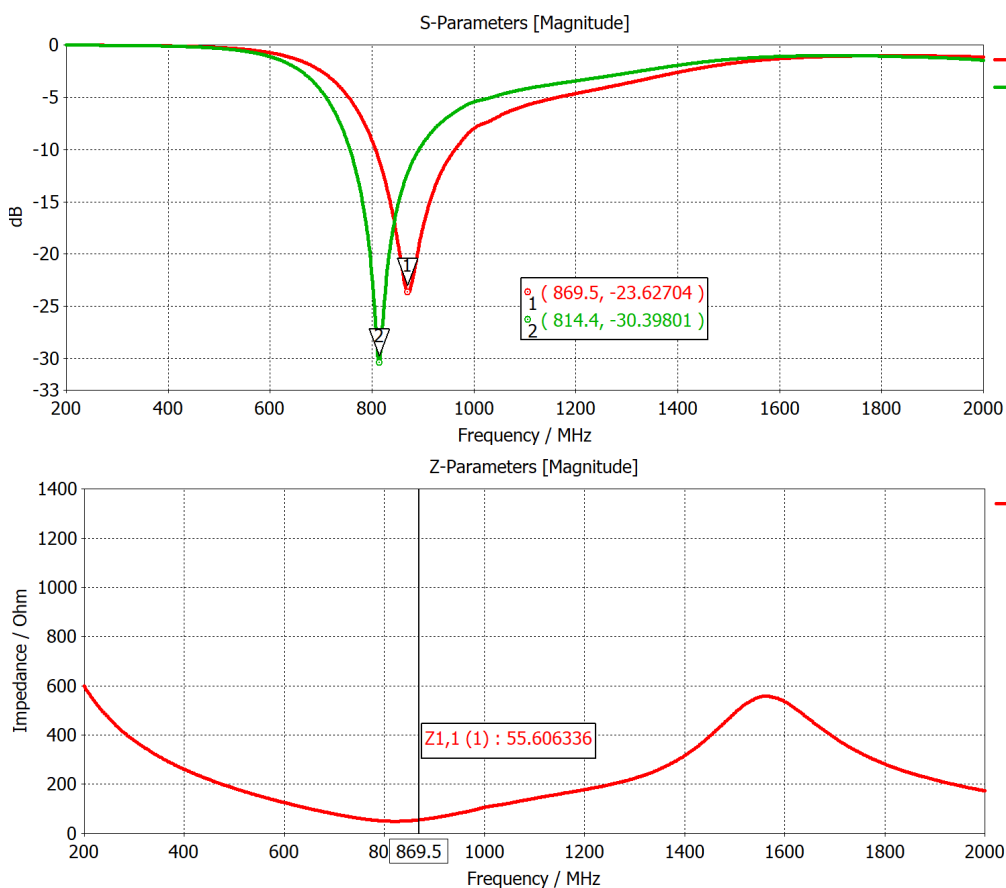


Figure 4.19: Simulation results a) S_{11} (Red optimized, green initial) b) Input impedance

Figure 4.19 shows that the antenna was not perfectly optimized, with a resonant frequency of 869.2 MHz and an input impedance of 55.6Ω , which is an unmatched antenna. And Figure 4.20 shows its radiation pattern which is quasi-omnidirectional, with an oval XY cut instead of a circular one, but still sufficiently omnidirectional.

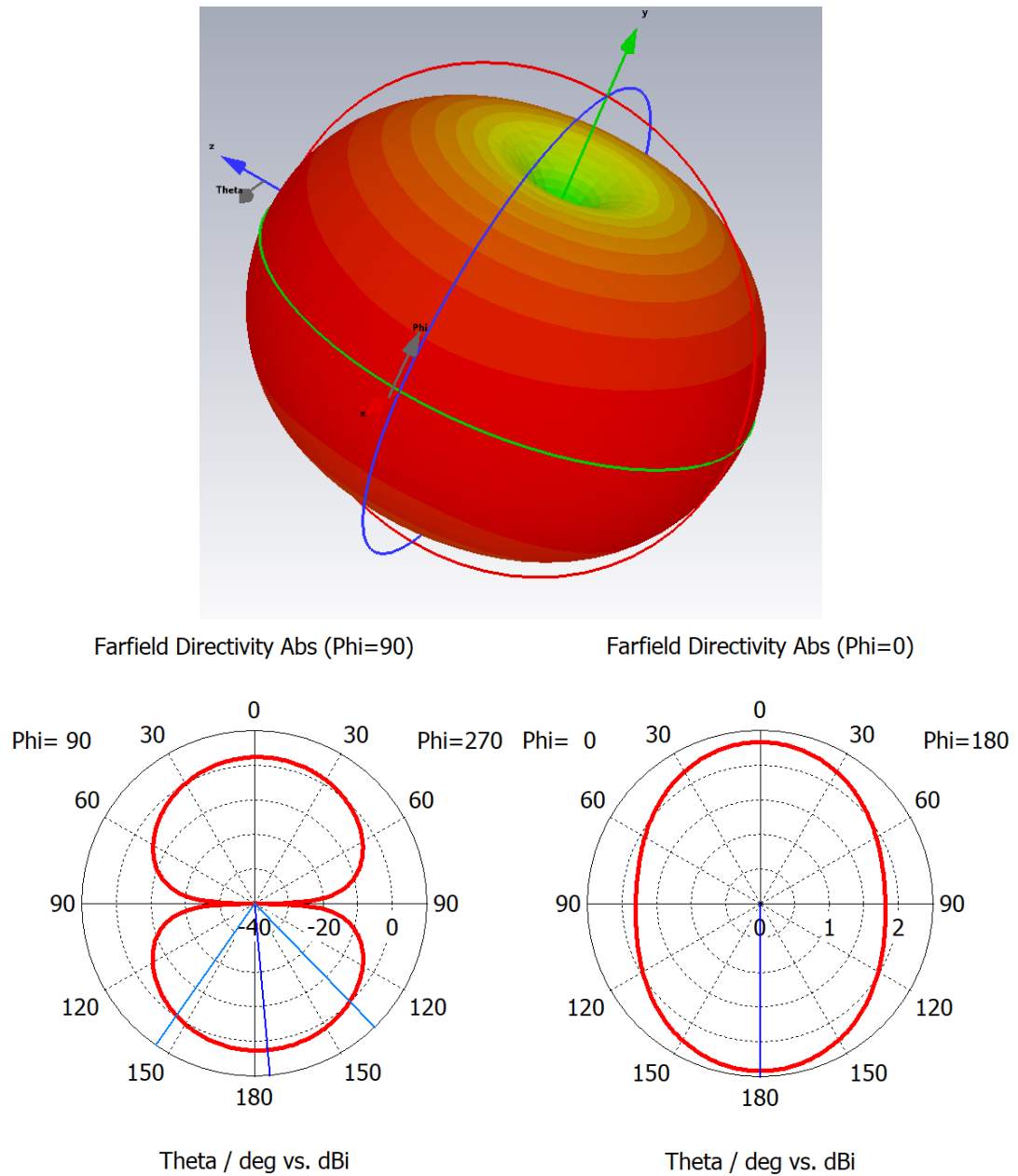


Figure 4.20: Simulated radiation pattern a) 3D radiation pattern. b) 2D cut of radiation pattern - XY plane c) 2D cut of radiation pattern - YZ plane

4.4 Design of an offset planar monopole antenna

The goal with this topology was to copy the monopole antenna just designed but shift the radiating element from the center of the substrate to one side. The objective is to make space for the bend necessary to design the inverted-L antenna, and see if any further scaling of the monopole length has to be done due to the effect of being closer to the edge of the board.

Initial geometry and simulation

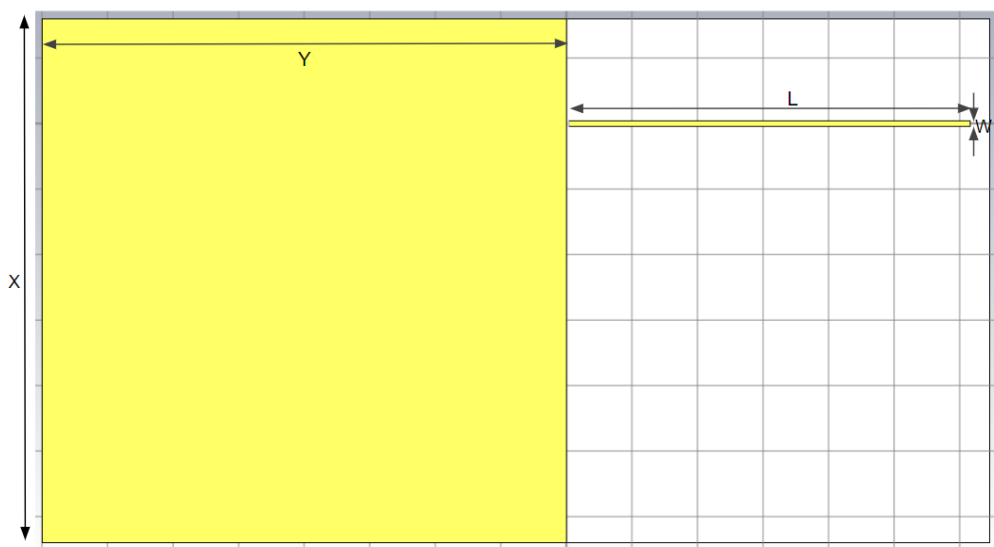


Figure 4.21: Offset planar monopole antenna

The initial geometry was taken from the same dimensions as in Table 4.4, but with the radiating element offset by 60% of the distance between the center of the structure and the side. The structure was then simulated.

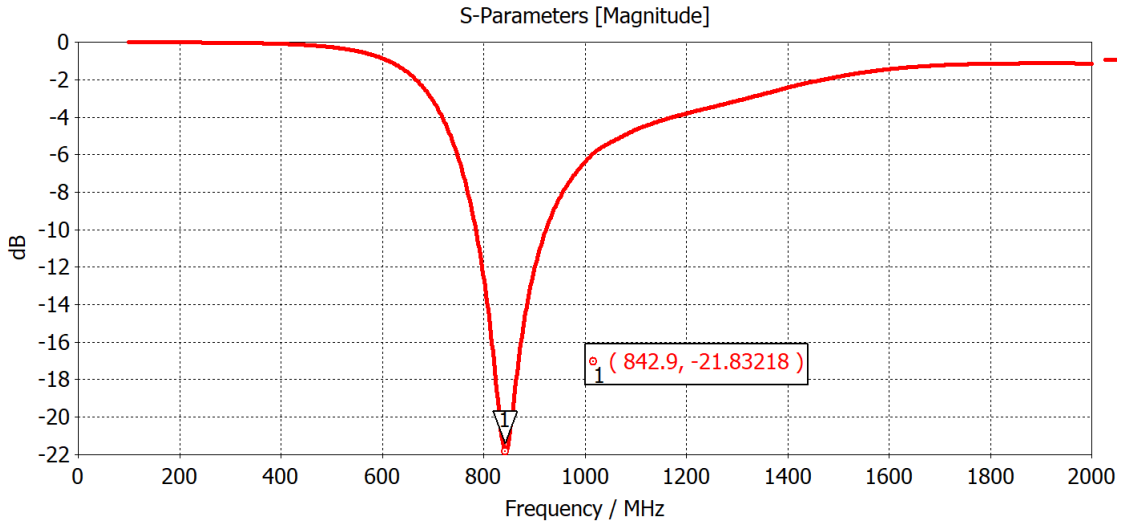


Figure 4.22: S_{11} of initial planar monopole antenna

Figure 4.22 shows that the initial structure for the offset monopole antenna is not resonant at 868 MHz, but at 842.9 MHz. By offsetting the antenna, the dielectric’s effect changes, and consequently, the resonant frequency changes. Due to this, the antenna length must be scaled to optimize the antenna to resonate at 868 MHz.

Optimization and final results

To optimize the offset monopole antenna to be resonant at 868 MHz, the arm length (L) was scaled by a factor of 0.96 to correct the frequency offset. Table 4.5 shows the final dimensions, and Figure 4.23 the obtained simulation results (in red) of this optimized geometry.

Parameter	Dimension (mm)
X	80
Y	80
L	61.58
W	0.8

Table 4.5: Dimensions of optimized offset Monopole antenna

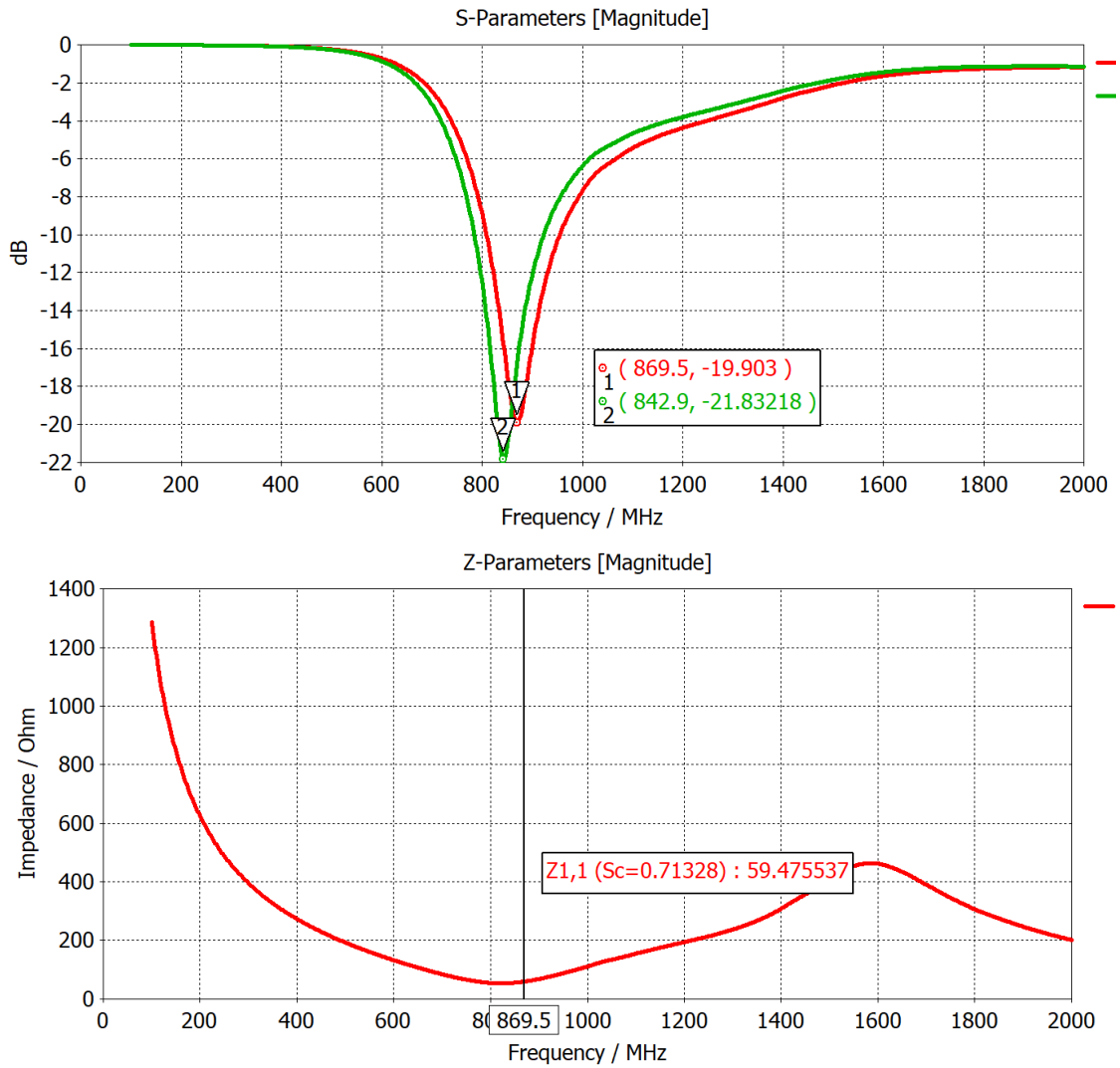
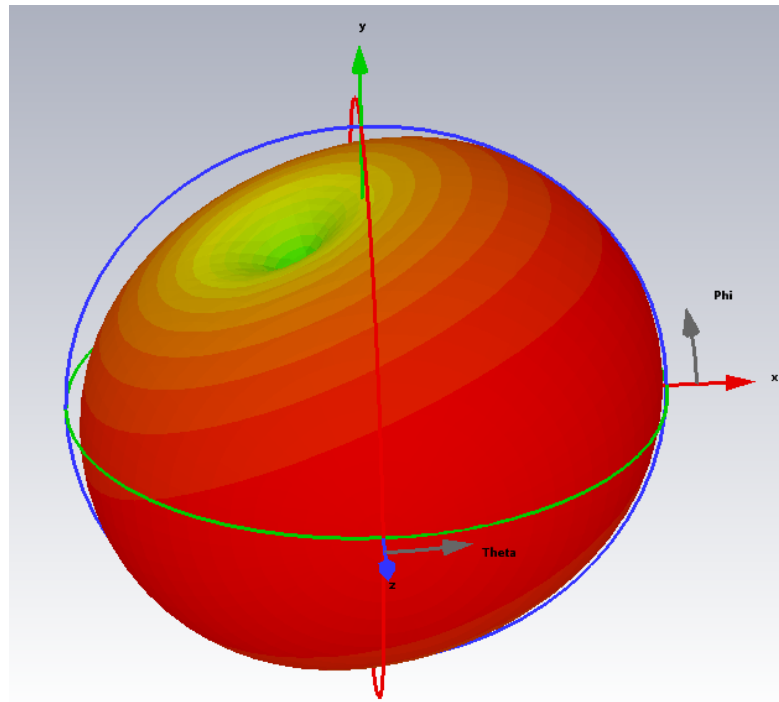


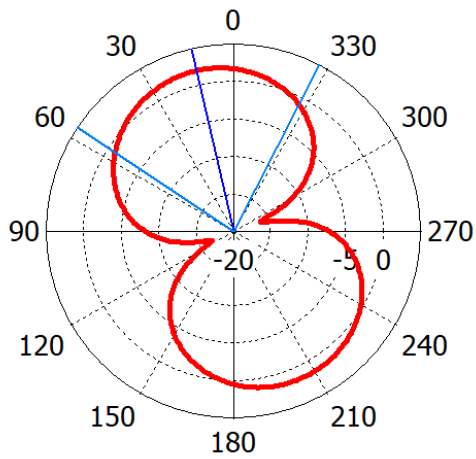
Figure 4.23: Simulation results a) S_{11} (Red optimized, green initial) b) Input impedance

Figure 4.23 shows that the antenna was correctly optimized, with a resonant frequency of 869.2 MHz and an input impedance of 59.5Ω . and Figure 4.24 shows its radiation pattern which is quasi-omnidirectional, but tilted towards the side the radiating element is located at (Positive Phi direction). The XY cut of the radiation pattern shows that it is tilted by about 30 degrees. Due to this, the YZ plane cut has to be tilted by these 30 degrees to show the real radiation pattern of the antenna which has an oval shape, meaning it will have some more directivity normal to the faces of the board and less towards the edges.

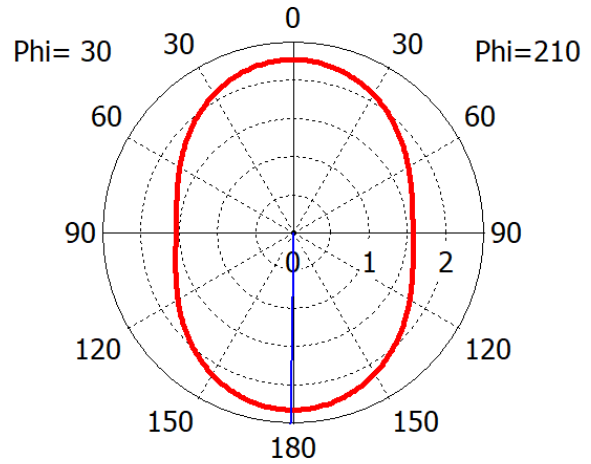


Farfield Directivity Abs (Theta=90)

Farfield Directivity Abs (Phi=30)



Phi / Degree vs. dBi



Theta / Degree vs. dBi

Figure 4.24: Simulated radiation pattern a) 3D radiation pattern. b) 2D cut of radiation pattern - XY plane c) 2D cut of radiation pattern - YZ plane tilted 30 degrees

4.5 Design of a planar inverted-L antenna

The next topology to be designed was a planar inverted-L antenna, which bends the monopole arm at some part of its length to make it more compact, while keeping the same resonant frequency. The trade-off for this compactness is losing radiation power and having a very low input impedance with respect to the planar monopole.

Initial geometry and simulation

The initial geometry was taken from the same dimensions as in Table 4.5, but with a bend in the monopole's length. The point chosen for the bend was 30 % down the length of the monopole from the feed point. Figure 4.25 shows the initial geometry for this monopole, and Table 4.6 its dimensions.

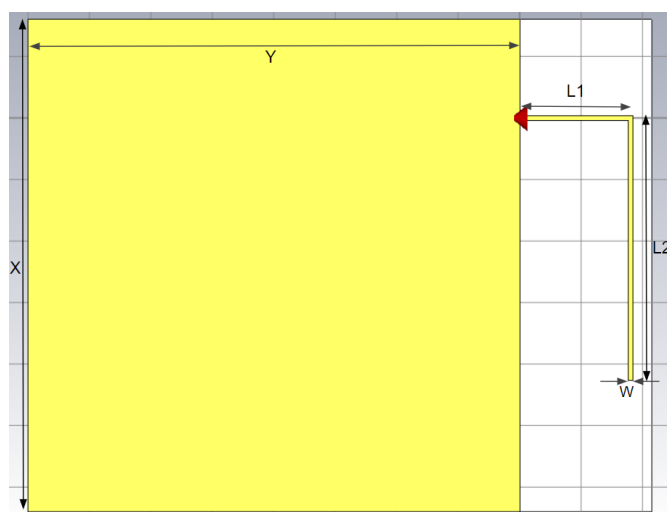


Figure 4.25: Initial planar inverted-L antenna

Parameter	Dimension (mm)
X	80
Y	80
L1	18.48
L2	43.11
W	0.8

Table 4.6: Dimensions of initial inverted-L antenna

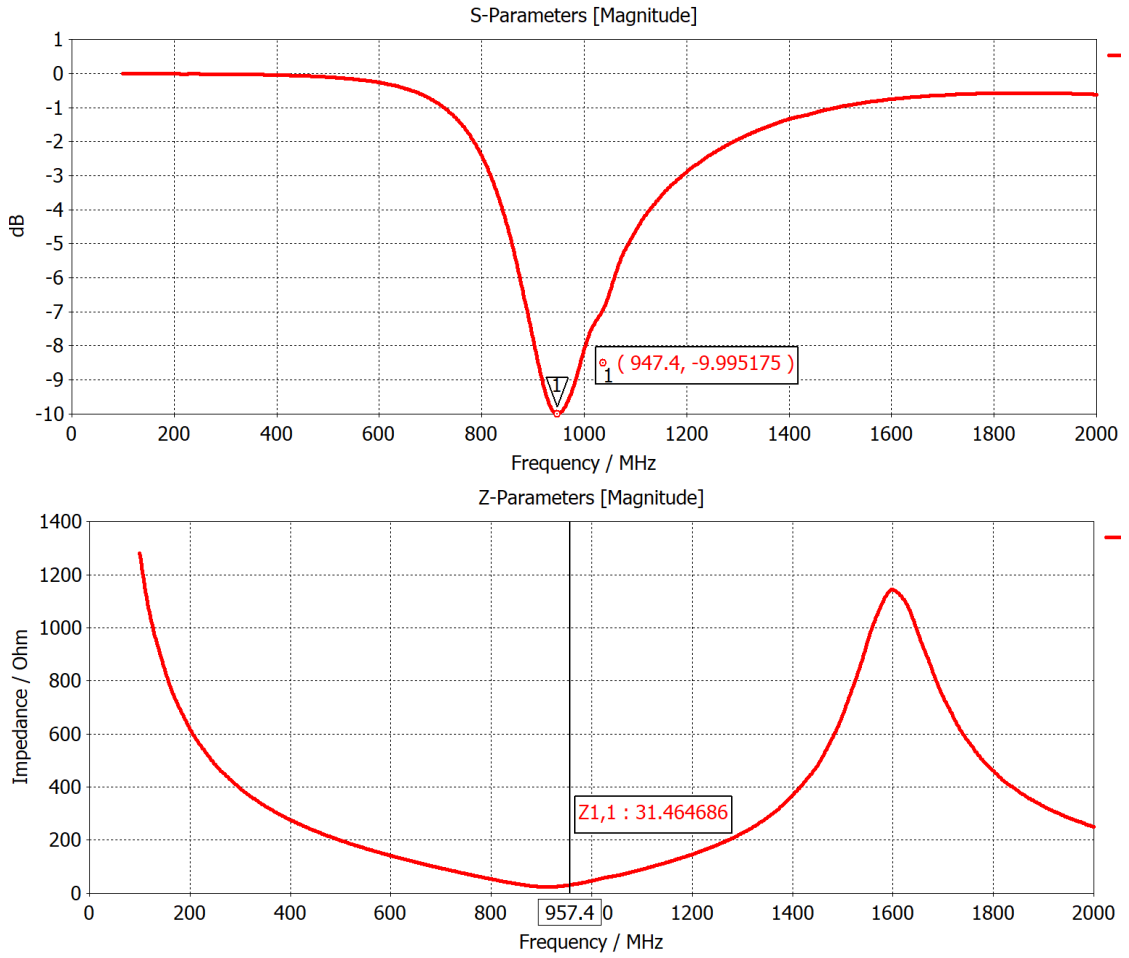


Figure 4.26: a) S_{11} and b) input impedance of initial planar monopole antenna

Figure 4.26 shows that the initial structure for the inverted-L antenna is not resonant at 868 MHz, but at 947.4 MHz. By bending the antenna and making it more compact, the dielectric's size is smaller and this causes a lesser effect on the resonant frequency of the antenna. This causes the frequency to increase since the antenna is no longer being as lengthened virtually as in the monopole. We can also observe that the input impedance is very low at 31.5 Ω . When connected to a 50 Ω connector this would cause reflections due to the mismatched impedance and that is why the S_{11} parameter only goes to -10 dB, instead of the -20 to -30 range we are used to seeing on the other antennas. Due to this, the antenna length must be scaled to optimize the antenna to resonate at 868 MHz, as well as the geometry to increase the input impedance.

Optimization and final results

To optimize the offset monopole antenna to be resonant at 868 MHz and have an input impedance of $50\ \Omega$, a new geometry was proposed in Figure 4.27

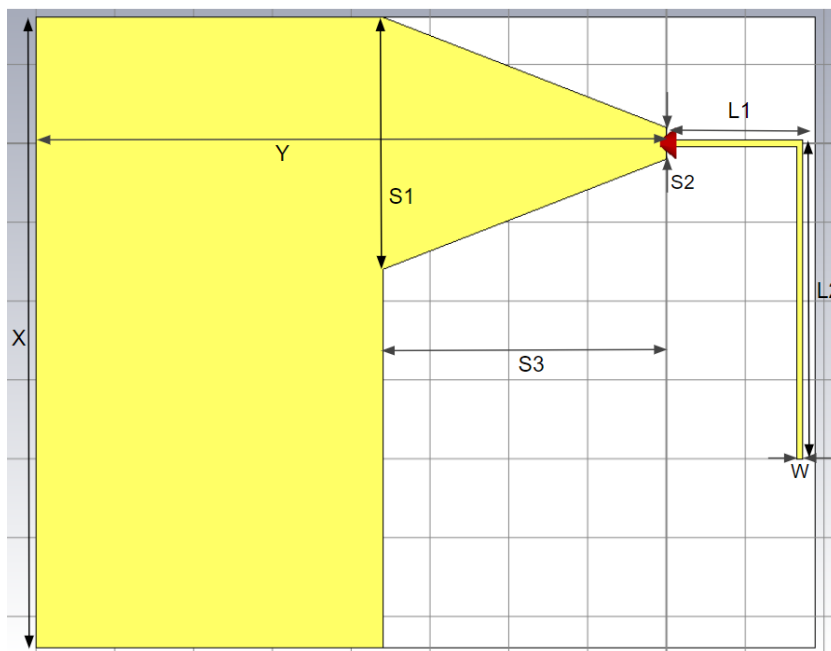


Figure 4.27: Modified planar inverted-L antenna

Parameter	Dimension (mm)
X	80
Y	80
L1	17.32
L2	40.41
W	0.8
S1	32
S2	4
S3	36

Table 4.7: Dimensions of modified inverted-L antenna

The geometry in Figure 4.27 shows an angled ground plane, which is mirrored in

the bottom ground plane. The added distance from the parallel section to the ground plane makes it behave less like a perfect transmission line and this increases the input impedance. However, this also changes the resonant frequency of the antenna due to the parallel section radiating slightly, and the whole antenna length has to be optimized as well. Changing the antenna length also changes the input impedance, so these two variables of angle of the ground plane and length of the antenna are dependent on each other, and have to be optimized together to achieve an antenna resonant at 868 MHz and 50Ω at that frequency. This was done by running parametric sweeps in CST Studio, a tool that allows running multiple simulations while varying the value of physical dimensions of the antenna. The final dimensions after the optimization are shown in Table 4.7.

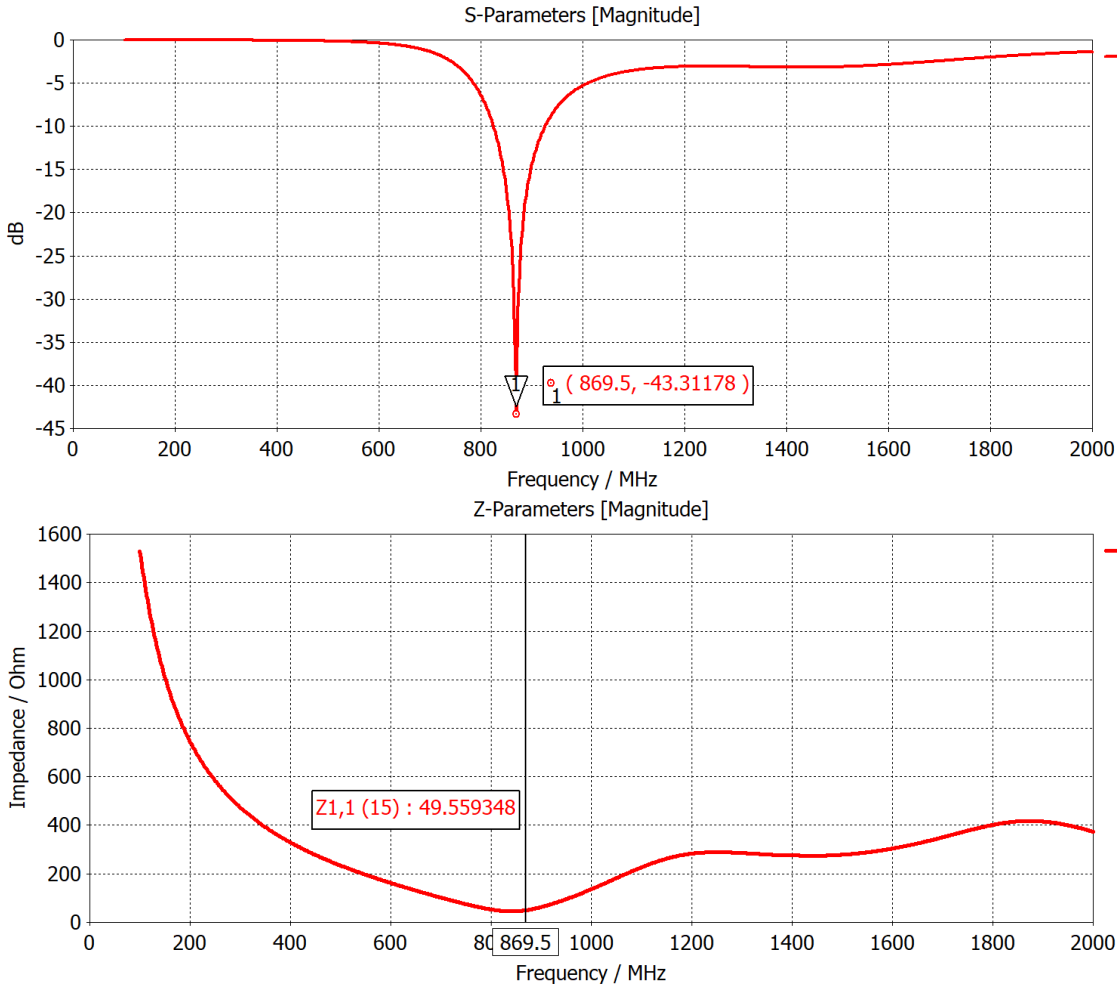


Figure 4.28: Simulation results a) S_{11} b) Input impedance

Figure 4.28 shows that the antenna was correctly optimized, with a resonant frequency of 869.5 MHz and an input impedance of 49.6Ω . The S_{11} parameter shows that the antenna is perfectly tuned at 869.5 MHz by having a value of -43.3 dB, the second best coupling of the antennas designed thus far after the dipole with balun. Figure 4.29 shows that, as the offset monopole, the radiation pattern is omnidirectional and tilted in the positive phi direction (at $\theta = 90^\circ$).

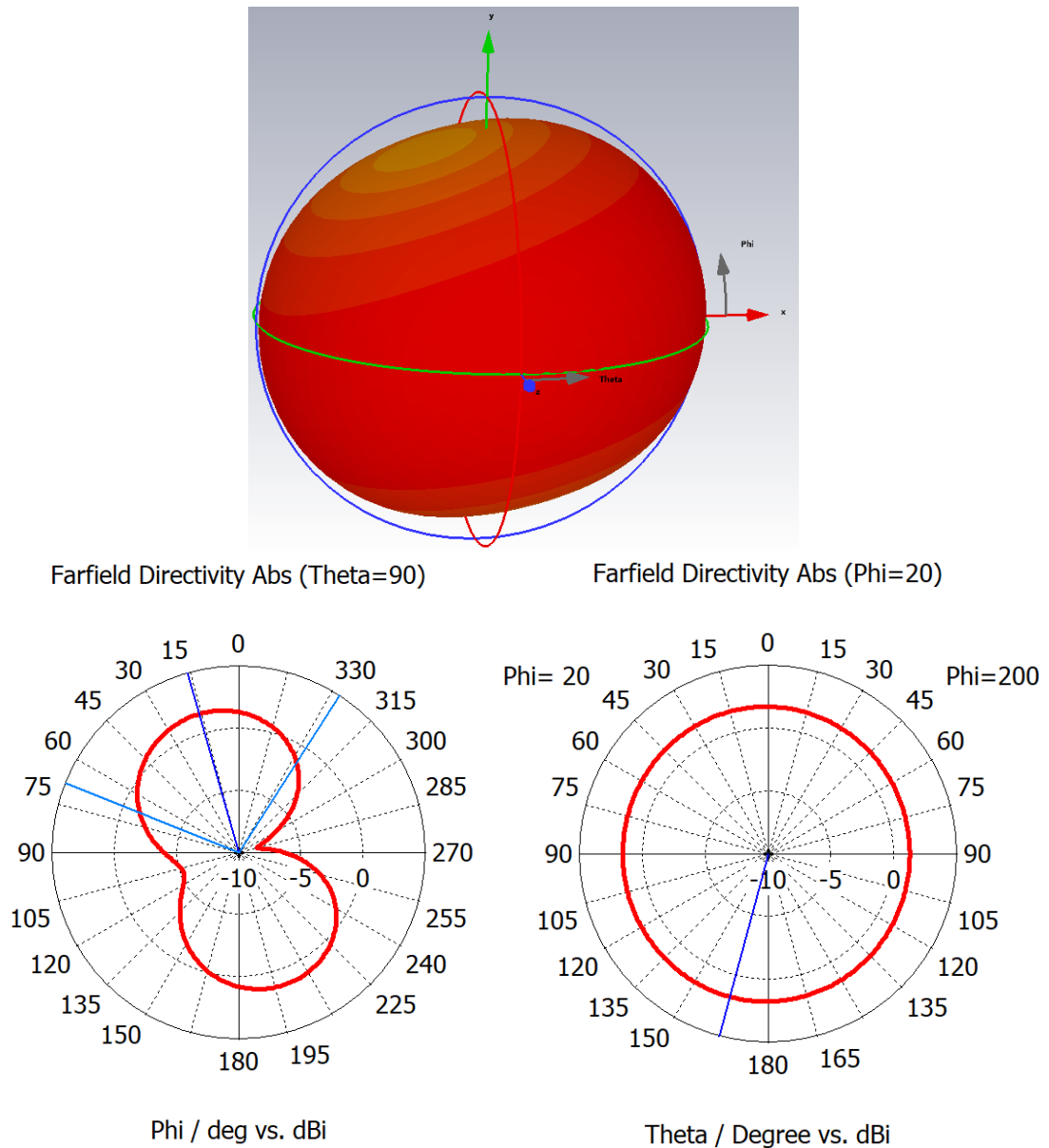


Figure 4.29: Simulated radiation pattern a) 3D radiation pattern. b) 2D cut - XY plane c) 2D cut - YZ plane tilted 20 degrees

4.6 Design of a planar meandered inverted-L antenna

The initial geometry was taken from the same dimensions as in Table 4.6, but with a bend in the inverted-L's parallel section. The point chosen for the bend was 60 % down the length of the parallel section from the initial L-bend. Figure 4.30 shows the initial geometry for this inverted-L antenna, and Table 4.8 its dimensions. Note that now, since the antenna is more compact, the offset to the side of the board is 30 % instead of 60 %.

Initial geometry and simulation

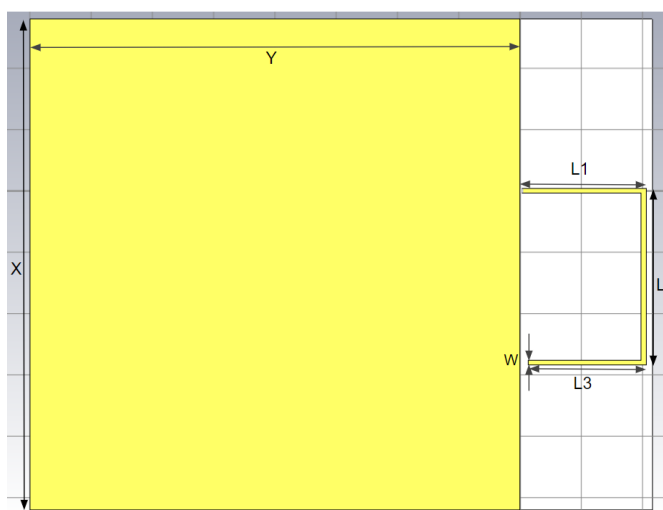


Figure 4.30: Bent inverted-L antenna

Parameter	Dimension (mm)
X	80
Y	80
L1	20.38
L2	28.53
L3	19.02
W	0.8

Table 4.8: Dimensions of initial bent inverted-L antenna

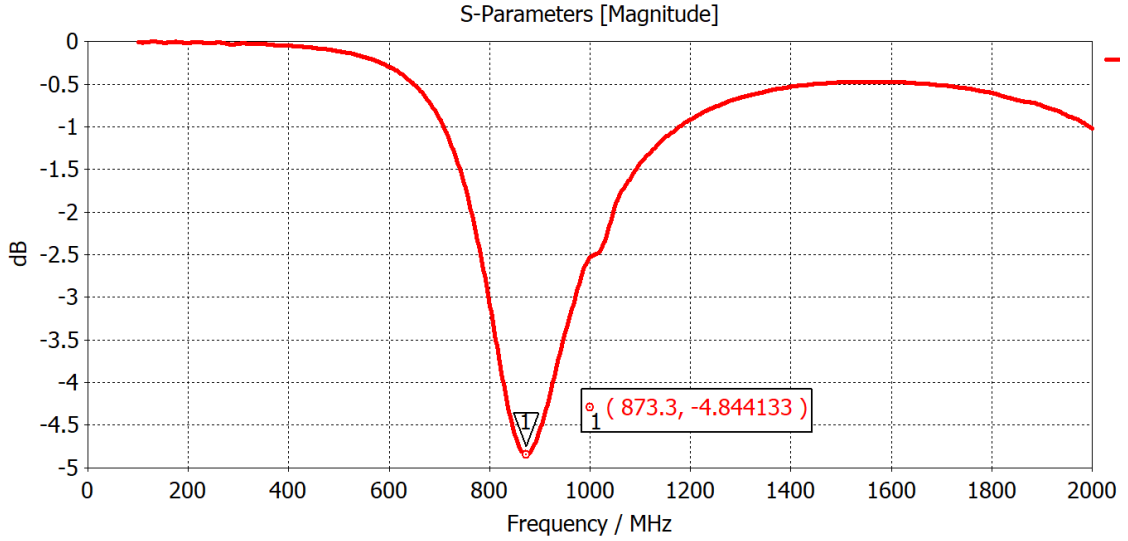


Figure 4.31: S_{11} initial planar monopole antenna

Figure 4.31 shows that the initial structure for the inverted-L antenna is not resonant at 868 MHz, but at MHz. By bending the antenna again and making it more compact, the new bent section and the reduced offset increase the resonating frequency, so the overall length has to be increased.

Optimization and final results

To optimize the offset monopole antenna to be resonant at 868 MHz, the total length was scaled up slightly. Table 4.9 shows the final dimensions, and Figure 4.32 the obtained simulation results (in red) of this optimized geometry.

Parameter	Dimension (mm)
X	80
Y	80
L1	20.59
L2	28.83
L3	19.22
W	0.8

Table 4.9: Dimensions of initial bent inverted-L antenna

Figure 4.23 shows that the antenna resonates at 867.6 MHz. As with the initial inverted-L antenna, we can see that the input impedance is very low, in this case, 18.69Ω . If this antenna were to be fabricated and tested with a 50Ω connector, the radiated power would be very low due to the mismatched impedance. The S_{11} value shows this by being only -4.78 dB. This topology will not be optimized for impedance matching since it is only a basis for the inverted-f topology, since the latter will not have an angled ground plane to match its impedance but a short circuit to the ground plane instead.

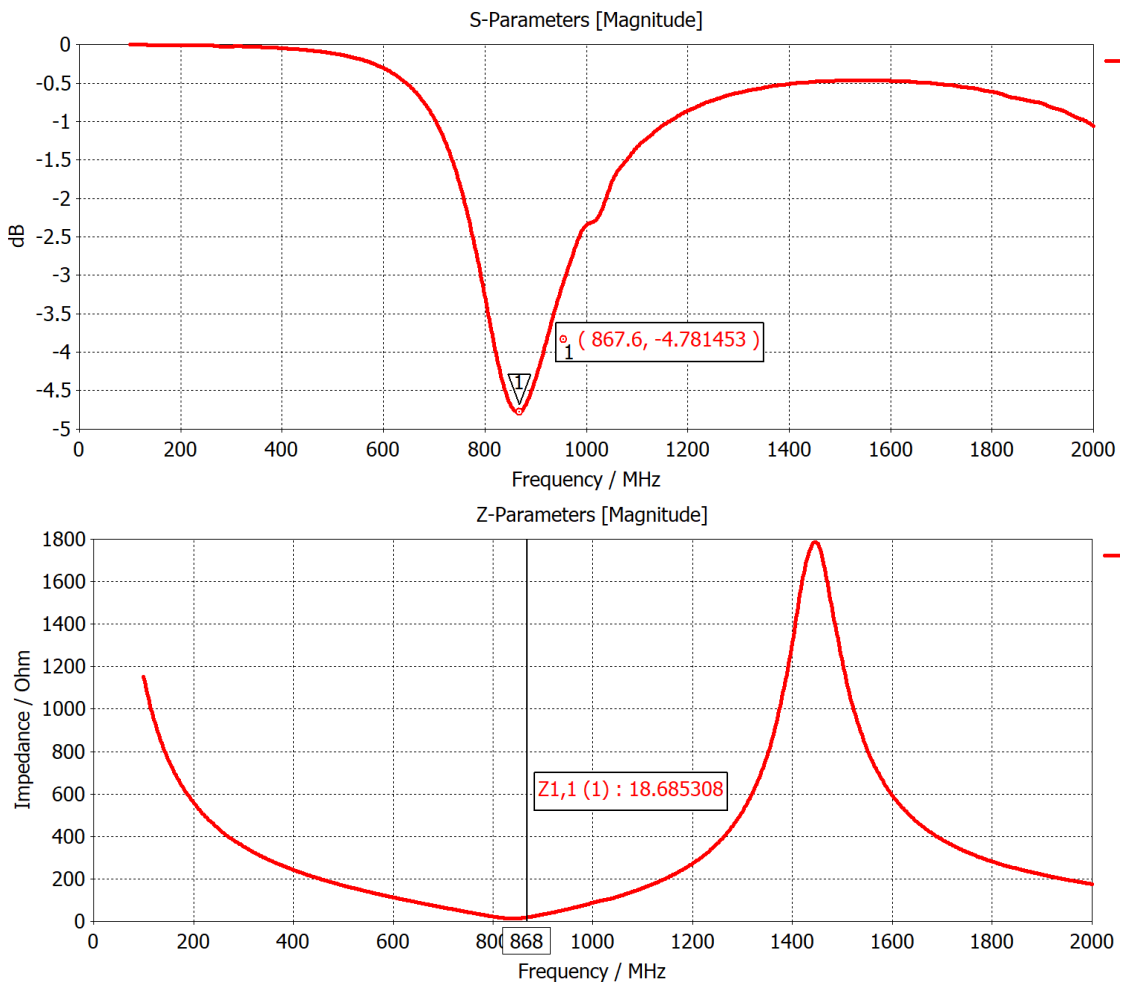


Figure 4.32: Simulation results a) S_{11} b) Input impedance

4.7 Design of a planar inverted-F antenna

The last topology to be designed was an inverted-F antenna. This type of antenna utilizes the monopole structure of an inverted-L antenna to radiate, but feeds the antenna at an intermediate point, leaving a section of the arm as an open circuit, like the inverted-L, while the other side is grounded. In RF, an open circuit behaves like a capacitor, and this is the reason the initial inverted-L antenna designed in Figure 4.25 had such a low impedance. The mismatch in impedance can be seen easily with the use of a smith chart:

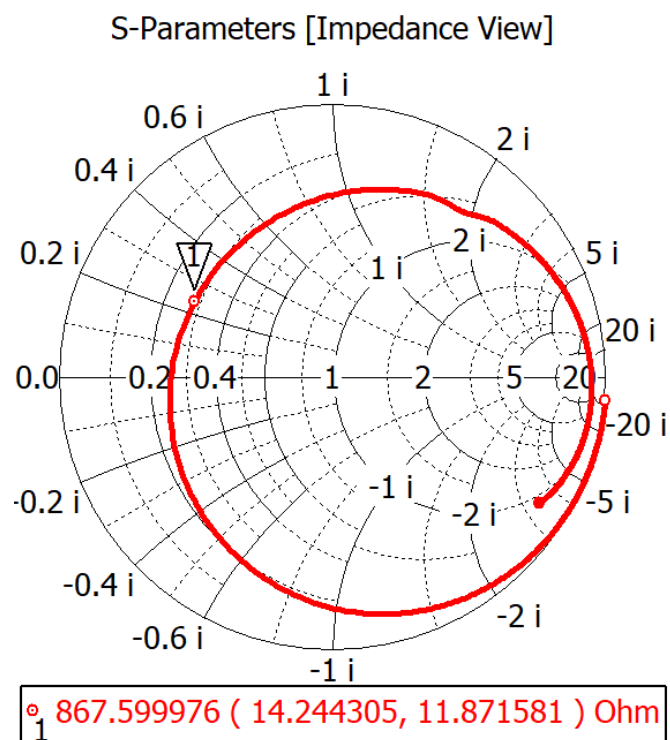


Figure 4.33: Smith chart of simulated bent inverted-L antenna

Figure 4.33 shows the impedance smith chart of the previously designed and optimized bent inverted-L antenna. At the resonant frequency, the complex impedance is $14.24 + j11.87 \Omega$. To counteract the effect of the capacitive element, an inductor may be used. This causes the imaginary part of the impedance to be cancelled out, and the antenna can be tuned to a purely real impedance of 50Ω for maximum radiation efficiency with correctly matched impedance. In the inverted-F antenna, the short circuit stub performs this task, behaving like an inductor in RF.

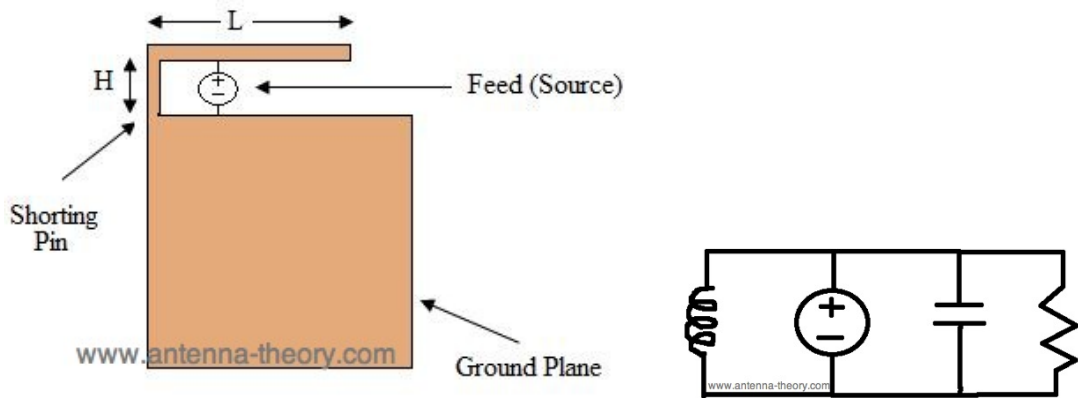


Figure 4.34: a) Inverted-F topology and b) equivalent circuit [30]

To remove the mismatch of the antenna's impedance with the $50\ \Omega$ port, the inverted-F antenna was designed.

Optimized geometry and simulation

When adding the short circuit stub, the length of the antenna's radiating element changes. This makes the system very complex since the length of the stub depends on the length of the antenna and the length of the antenna on the length of the stub, and renders the system very difficult to optimize analytically through calculations. As such, the optimization was carried out in CST Studio using the parametric sweep tool to simulate different dimensions of antenna and stub length until an optimized structure was found. Figure 4.35 shows the antenna design and Table 4.10 its dimensions.

Parameter	Dimension (mm)
X	80
Y	80
L1	21.72
L2	29.85
L3	19.90
L4	4.63
W	0.8

Table 4.10: Dimensions of optimized inverted-F antenna

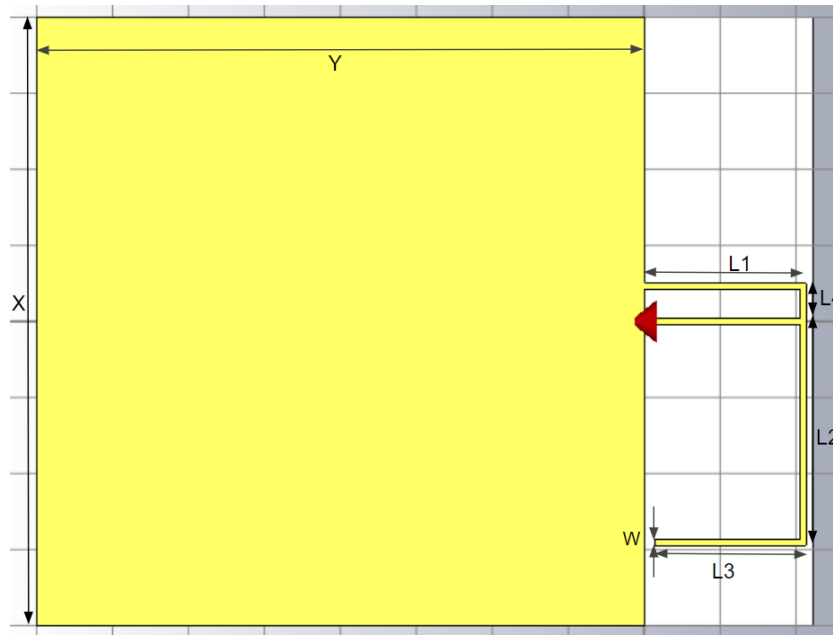
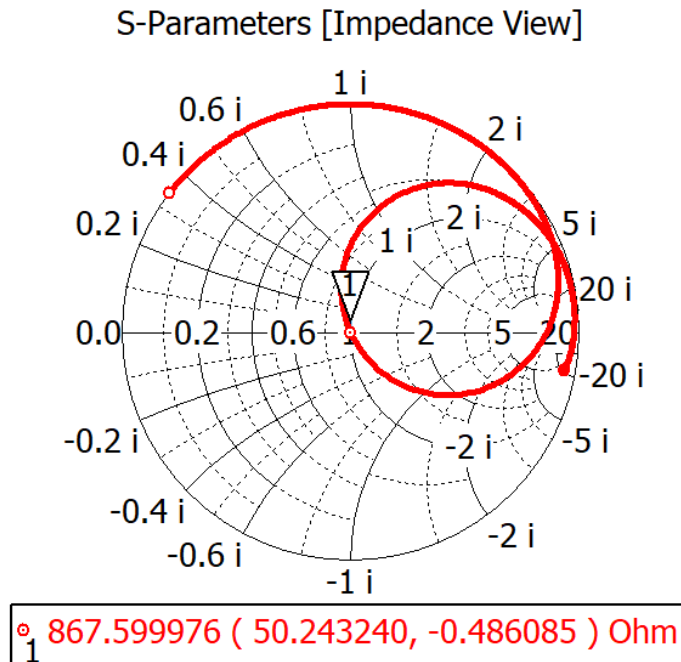


Figure 4.35: Optimized inverted-F antenna

The geometry in Figure 4.27 shows the added short circuit stub to the bent inverted-L antenna's geometry. This will compensate the capacitive element as shown by the simulations:



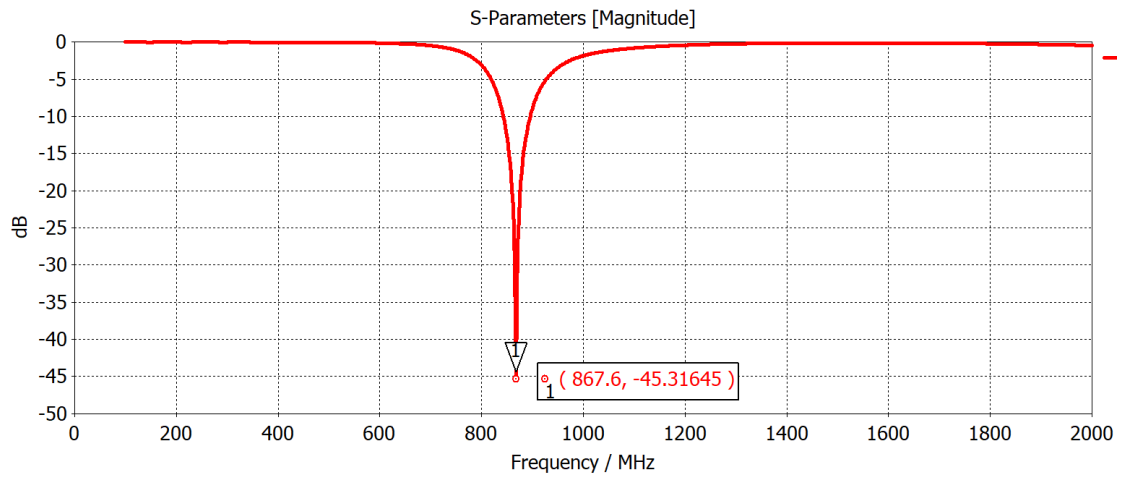
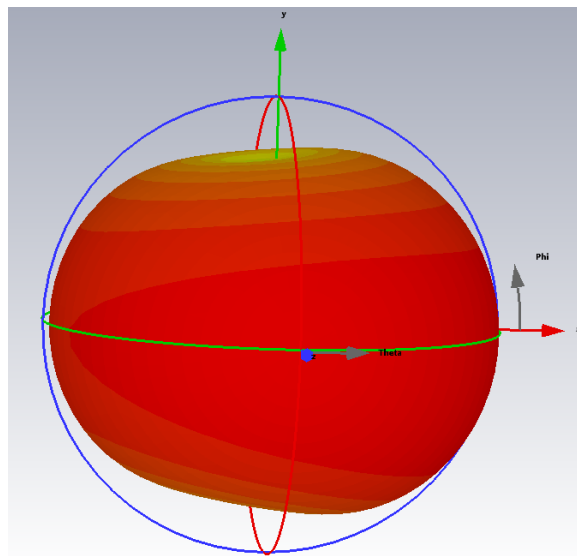


Figure 4.36: Simulation results a) Smith chart, b) S_{11}

Figure 4.36 shows that the antenna was correctly optimized, with a resonant frequency of 867.6 MHz. At this frequency the complex impedance, given by the Smith chart is of $50.24, -0.49 \Omega$, which confirms the optimization was carried out successfully. Figure 4.37 shows the radiation pattern of the inverted-F antenna.



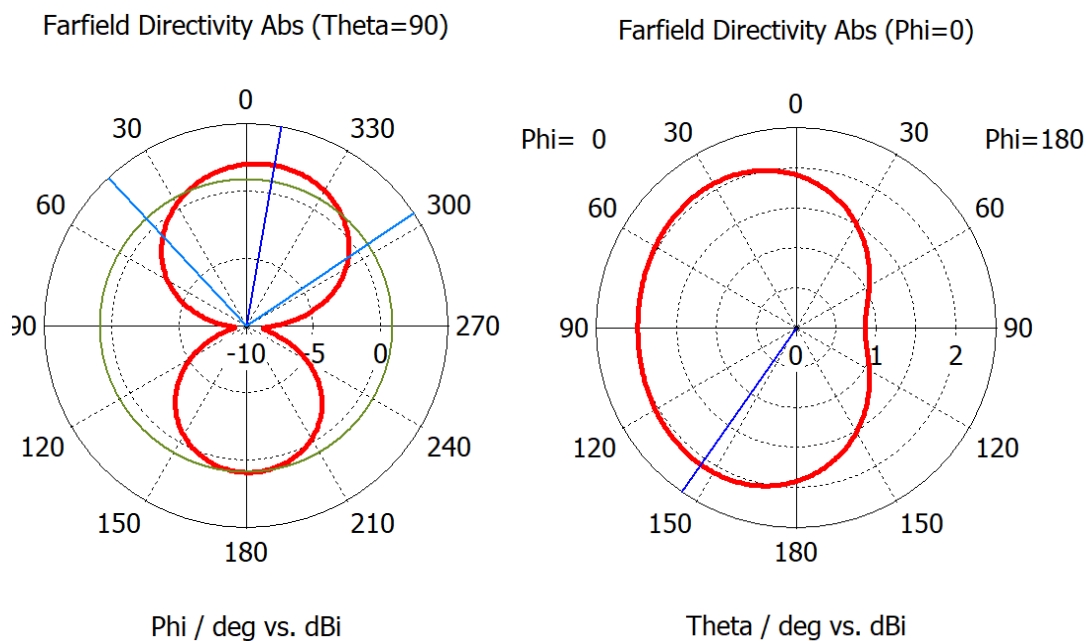


Figure 4.37: Simulated radiation pattern a) 3D radiation pattern. b) 2D cut - XY plane c) 2D cut - YZ plane

We can see that the radiation pattern is quasi-omnidirectional, but as shown in the XY plane cut, the antenna has some more directivity towards the side where there is no short circuit stub. However, for our use-case, this antenna's radiation pattern is sufficient.

Chapter 5

Validation of Designed PCB Antennas

In this chapter, some of the proposed geometries simulated in chapter 4 will be fabricated and tested in an anechoic chamber to validate the simulations and their implementation potential. The validation process for each antenna will be comprised of three stages:

1. **Design of the mock PCB:** A *mock* PCB is a printed circuit fabricated to test the antenna exclusively. This type of PCBs will contain the antenna's geometry with no other components, in a board with similar geometry to the prototype's final measurement, and a feeding mechanism for the antenna. Since our tests will be carried out in an anechoic chamber where the signal source has a 50Ω coaxial with a male SMA connector, the boards will have a female SMA connector to feed the antenna. For these PCBs the geometry previously designed in CST studio will be exported as a .DXF file and imported into Altium designer, a PCB and Schematic CAD program, where the mock PCBs will be designed.
2. **Fabrication and assembly of the mock PCB:** After designing the PCBs in Altium designer, their Gerber data will be exported and sent to fabrication house Eurocircuits for production. After receiving them, the PCBs by the soldering of the female SMA connectors, making it ready for testing.
3. **Test of the mock PCB:** The tests will be carried out in the Politecnico di Torino's anechoic chamber, a structure that allows to measure the radiation characteristics of radiating structures with no interference from other radio wave sources or self-interference from reflections of the radiated wave. This anechoic chamber has a NETWORK ANALYZER to measure the S-parameters of the antenna and a RECEIVER to measure the radiation strength of the

antenna. To measure the radiation pattern, the antennas will be placed inside the anechoic chamber, fixed to a rotating arm, which will make the antenna rotate around one of the polar axes, and the receiver will measure the radiation strength as it rotates every 2° . The characteristics to be measured in this test are the S_{11} parameter of the antenna to see the resonant frequency of the real structure and the quality of its impedance matching, as well as the $\phi = 0$, $\phi = 90$, and $\theta = 90$ cuts of the radiation pattern. The S_{11} parameter will be measured for each antenna from 500 MHz to 1,500 MHz to visualize the target frequency of 868 MHz. The radiation pattern will be measured at 837, 843, 849, 855, 861, 867, 873, 879, 885, 891, and 897 MHz for each antenna.

4. **Result analysis:** The test results will be analyzed and compared to the simulated behavior of the structures. To extract the data from the files generated by the anechoic chamber's receiver and be able to present and analyze the results, Matlab will be used to generate the graphs of the radiation pattern cuts. This data will then be interpolated in Matlab to generate an approximate of the 3D radiation pattern. The S_{11} parameter will be visualized using Touchstone Viewer, a program that allows the visualization of .S1P files.

The antenna topologies that will be tested are:

- Dipole antenna with Balun
- Monopole antenna
- Inverted-L antenna
- Inverted-F antenna

After analyzing these previously simulated antennas, a PCB with a chip antenna will also be manufactured and tested as an alternative to planar antennas. The analysis of the radiation and geometric characteristics of all these topologies will allow us to choose the most appropriate antenna to be used in the design of the sensor node PCB.

5.1 Planar dipole antenna

The first PCB to be designed was the planar dipole antenna with the integrated Balun. The geometry was exported from CST Studio and the following PCB was designed in Altium Designer.

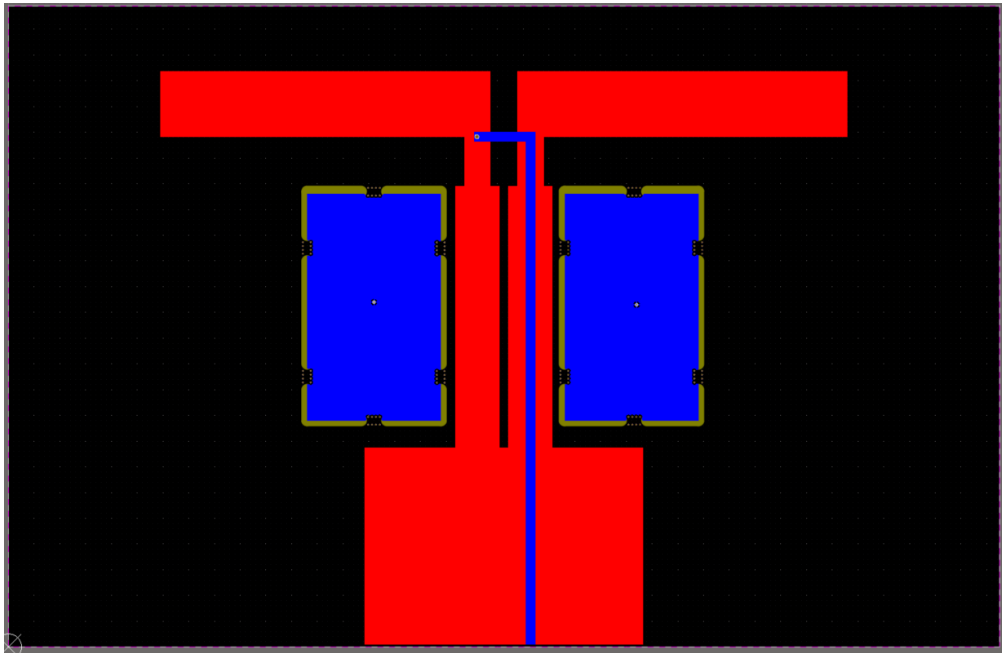


Figure 5.1: PCB Design: Dipole Antenna with Balun

Note that the blue rectangles to the sides of the feed line correspond to elements with copper planes that can be popped out of the board. This was built into the design due to fabrication constraints from Eurocircuits that required a higher copper density in the PCB to ensure the accuracy of the copper dimensions. Due to the bottom (Blue) layer of the PCB having only the slim feed line, the copper density was very low. By adding these two rectangles, the copper density in the bottom layer of the board was enough to satisfy the requirement. Before testing these two structures will be removed from the PCB so it will not affect its radiative properties.

Since it has the biggest dimension of all the designed antennas (The mock PCB containing just the antenna and Balun are bigger than the current generation sensor node), it does not accomplish the design goals for the sensor node PCB and will not be chosen to be integrated in its design. Due to this, this antenna was the only one to be designed without soldermask. The reasoning behind this decision was to validate the results of the simulations without influence of the soldermask, even though our hypothesis was that, being such a thin layer, the solder mask would not change the properties of the structure. In this way, if this antenna managed to be faithful to the simulations and the other ones didn't, we would know that the soldermask had a bigger effect on the radiative properties than anticipated and all structures should be simulated with soldermask.

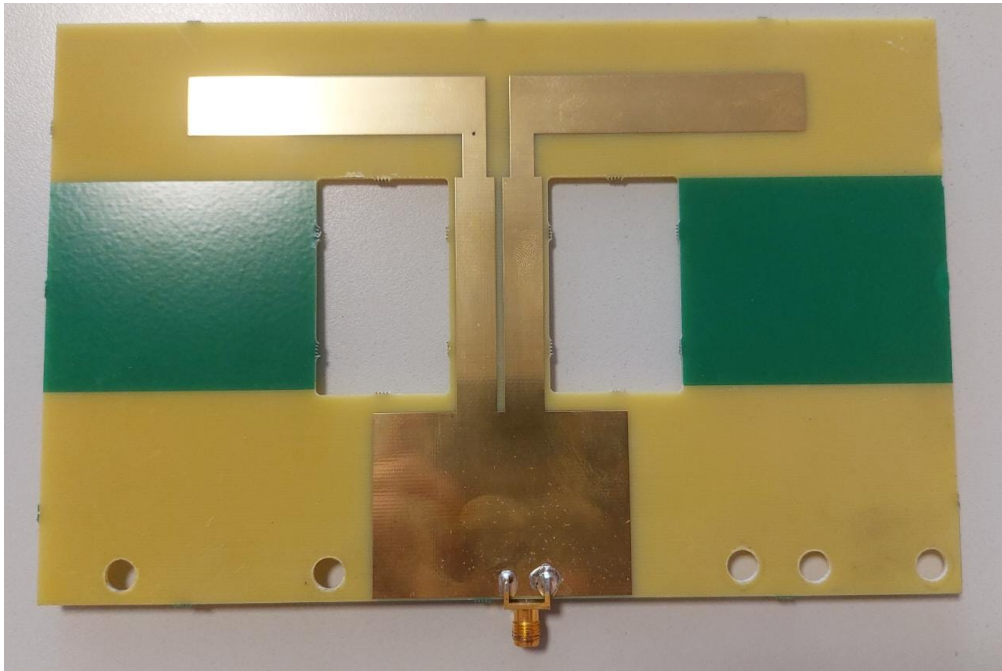


Figure 5.2: PCB Design: Dipole Antenna with Balun

Figure 5.2 shows the dipole antenna with integrated Balun after fabrication, removal of the pop-out structures, and assembly of the connector. Note that mounting holes for the anechoic chamber's rotating arm were drilled in the substrate of the PCB. After an initial visual inspection of the assembled PCB, the tests in the anechoic chamber were carried out.

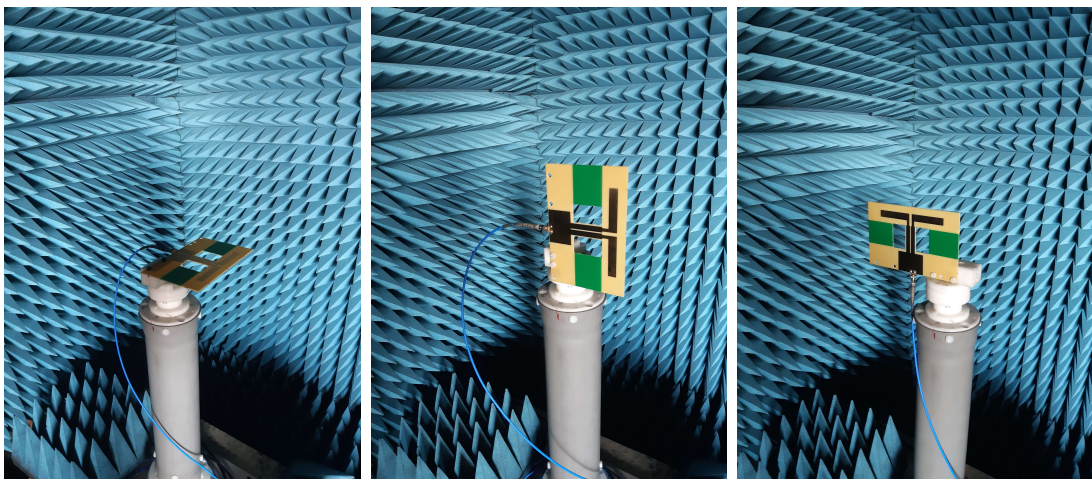


Figure 5.3: Test setup: a) $\phi = 0$, b) $\phi = 90$, and c) $\theta = 90$

The setup for the tests was fixing the PCB in the $\phi = 0$, $\phi = 90$, and $\theta = 90$ planes as shown in Figure 5.3 and rotating around that axis, measuring the strength every 2° . The network analyzer feeding the antenna will also provide a measurement of the S_{11} parameter as shown in Figure 5.4. The radiation pattern results were then analyzed using the Matlab code in Appendix A to generate the 2D cuts of the radiation patterns, shown in Figure 5.7, and a 3D visualization from interpolating the data of these cuts, shown in Figure 5.7. Note that only the polar representation of the radiation pattern cuts will be shown in this chapter. For the Cartesian representation refer to Appendix B.

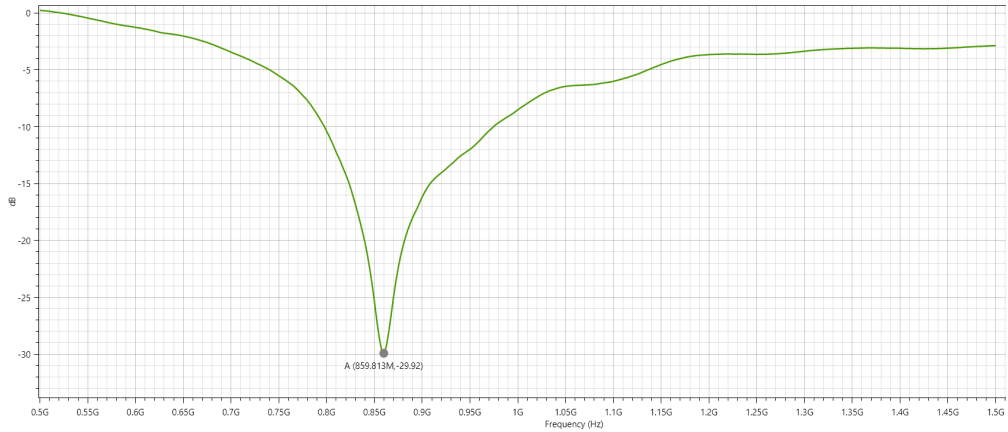


Figure 5.4: Test results: S_{11}

The first thing to be validated was the antenna’s resonant frequency and impedance matching to the 50Ω connector feeding it. This is done through the analysis of the S_{11} parameter, shown in Figure 5.4. By the global minimum point we can know that the resonant frequency of this antenna is 859.8 MHz. However, this antenna was simulated to be resonant at exactly 868 MHz. However, according to the results presented for the other antennas, we don’t think this behavior is an inaccuracy of the simulation but due to external factors in the testing process.

Our hypothesis as to why the antenna’s resonant frequency shifted from the simulation is that it is caused by the cutouts designed to increase copper density. To prove this, the antenna was simulated again in CST studio but with the cutouts added. Figure 5.5 shows that the frequency shifts to 870 MHz. However, it doesn’t seem that the holes provide the complete -20 MHz shift. A possible cause of this is that the rotating arm of the anechoic chamber is interfering with the antenna since as it was mounted it does not sit in the dipole’s axis. This causes the arm and cable to be in the radiation volume of the antenna and compound to the effect of the cutouts in shifting the antenna’s frequency down.

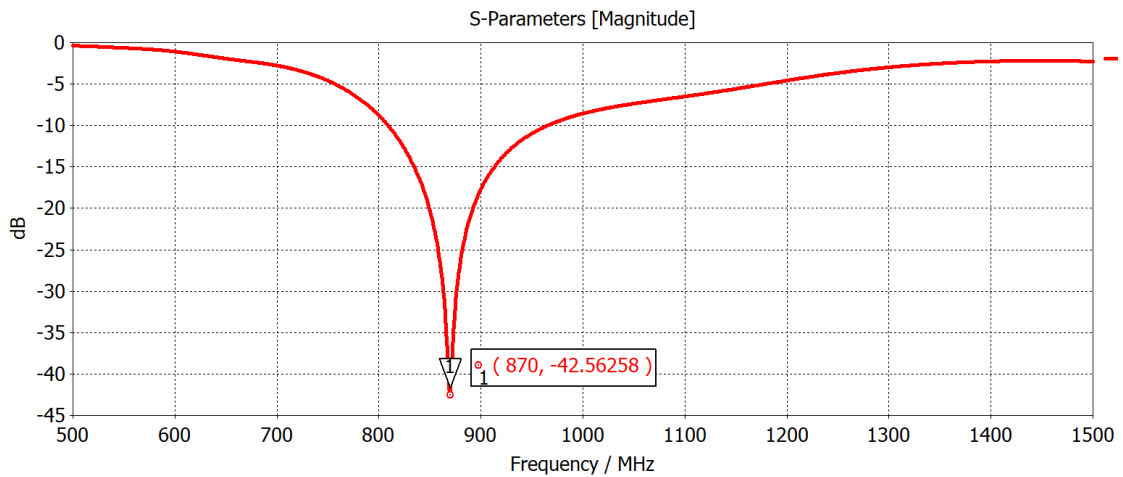


Figure 5.5: Simulation results: S_{11}

What we can conclude from Figure 5.4, that the antenna is well matched at a resonant frequency with a S_{11} parameter of -29.92 dB. The radiation patterns were generated with the 861 MHz dataset, the closest frequency to the measured resonant frequency. As we can see by the 2D cuts in Figure 5.7, the radiation pattern describes an omnidirectional antenna, which matches the simulations done in CST Studio. This validates the results obtained in the simulations.

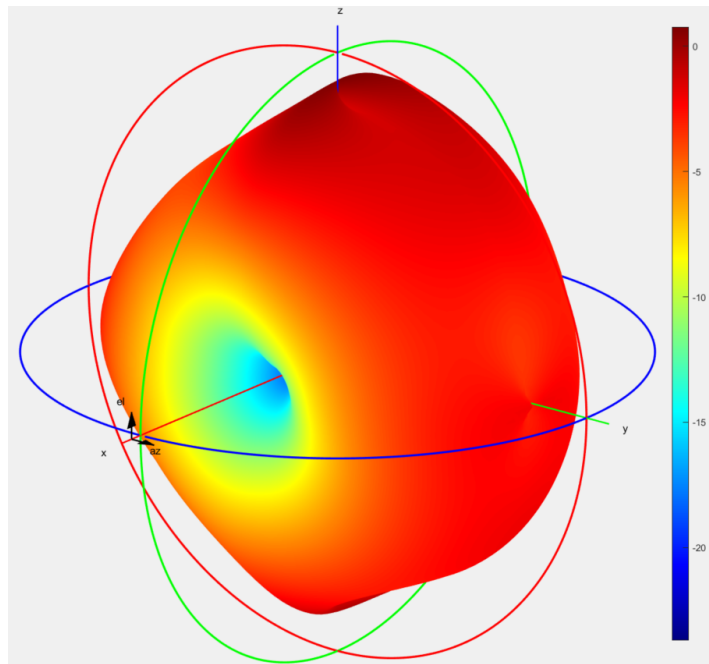


Figure 5.6: Approximate 3D radiation pattern

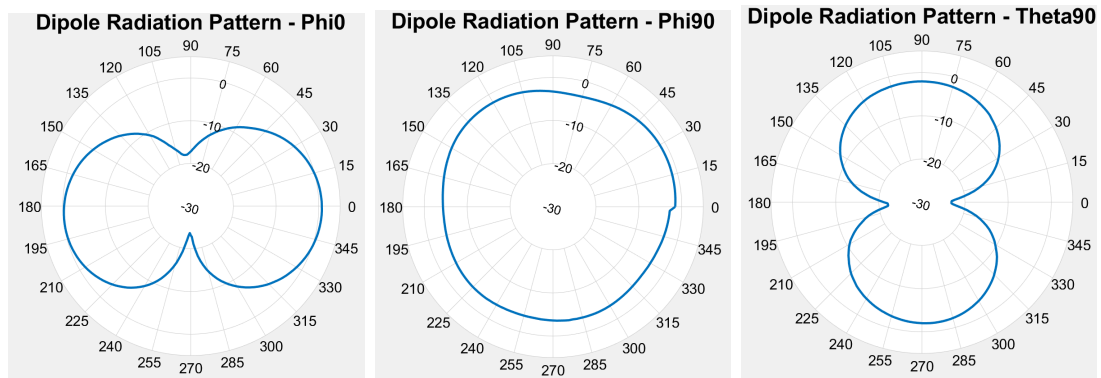


Figure 5.7: Radiation pattern cuts: a) $\phi = 0$, b) $\phi = 90$, and c) $\theta = 90$

5.2 Planar monopole antenna

The next PCB to be designed was the planar monopole antenna. The geometry was exported from CST Studio and the following PCB was designed.

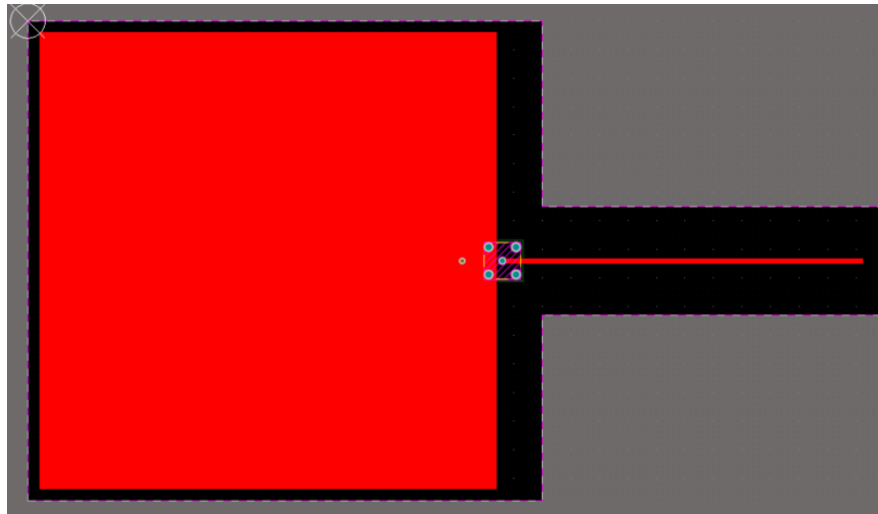


Figure 5.8: PCB Design: Monopole Antenna

Note in Figure 5.8 that cutouts were designed on the sides of the monopole's length. As with the dipole, the thin antenna arm would have a very low copper density. To increase the copper density, some of the substrate without the ground plane was removed around the antenna's arm.

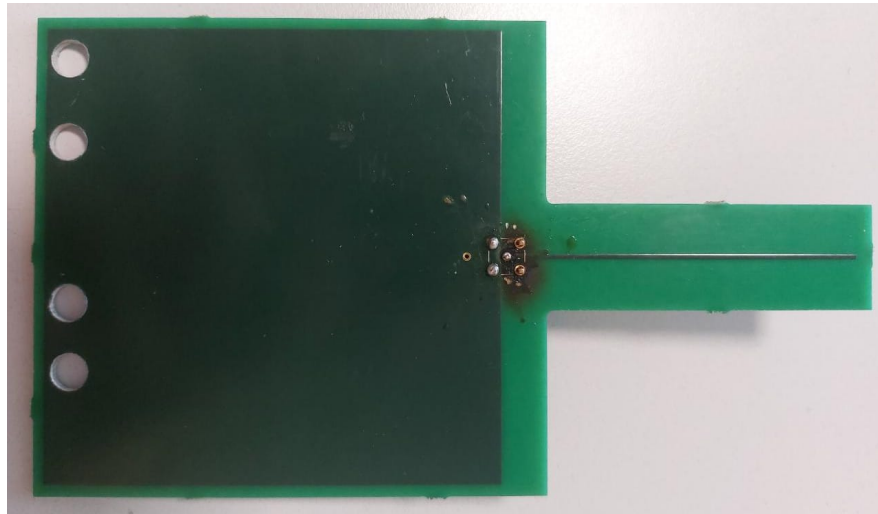


Figure 5.9: PCB Design: Monopole Antenna

Figure 5.9 shows the monopole antenna after fabrication and assembly of the connector and drilling of the mounting holes. After an initial visual inspection of the assembled PCB, the tests in the anechoic chamber were carried out in the same manner as the previous antenna.

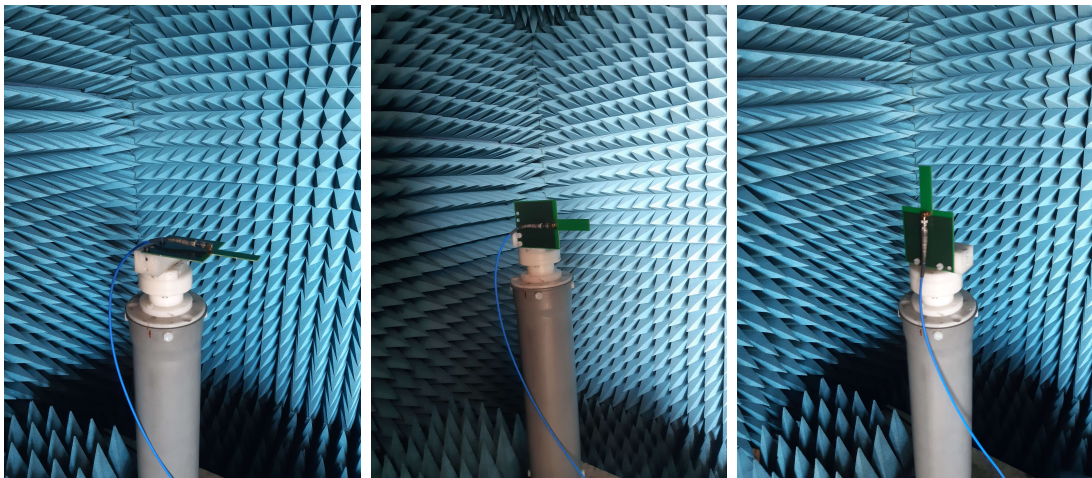


Figure 5.10: Test setup: a) $\phi = 0$, b) $\phi = 90$, and c) $\theta = 90$

Analysing the results of the S_{11} parameter measurement, we can immediately realize that the antenna does not have a good performance. This, however, was expected, as in the simulation results in Figure 4.19 we could foresee that the antenna would have matching problems due to its high input impedance.

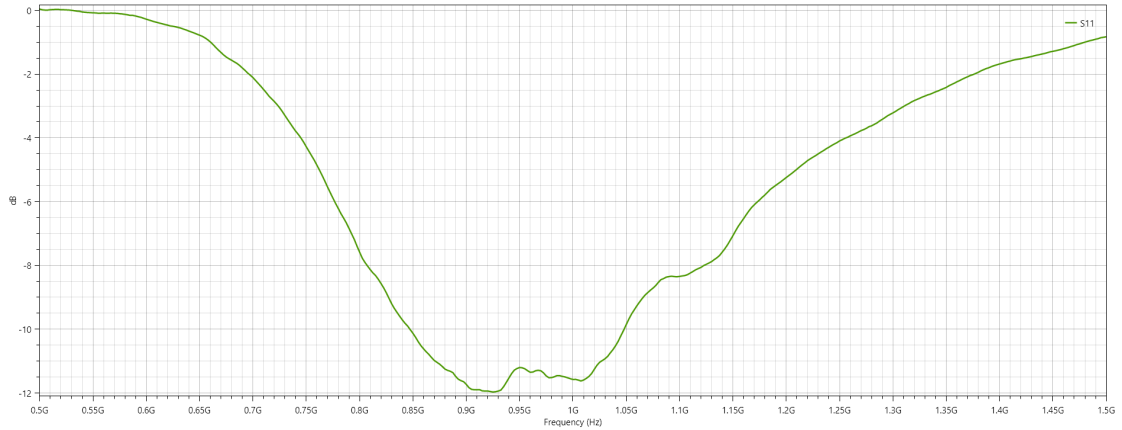


Figure 5.11: Test results: S_{11}

A disadvantage of the planar monopole antenna’s design is that it is very difficult to tune its input impedance. As shown in the design of the inverted-L antenna, the ground plane angle can be modified to increase input impedance, but to decrease input impedance there is no easy way planarly. A solution for this, if this is the design chosen to be used in the sensor node PCB is to include a pi matching network, a net of inductive and capacitive components that allows the matching of two structures with different impedance. With this in mind we can still see that the radiation pattern of the planar monopole is still fairly omnidirectional at 868 MHz. Also, we can see a pattern will start to develop with these measurements that the northern hemisphere of the $\phi = 0$ and $\phi = 90$ measurements are distorted with respect to the southern hemisphere. This hemisphere represents the side of the board where the connector was placed. The interference of the connector and cable affect the measurements of this hemisphere in the measurements that have the connector so close to the antenna.

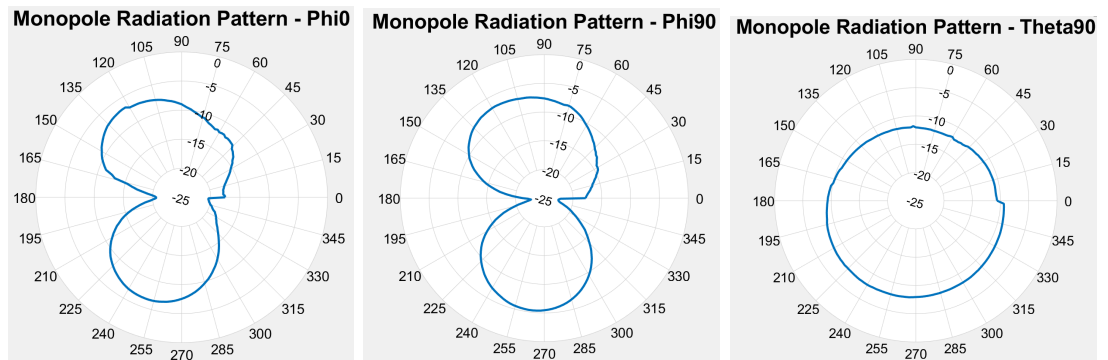


Figure 5.12: Radiation pattern cuts: a) $\phi = 0$, b) $\phi = 90$, and c) $\theta = 90$

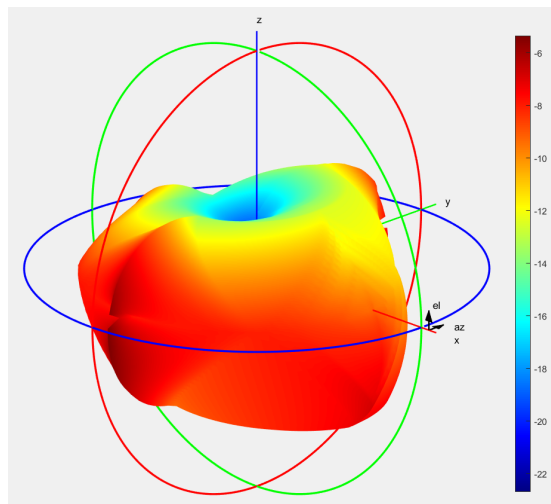


Figure 5.13: Approximate 3D radiation pattern

5.3 Planar inverted-L antenna

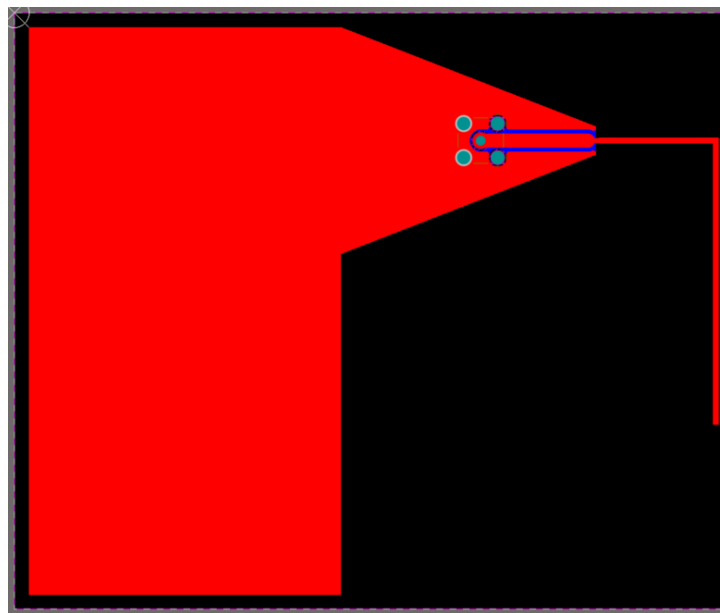


Figure 5.14: PCB Design: Inverted-L Antenna

Next, the planar inverted-L antenna was designed. The geometry was exported from CST Studio and the PCB was designed in Altium Designer as shown in Figure 5.14. Note that in this design, the connector was moved away from the

antenna through the use of a co-planar waveguide that was designed for a $50\ \Omega$ input impedance. The antenna was then manufactured, assembled, and prepared for testing as shown in Figure 5.15.

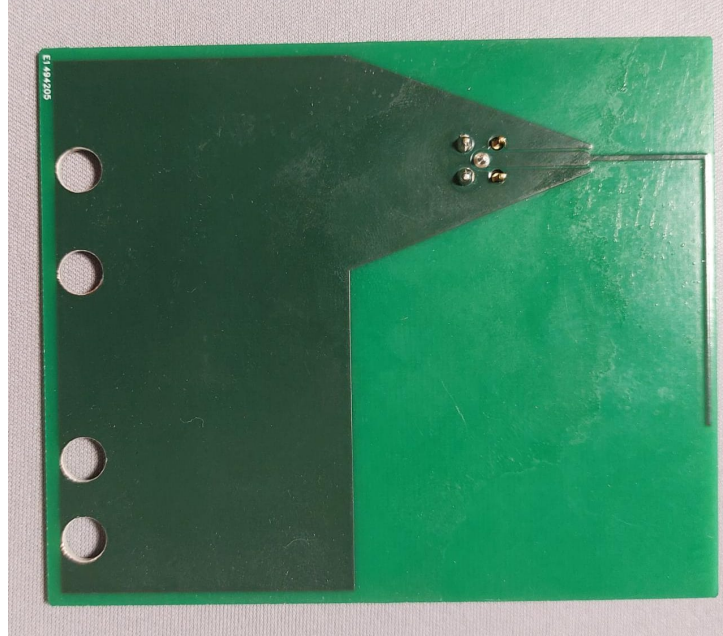


Figure 5.15: PCB Design: Inverted-L Antenna

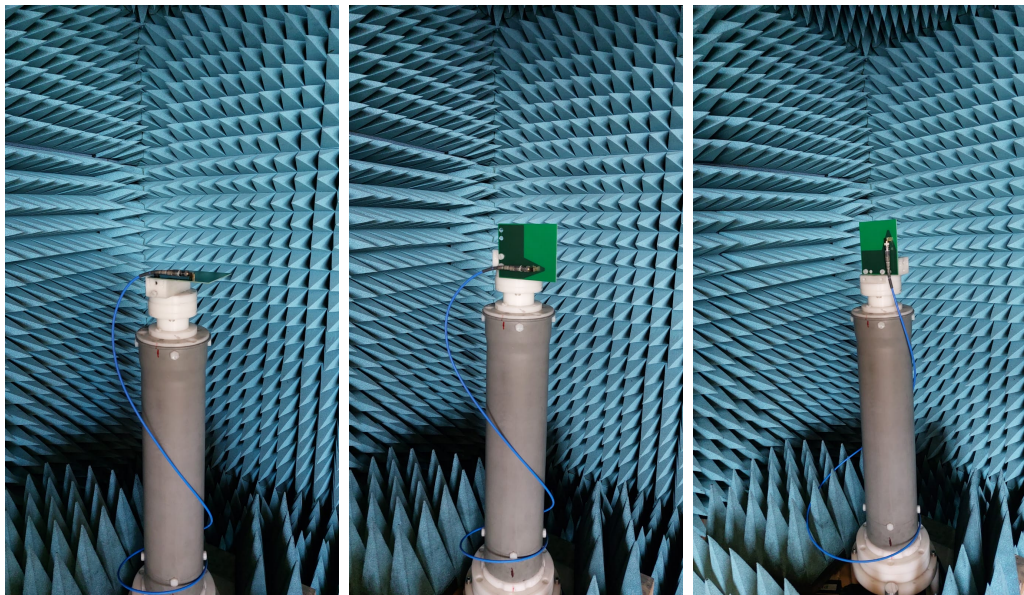


Figure 5.16: Test setup: a) $\phi = 0$, b) $\phi = 90$, and c) $\theta = 90$

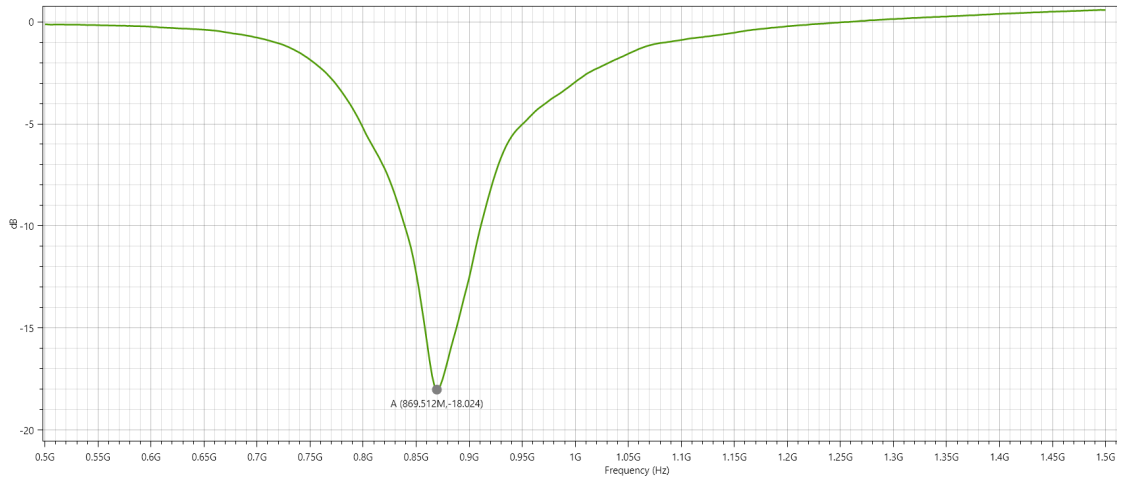


Figure 5.17: Test results: S_{11}

Figure 5.17 show that the antenna shifted its resonant frequency by 1.5 % with a value of 852.5 MHz, compared with the 865.7 MHz of the simulation in Figure 4.28. The S_{11} minimum value of -11.97 dB shows that the antenna was also mismatched when compared to the simulations. The hypothesized cause for this behavior is the interaction between the co-planar waveguide and the angled ground plane. On the thinnest part of the ground plane the behavior of the co-planar waveguide changes, starting to radiate. This changes the input impedance and lengthens the antenna, decreasing the resonant frequency. Other than this, the tests validated the results of the simulations.

The conclusion for the Inverted-L antenna is that, due to the angled plane it would be difficult to implement in the sensor node PCB design due to the increased footprint, that reduces available component space as well as the feeding complexities regarding the interaction of the co-planar waveguide with the angled ground plane.

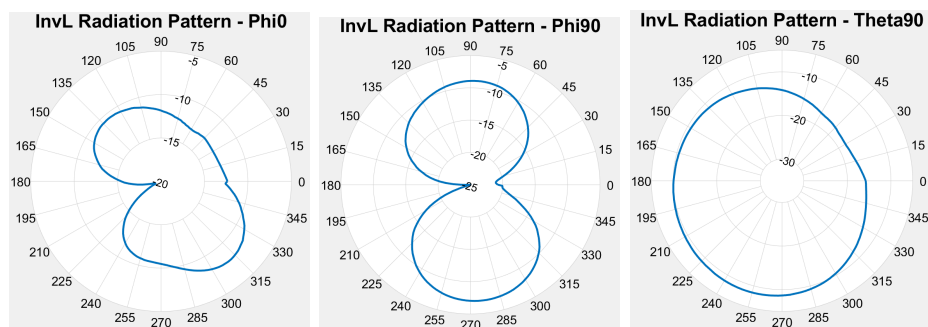


Figure 5.18: Radiation pattern cuts: a) $\phi = 0$, b) $\phi = 90$, and c) $\theta = 90$

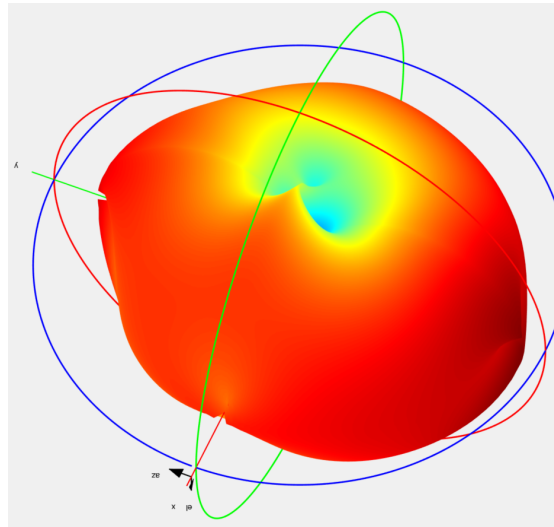


Figure 5.19: Approximate 3D radiation pattern

5.4 Planar inverted-F antenna

Continuing the design of the PCBs, the planar inverted-F antenna was designed. The geometry was exported from CST Studio and the PCB was designed in Altium Designer as shown in Figure 5.20. The antenna was then manufactured, assembled, and prepared for testing as shown in Figure 5.21.

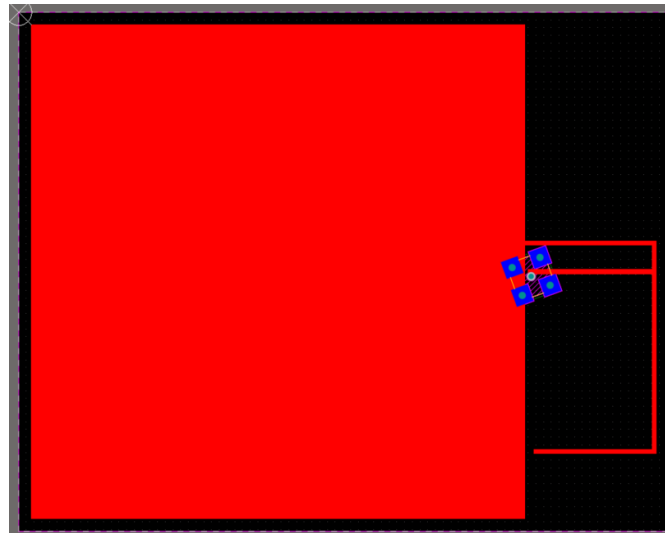


Figure 5.20: PCB Design: Inverted-F Antenna

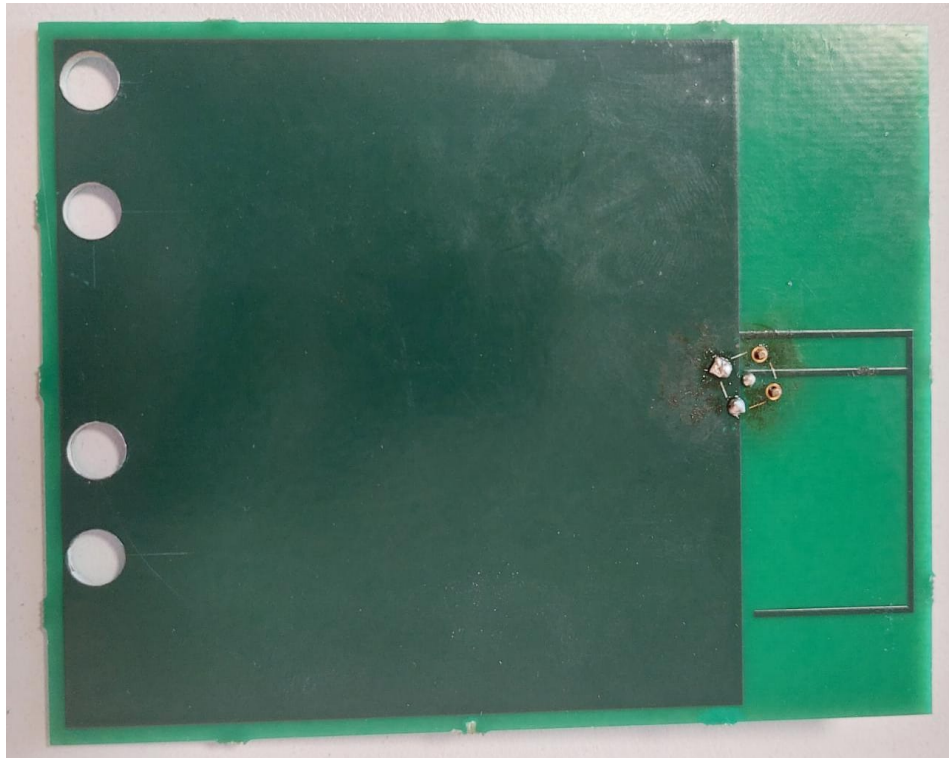


Figure 5.21: PCB Design: Inverted-F Antenna

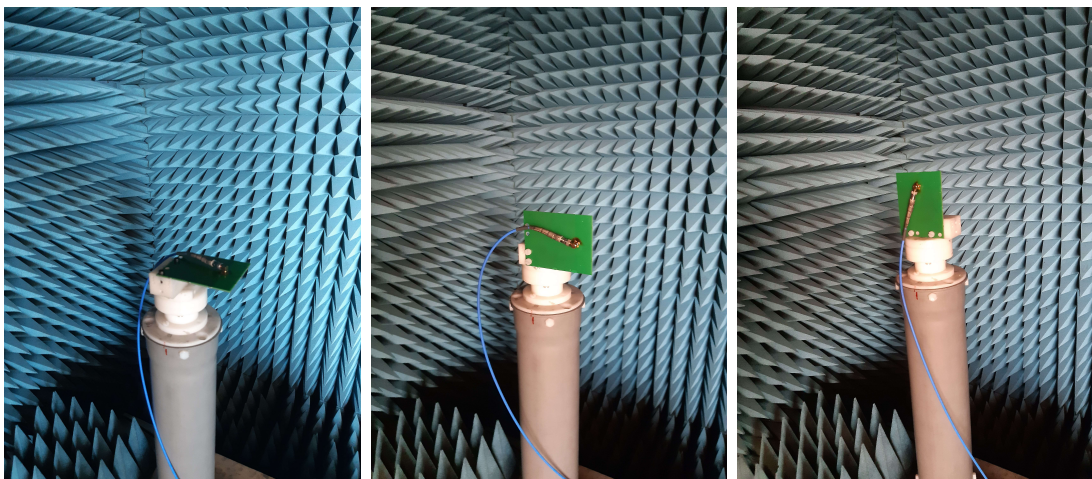


Figure 5.22: Test setup: a) $\phi = 0$, b) $\phi = 90$, and c) $\theta = 90$

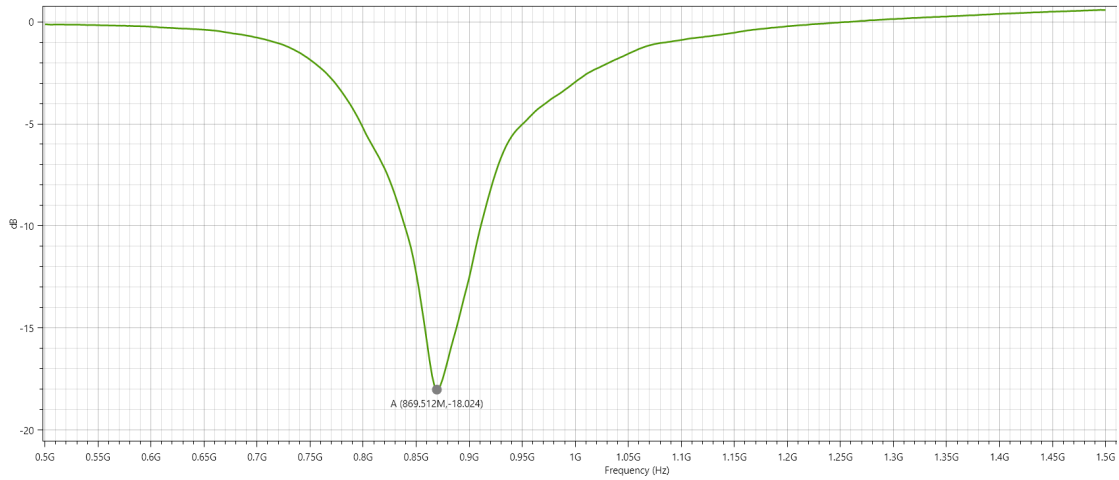


Figure 5.23: Test results: S_{11}

Figure 5.23 show that the antenna carried over its radiative properties from the simulation, with a resonant frequency of 869.512 MHz, compared with the 867.6 MHz of the simulation in Figure 4.36. Also good matching can be noted with -18 dB, which, for a real antenna, is good. However, a pi-shaped matching network could still be used in the PCB to match it even better. The radiation pattern cuts shown in Figure 5.24, as with the monopole antenna, is deformed in the hemisphere with the connector due to its vicinity with the antenna. The hemisphere opposite of the connector and the $\theta = 90$ cut of the radiation pattern demonstrate that the antenna radiates omnidirectionally.

The conclusion from the test results of the inverted-F antenna is that it validates the design and is a very trustworthy topology since it keeps its resonant frequency equal to that of the simulations, and can be easily corrected through a pi-shaped matching network in the case of implementation on the sensor node PCB.

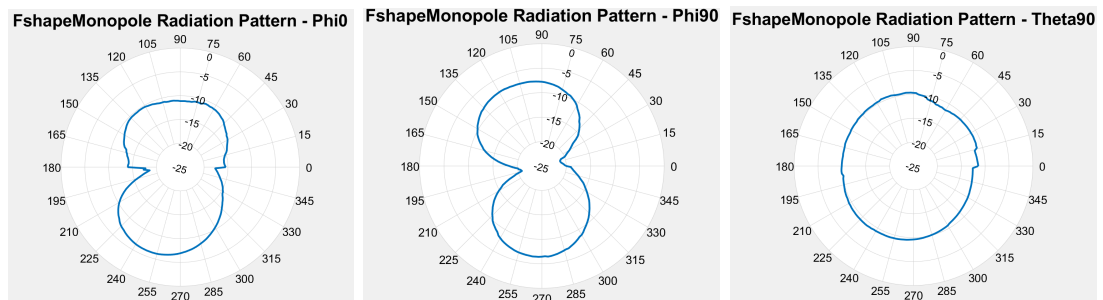


Figure 5.24: Radiation pattern cuts: a) $\phi = 0$, b) $\phi = 90$, and c) $\theta = 90$

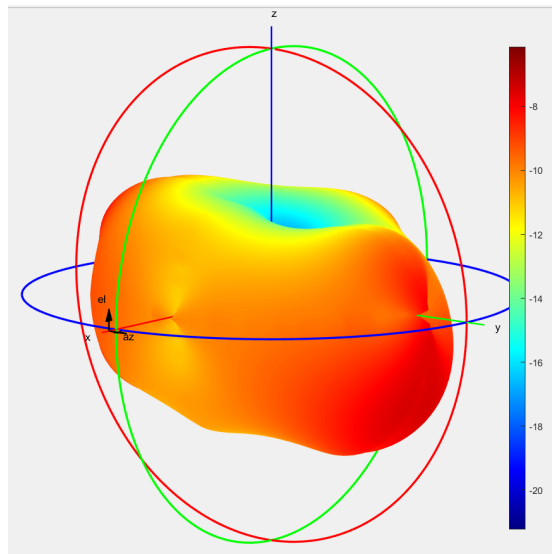


Figure 5.25: Approximate 3D radiation pattern

5.5 PCB Chip antenna

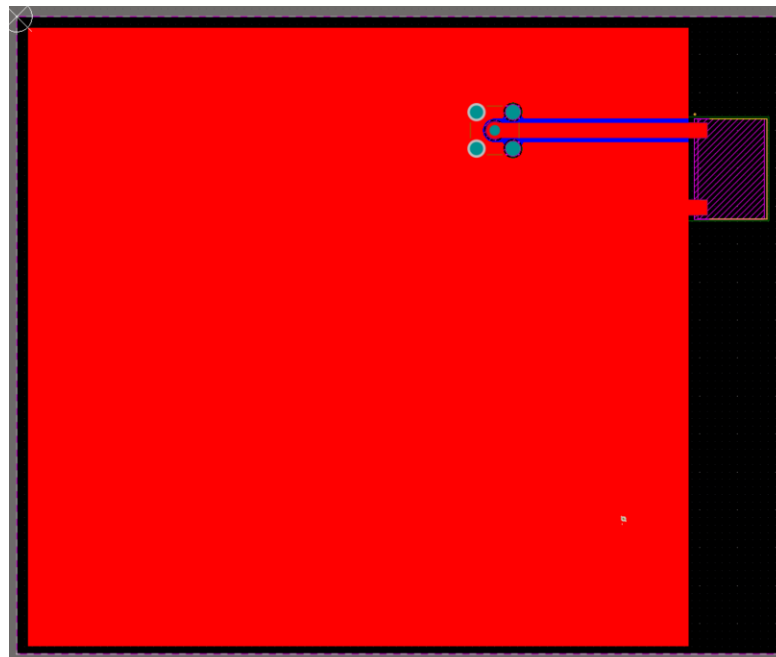


Figure 5.26: PCB Design: Chip Antenna

The mock PCB in Figure 5.26 was designed in order to test the performance of a commercially produced chip antenna and compare it to the printed planar antennas. In this case, the Linx ANT-868-uSP410 was chosen, a 868 MHz surface mount monopole antenna for embedded applications, specifically advertised for use in LoRaWAN® and SigFox® applications. The datasheet specifies an operating band with $VSWR \leq 2 : 1$ from 862 MHz to 876 MHz, and a footprint with 13.2x9.1x2.9 mm dimensions; the most compact among all the tested antennas[31].



Figure 5.27: PCB Design: Chip Antenna

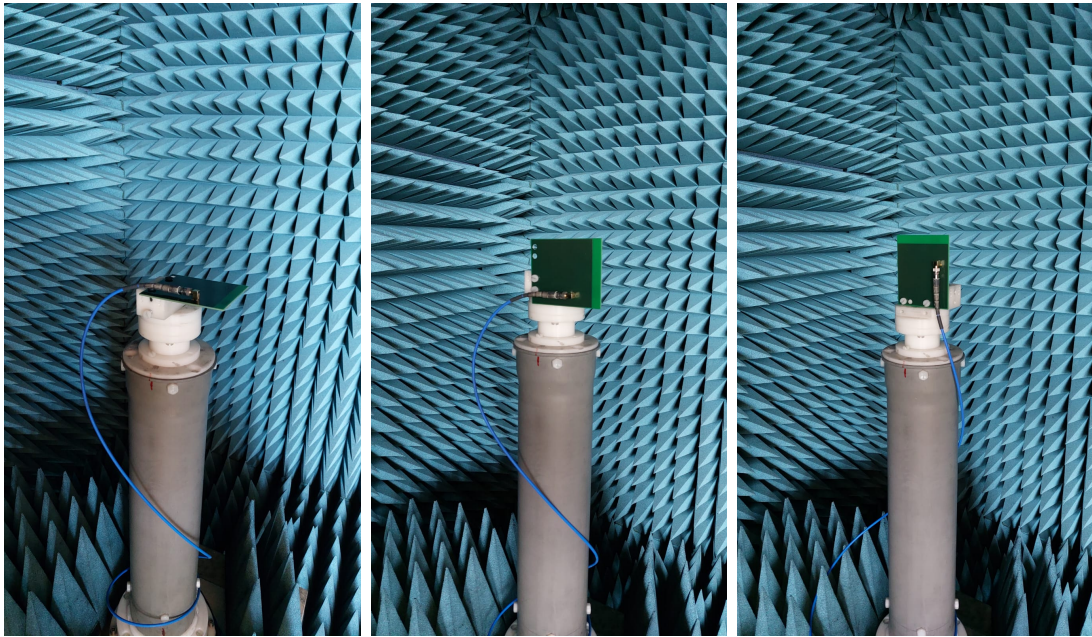


Figure 5.28: Test setup: a) $\phi = 0$, b) $\phi = 90$, and c) $\theta = 90$

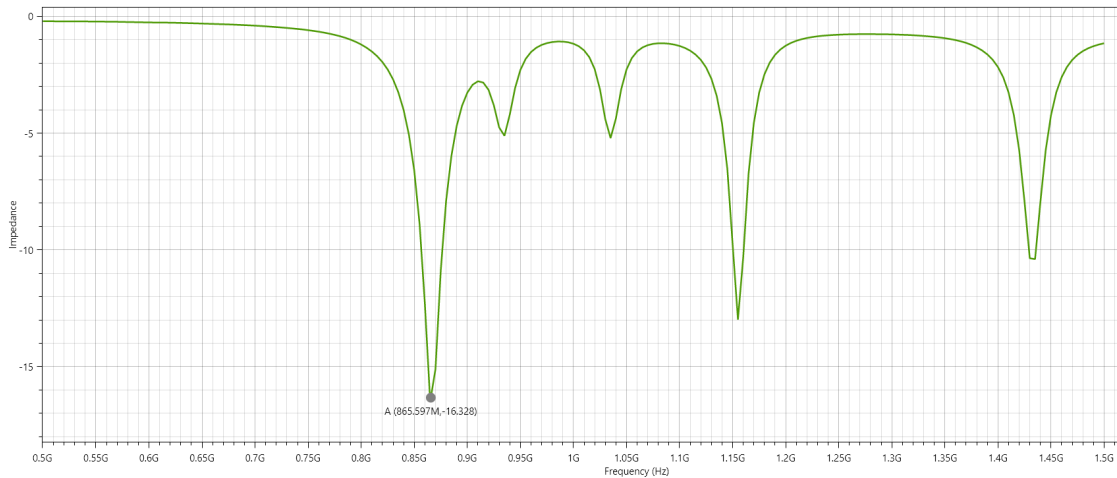


Figure 5.29: Test results: S_{11}

Figure 5.29 validates the characteristics from the datasheet. The approximate $VSWR \leq 2 : 1$ band, given by 10% returned power or -10 dB S_{11} is from 856 MHz to 876 MHz. However, we can also see that the antenna has two other -10 dB bands at 1.15 GHz to 1.16 GHz, and 1.42 GHz to 1.43 GHz. The radiation pattern in Figure 5.30 also validates the omnidirectional radiation of the antenna as presented in the datasheet.

The conclusion from the test results of the chip antenna is that, even though they are much easier to implement into any design, their performance and radiation characteristics do not exceed the performance of a well designed antenna.

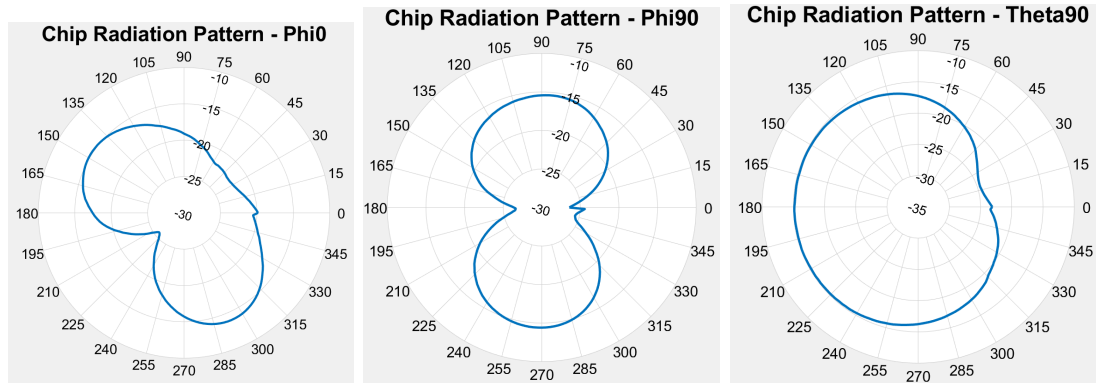


Figure 5.30: Radiation pattern cuts: a) $\phi = 0$, b) $\phi = 90$, and c) $\theta = 90$

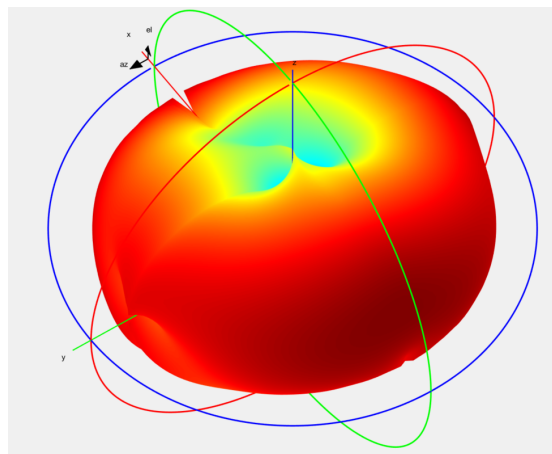


Figure 5.31: Approximate 3D radiation pattern

5.6 Choosing the antenna topology for the sensor node PCB

Once all the designs have been tested and analyzed, the antenna's topology to be used in the sensor node PCB was chosen. The most important aspects that were taken into account for this decision were:

- **Performance:** Since the antenna will be used for LoRa communications, it has to show sufficient radiation power for the application. Another important performance aspect is how similar the antenna performance in the tests was to the simulations, as an antenna that had results similar to the simulation is more reliable and resilient to external aspects to be implemented than one that varied from the simulation results.
- **Dimensions:** Due to its integration in the sensor node PCB, it should not increase the dimensions of PCB by too much with respect to the current generation of the sensor node PCB. This would mean increased costs since a bigger PCB would cost more to fabricate, and a bigger enclosure would be needed which would also drive up the cost of the unit.
- **Ease of integration:** The antenna should avoid forcing as many constraints as possible on the PCB design. As an IoT node, the sensor node PCB antenna will already be a very densely populated PCB so reducing the available area for component placing and routing would make the design very difficult.

The easiest way to arrive to the final antenna topology is to rule out the designs that perform poorly in one or more of these categories. The most obvious topologies to be ruled out are the monopole and dipole antennas. The dipole has the best radiation power out of all the tested topologies but its size makes it impossible to be integrated due to the need of a Balun. The monopole, on the other hand, had the worst performance out of all the antennas due to the difficulty in tuning its characteristic impedance. Its resonance band was also the largest among all antennas, not having a defined resonance frequency.

The other topologies are well matched in the performance category, but the inverted-L antenna needs more space out of the three remaining antennas. Needing the angled ground plane increases the overall footprint of the antenna and reduces the available space for PCB components. Due to this it was also ruled out. Finally, the chip antenna was also ruled out due to the cost increase it means for the BOM of each sensor node PCB. Even if it is the most compact design that is the easiest to integrate, its cost increase is a downside that the inverted-F antenna does not have.

In conclusion, the inverted-F antenna will be the topology chosen to be integrated in the design of the sensor node PCB. Its combination of possessing a compact size, ease of integration and performance bring the perfect balance for our specific use-case scenario. The only constraints placed on the PCB design is the inclusion of the footprints for a pi matching network in the case the impedance matching has to be improved, and leaving a 23 mm gap from the board edge with the antenna and the ground plane. The reduction of component space is minimal and allows the board to be designed easily.

Chapter 6

Mechanical Design of the sensor node enclosure

Having chosen the inverted-F antenna as the antenna to be integrated in the design, we could use its dimensions to calculate the average size of the PCB to choose a proper enclosure and connection interface. As mentioned in section 1.5, the requirements of the mechanical design are to ensure the protection of the sensor node’s electronic components by maintaining a weatherproof seal, decrease the assembly complexity, and increase the modularity of the sensor node.

To accomplish these objectives the following connection interface is proposed:

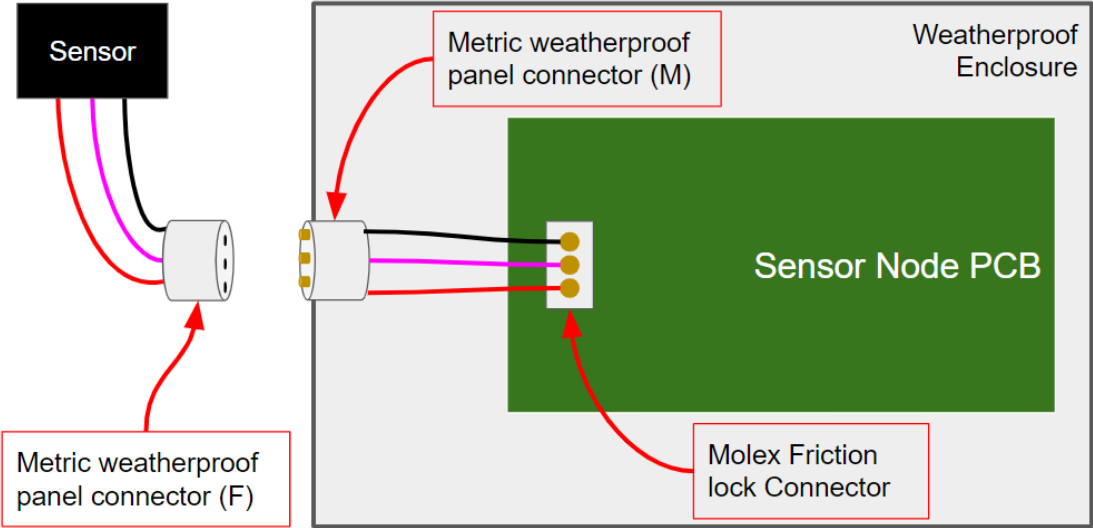


Figure 6.1: Proposed connection interface

In the connection interface shown in Figure 6.1, the sensor is connected to the female part of a metric weatherproof panel connectors. These type of connectors, as shown in Figure 6.2, are soldered to the exposed conductors of a cable. Then the weatherproof cap is secured around the insulator of the cable and the female connector is connected to the male connector, mounted on the edge of the waterproof enclosure. Then a sealing structure in the female section is screwed by hand into the male section to secure the connection and ensure the waterproof seal of the connector.

The use of this type of connector would accomplish all three requirements for the design of the connecting interface. It provides a waterproof seal, while increasing modularity since sensors can now be connected and disconnected from the sensor node without needing to open the enclosure or using any specialized tools. Also, the male part which remains attached to the enclosure includes a cap which can be placed on the connector when nothing is connected to it to keep it weatherproof, making it possible to leave the sensor node installed even when a sensor is removed. This also reduces the assembly complexity since sensor nodes and sensors can be assembled separately. Before, with the cable glands, the sensor was fixed to the sensor node and the whole system became cumbersome to assemble, test, transport, and install. In specific the AOHUA [32] (a Chinese company specialized in waterproof plugs) range of metric waterproof plugs connectors were proposed for this design since their cost is very low when bought in bulk (about 2.25 USD each when ordering less than 2000 units).



Figure 6.2: Female terminal mounting method of metric connector[33]

The next component in the mechanical interface is the weatherproof enclosure. As mentioned in section 2.3, a minimum IP rating of IP66 is needed for the enclosure, as well as being compatible with the AOHUA metric connectors with the least amount

of assembly complexity. To choose an appropriate enclosure the approximate size of the PCB was calculated by Knowing that the current version of the sensor node PCB has a dimension of 100x76 mm which indicates a required area of 7,600 mm² for the components, and the inverted-F antenna needs a 23 mm gap. As such, the minimum required area of the PCB is given by:

$$A_{min} = A_{comp} + (L_{ant} * W_{PCB}) \quad (6.1)$$

where A_{comp} is the minimum area needed for the components or 7,600 mm², L_{ant} the length of the antenna or 23 mm, and W_{PCB} the width of the PCB.

With these requirements in mind, the enclosure was chosen. The proposed enclosure is the Spelsberg TK PC 1309-6-tm, an IP66 polycarbonate enclosure with a transparent cover with dimensions 130x94x57 mm. It also includes 10 ports on the sides of the enclosure compatible with M16 and M20 metric connectors with knock out ports that are usually watertight, but can be opened with a screw driver or small cutting object to install the male side of the panel mounted metric connector. The TK PC 1309-6-tm enclosure is shown in Figure 6.3. The area inside of the enclosure is 10,912 mm² which leaves, by using Equation 6.1, an area of 8,888 mm² is left for the components. This size is greater than the minimum component area of 7,600 mm², and allows for a design of the PCB with relatively relaxed size constraints.



Figure 6.3: Spelsberg TK PC 1309-6-tm enclosure [34]

On the inside of the enclosure, the male part of the metric connector has concave terminals to which cables can be soldered easily as shown in Figure 6.4. These cables will connect to the board using Molex friction lock connectors. These connectors

use crimped pins inside a plastic housing which has mechanical locking mechanisms. This housing, or female terminal will connect and lock onto the male terminal which is soldered onto the PCB. This type of connection mechanism allows the PCB to be independent from the sensor and enclosure completely, making maintenance work easy. If a PCB needs to be changed, the damaged PCB would just need to be disconnected from the Molex connectors, the screws removed from the board, and the new board can be screwed in, and reconnect the Molex connectors. This operation would take very little time and effort, and the technician would only need a screwdriver to perform it.

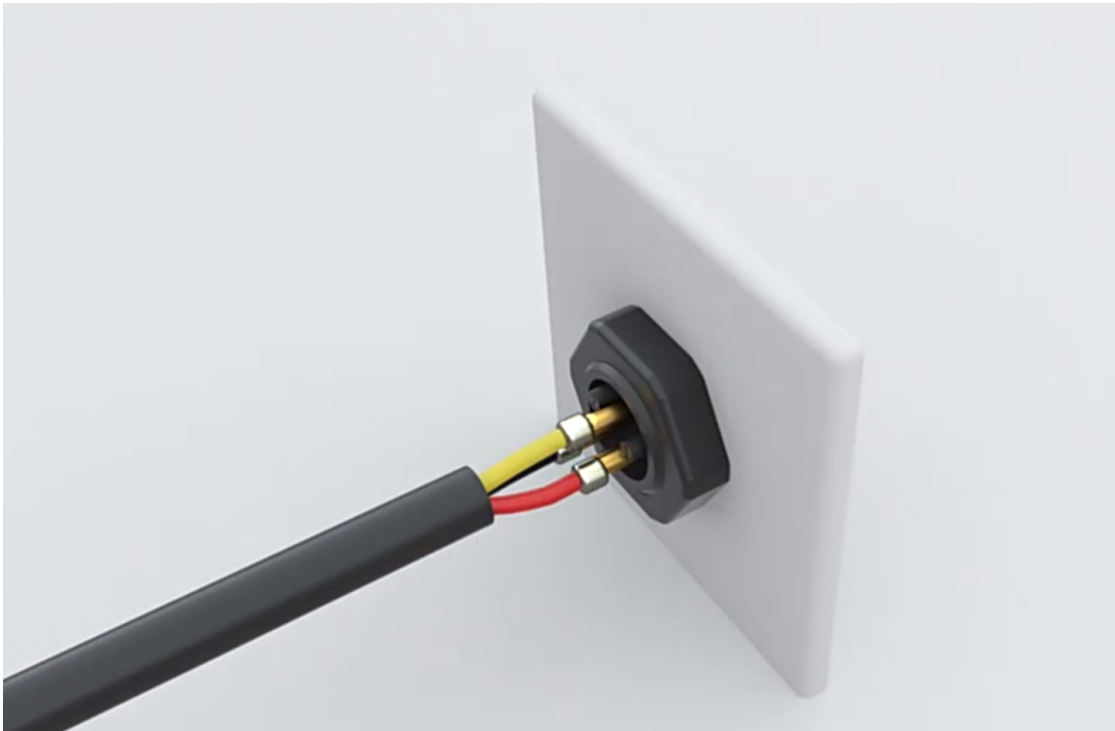


Figure 6.4: Male terminal mounting method of metric connector[33]

Having defined the connection interface with the sensors and the enclosure for the sensor node PCB, and parts being chosen that satisfy all mechanical project requirements, we can move on with the design of the PCB. The requirements of the PCB will include the dimensions of the Spelsberg TK PC 1309-6-tm enclosure, and the Molex connectors.

Chapter 7

Design of the Sensor Node PCB

In this chapter, the design of the sensor node PCB will be presented. The CAD software to be used for the PCB design is Altium designer, however, the current version of the sensor node PCB was designed using EAGLE. As such, the schematics, footprints, placing, and routing had to be done from scratch, following the design requirements in section 1.5, as well as the design constraints set by the chosen connection interface and enclosure for the sensor node.

7.1 Definition of the board outline

The board shape is directly constrained by the chosen enclosure. The technical drawing of the Spelsberg TK PC 1309-6-tm enclosure is shown in Figure 7.1. However, Spelsberg also provides 3D CAD data for all their enclosures. This 3D data was imported into AutoCAD, the internal area selected with the mounting holes was selected, and then exported as a .DWG file. This file contained the outline of the internal area of the enclosure as well as the outline for the mounting holes, which was imported into Altium designer to generate the outline of the PCB. All sides of this outline were then adjusted by 1 mm to reduce the board size so a 1 mm leeway space could be left for the PCB inside the enclosure. This outline was then declared the board's outline as shown in Figure 7.2.

The defined PCB shape is 110x74 mm which has an area of 7,400 mm². Including the 23 mm gap that should be left for the antenna, the total area available for components would be 6,438 mm² which is smaller than the previous component area of 7,600 mm². However, on analysis of the current sensor node PCB, the PCB area is not being used efficiently. Nonetheless, this area was considered feasible

by increasing the efficiency of component placing, as well as changing the Wago 250-20X connectors to Molex connectors which have a smaller footprint. To achieve this, about 84 % of space should be saved in the new design which was considered possible since the current PCB underuses its component space, having about 30 % of its area unused, and component density is not as high as it can be.

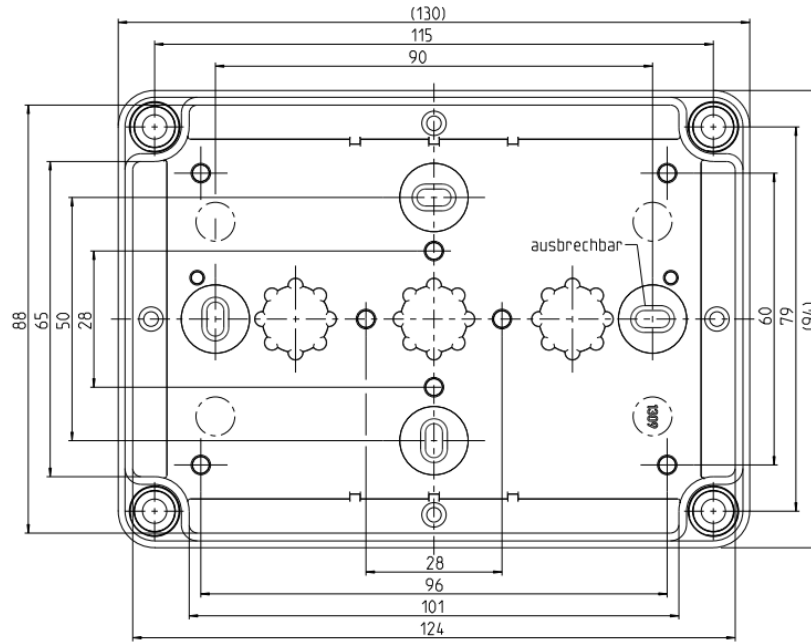


Figure 7.1: Technical drawing of Spelsberg TK PC 1309-6-tm enclosure [34]



Figure 7.2: Board shape for sensor node PCB

7.2 Definition of the PCB Antenna's Footprint

As explained in chapter 5, the chosen antenna topology to be integrated in the PCB design is the inverted-F antenna. However, since the board size and board stackup will change from this design with respect to the simulated model in chapter 4, the antenna will once again be simulated in CST studio and optimized for the new board characteristics, before integration with the sensor node PCB. With reference to Figure 4.35, the new dimensions of the antenna are shown in Table 7.1, and Figure 7.3 shows the model of the new board stackup, a PCB with 4 layers: Three ground planes and one signal plane.

Parameter	Dimension (mm)
X	74
Y	87.5
L1	20.25
L2	28.34
L3	18.90
L4	3.97
W	0.8

Table 7.1: Dimensions of PCB inverted-F antenna

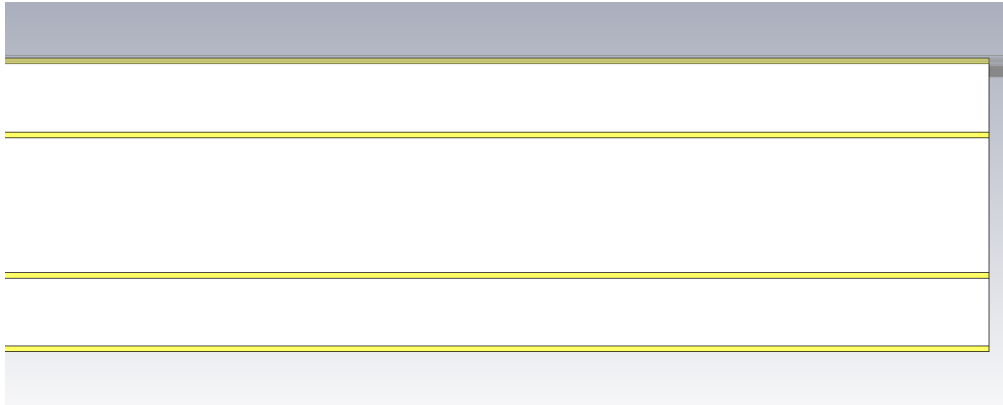


Figure 7.3: 4 layer board stackup in CST Studio of the sensor node PCB

The simulation of this model is shown in Figure 7.4. As with the previous model of the inverted-F antenna, the short circuit stub has to be optimized so that the

input impedance of the antenna at the resonant frequency is completely real and equal to $50\ \Omega$. This can be seen in the smith chart representation of the simulation results. The input impedance of the designed antenna was simulated to be $50.74\ \Omega$ at the resonant frequency of $867.5\ \text{MHz}$, proving that the antenna was correctly optimized and ready to be integrated into the PCB.

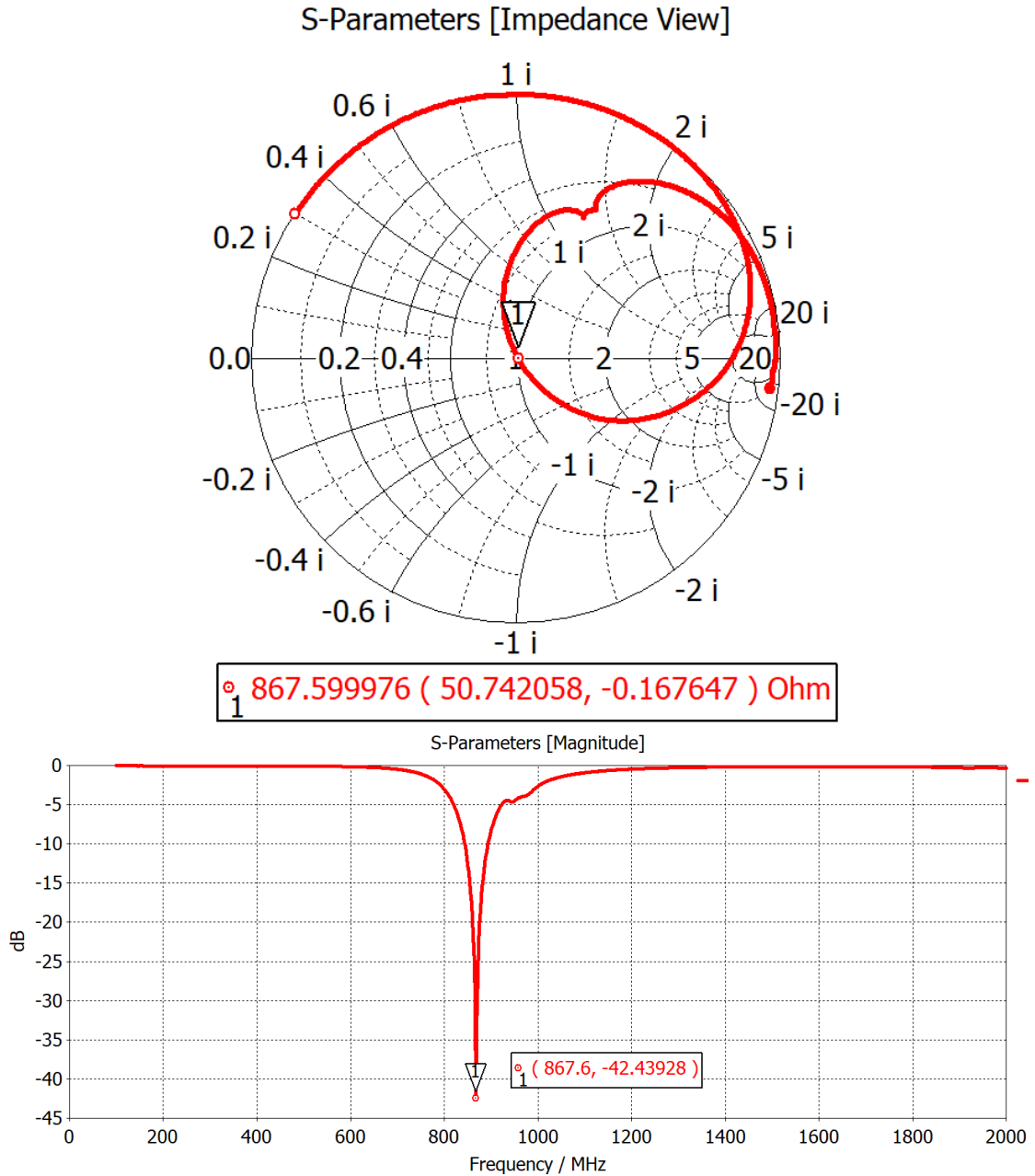


Figure 7.4: Simulation results a) Smith chart, b) S_{11}

To integrate the antenna into the PCB design, a PCB component was created in Altium designer, composed by a schematic symbol and a PCB footprint, as shown in Figure 7.5. This component can then be placed in any schematic to then be placed into a PCB design.

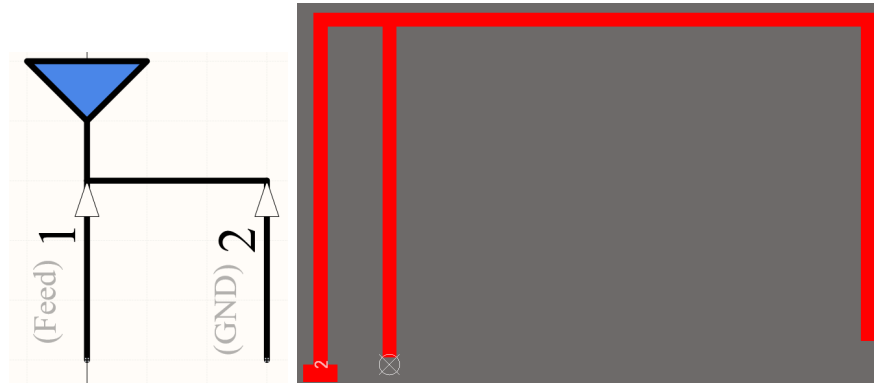


Figure 7.5: Antenna PCB component: a)Schematic symbol, and b) PCB footprint

7.3 Creation of PCB Schematics

For the full schematics, refer to Appendix C. These schematics were designed based on the current sensor node PCB schematics. However, most components were changed. All passive components were selected to the most cost effective components, since some of the old components were directly replaceable by cheaper alternatives with the same characteristics. To use the available PCB space efficiently, most passive components were changed to the 0402 package. The Wago 250-20X connectors were changed to the Molex connectors as per the proposed connection interface. A safe mode switch was added to support a desired future firmware update that disables some parts of the communication sequence when maintaining the PCB. Test points were added to do measurements with a voltmeter on the battery levels and regulated voltage levels of the PCB. An SMA connector was added to test the antenna of first prototype of the board in the anechoic chamber. To select whether the 1SJ module or the SMA port feeds the antenna, two 0Ω resistors were added. Only one will be assembled onto the board, selecting which feeding mechanism will be used. The full BOM of the PCB can also be seen in Appendix C.

7.4 Design of the PCB

With the BOM and schematics defined, the next step was to design the PCB. Using the SnapEDA plugin of Altium designer, the footprints for all the designed components were imported into the PCB design environment and placed. The stackup for this board is a 4 layer board with the top two layers and the last one (from the top to the bottom of the PCB) being ground planes, and the third layer a power signal plane to distribute 3.3 V across the board.

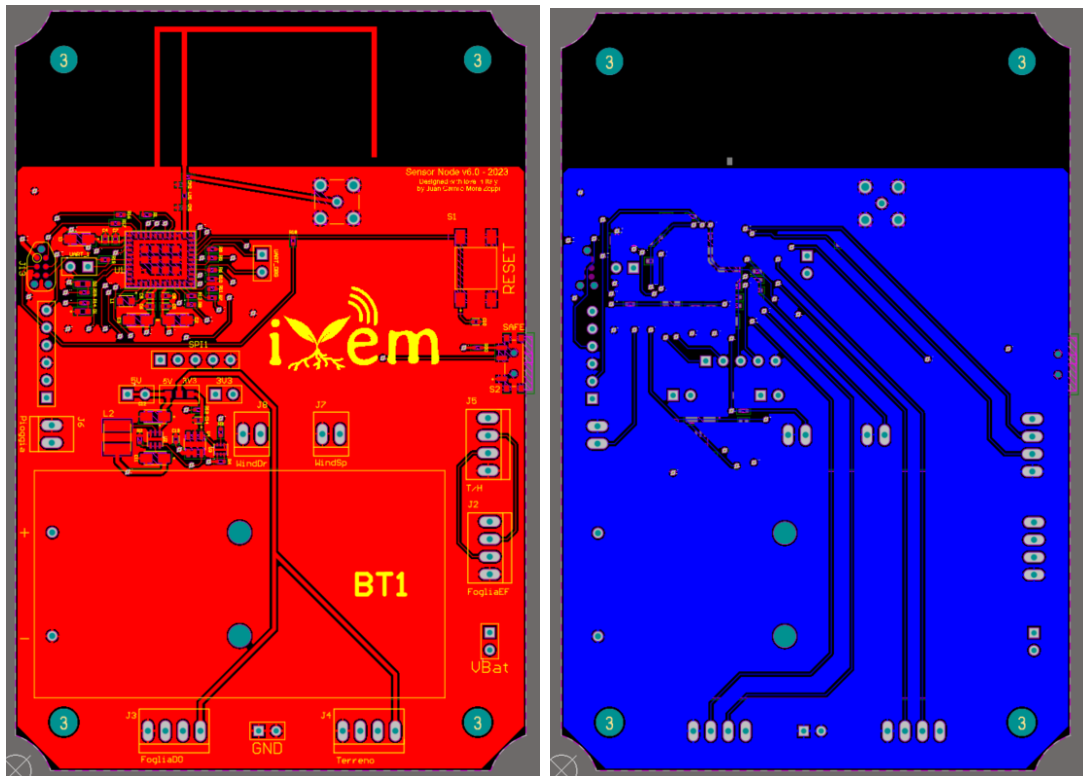


Figure 7.6: Sensor node PCB: a) Top layer b) Bottom layer

As we can see in Figure 7.6, all the components were successfully placed on the PCB. Three main areas can be identified: The 1SJ module and its components, the power interface, and finally the connectors. It can be observed that the PCB has some left over space where the iXem logo is located, revealing that the board size could be even smaller. This shows how inefficient the current generation of the PCB is with its space utilization and component density. The Molex connectors were placed around the PCB so as to place each one close to one of the metric knock outs in the enclosure. This way the cable management between the panel-mounted male metric connectors to the board is as simple as possible. As with the current

generation of the board, the electronic components can be found only on the top layer of the board due to mounting the PCB in the enclosure without the use of standoffs. If standoffs were to be used, the bottom of the board could be utilized, saving even more space and reducing board size. The safe mode switch was placed on the side of the board and easily accessible but in a position where it can't be accidentally switched.

With the design of the PCB completed its fabrication output files were produced and sent for manufacturing and component assembly at Eurocircuits. The produced and assembled board can be seen in Figure 7.7.



Figure 7.7: Sensor node PCB after manufacturing and assembly

Chapter 8

Validation of the Sensor Node

In this chapter, the proposed design of the sensor node will be tested to prove its validity and functionality. The tests to be done are:

- **Anechoic chamber testing:** Using the integrated 50Ω connector in the board, the antenna will be tested to verify its performance when surrounded by the other components in the populated board. As with the mock antenna tests, the anechoic chamber will measure the S_{11} parameter of the antenna to know its resonant frequency and quality of impedance matching.
- **Lab tests without enclosure:** The firmware for the current generation of sensor node PCBs will be loaded and its initial functionality will be verified with an array of the compatible sensors.
- **Field test:** The PCB will be installed in a real use-case scenario, measuring weather data continuously for a set amount of time. This will validate the stability of the PCB's behavior, as well as the efficacy of the mechanical design at simplifying the assembly and ensuring the protection of the PCB against the elements.

8.1 Anechoic chamber testing

The sensor node PCB was assembled with the 50Ω SMA connector and the 0Ω jumper was soldered in the position where the SMA connector feeds the antenna instead of the 1SJ module. As with the previous anechoic chamber tests, the antenna's radiation pattern was measured every 2° on 3 different polar axes, as well as the S_{11} parameter. The setup for the tests is shown in Figure 8.1

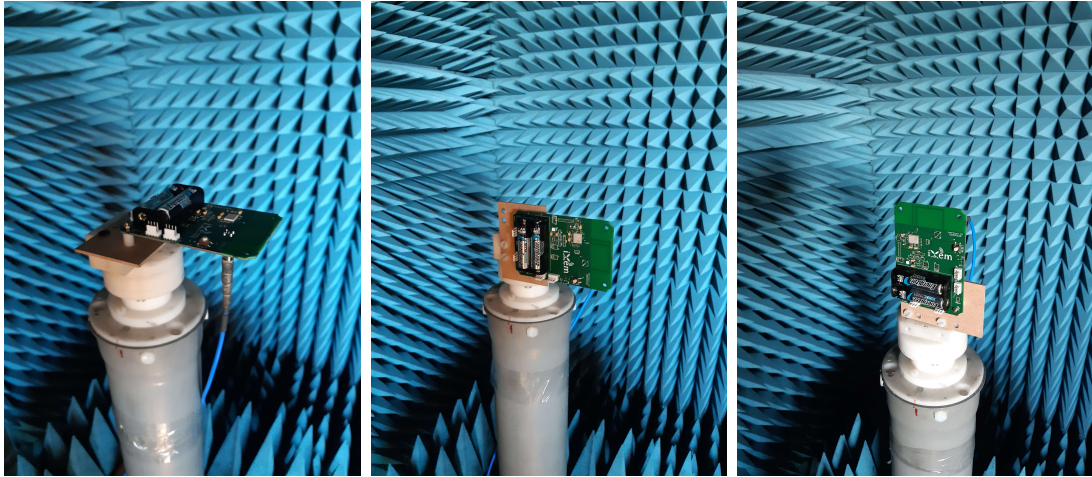


Figure 8.1: Test setup: a) $\phi = 0$, b) $\phi = 90$, and c) $\theta = 90$

From the test results in Figure 8.2, we can observe that the antenna has a resonant frequency of 865 MHz, with an S_{11} value of -24.48 dB at this frequency. The -10 dB Bandwidth from 840 MHz to 888 MHz covers the entire EU868 channel frequencies. This performance shows that the antenna has good impedance matching throughout the desired bandwidth. On the other hand, Figure 8.4 shows that the pattern behavior is omnidirectional as designed and simulated. These characteristics validate the antenna design on the PCB.

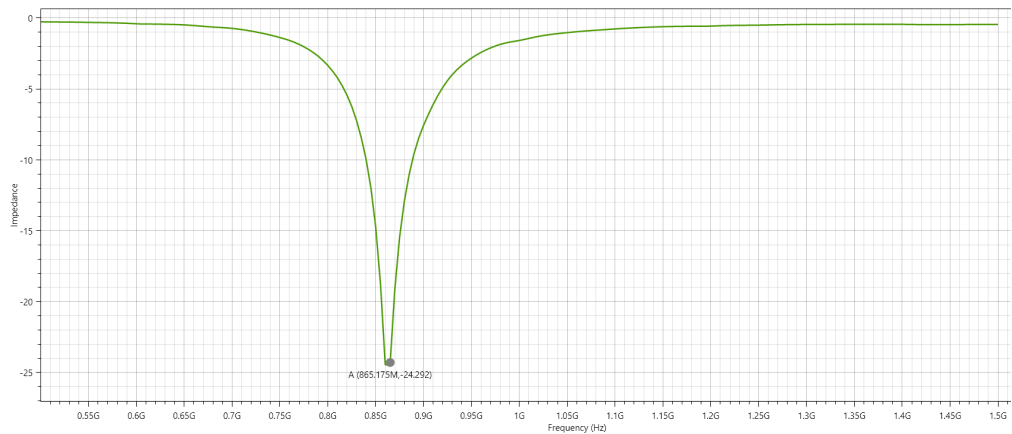


Figure 8.2: Test results: S_{11}

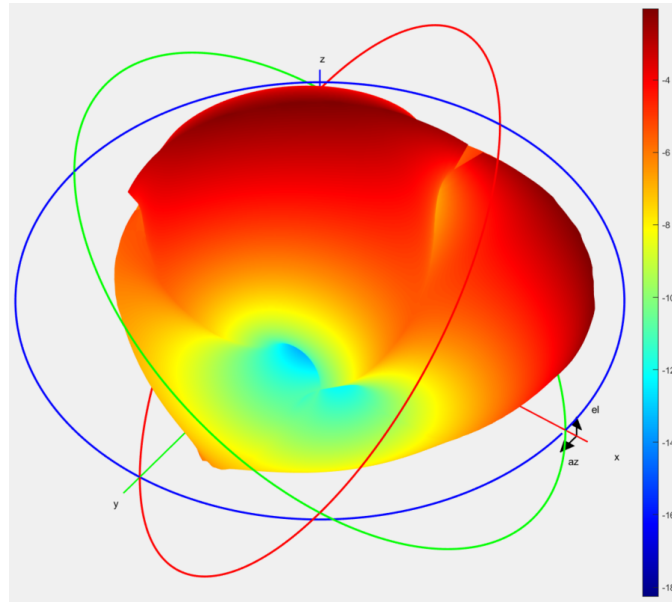


Figure 8.3: Approximate 3D radiation pattern

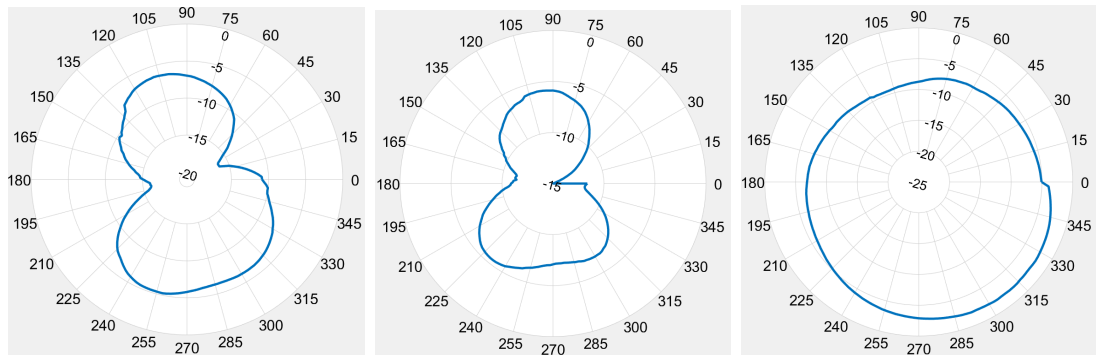


Figure 8.4: Radiation pattern cuts: a) $\phi = 0$, b) $\phi = 90$, and c) $\theta = 90$

8.2 Lab tests without enclosure

To test the basic functionality of the board, the firmware was flashed onto it, and the live packets were monitored on The Things Network platform. The firmware's first interaction with TTN is to join to the network server by sending a join request packet that is received by any gateways in its transmission range. If the join request is sent correctly, the end device is now joined to the TTN user application and can start sending and receiving data through uplinks and downlinks, respectively. On a successful join request, the TTN console reports the RSSI and SNR of the end

device to the gateway, showing the quality of the transmission.

Downlinks can be sent to the sensor node via the TTN application console. The sensors to be connected to the sensor node are configured through these downlinks, where each sensor has a specific value to be included in the downlink payload. The firmware reads this downlink data and starts acquiring data from the configured sensors. Uplinks are sent every 10 minutes by the sensor node, and their payload is the acquired data from the sensors, as well as the battery level. This data is then collected and shown in the iXem dashboard. For the initial lab test, the setup in Figure 8.5 was done. The board was left in the lab with no enclosure, and was configured to acquire data from the Air Temperature and Humidity sensor, seen in the bottom of Figure 8.5. A rain sensor was also connected, as seen on the top of Figure 8.5, but since the test is done indoors, it will not activate.



Figure 8.5: Initial Test: Setup

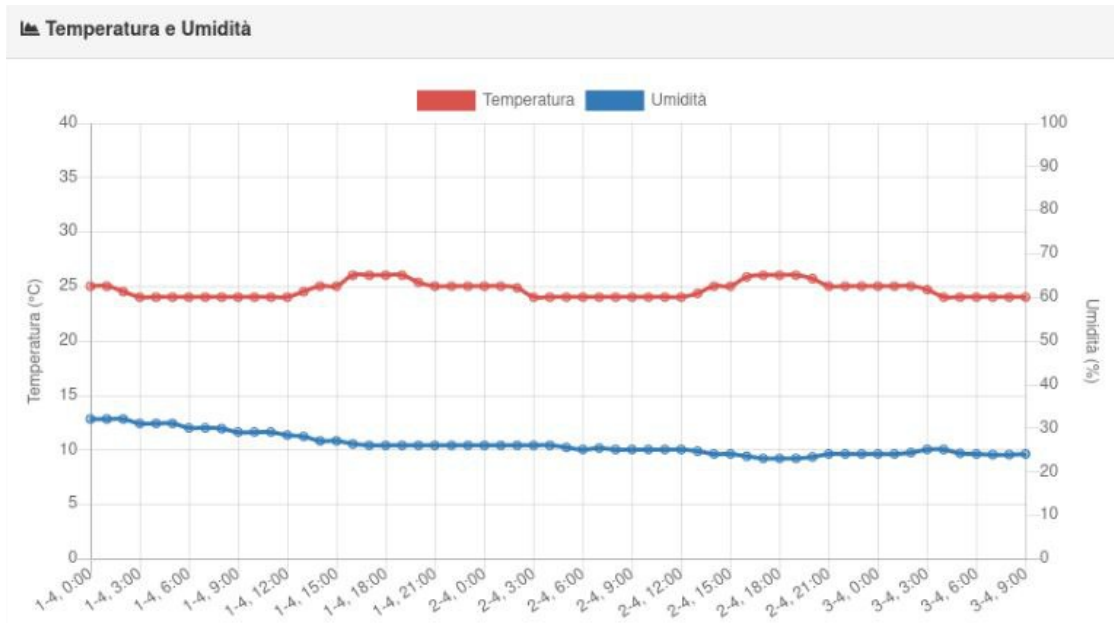


Figure 8.6: Initial Test: Results

To test the functionality and stability of the sensor node, the initial test was carried out during the weekend from April 1st at midnight to April 3rd at 9:00 AM, monitoring the temperature and humidity of the iXem Lab. Figure 8.6 shows the dashboard view of the the results. The test was carried out in a lab environment that counts with an HVAC system. The test results reflect this due to the stability of the temperature, which oscillated around 25° by $\pm 1^{\circ}$ throughout the weekend, and humidity, which stabilized at 20%.

Also, during this test, whenever the rain sensor was manually actuated, simulating rain, the following uplink transmitted correctly the times the sensor was actuated. Finally, the battery level did not drop from 100% after transmitting data all weekend. The test results indicate that the new sensor node PCB is able to:

- Transmit and receive data through LoRa
- Conform to LoRaWAN EU868 by joining the TTN iXem application
- Be configured by downlinks sent through the TTN application console
- Acquire sensor data correctly from the configured sensors
- Transmit uplinks with the acquired sensor data

- Have stable performance with no human interaction
- Have very low power consumption during operation

The conclusion drawn from this test is that the version 6.0 sensor node PCB accomplishes all of the functionalities required by the project with stability, and was found suitable to be tested further in a test of a completely assembled iXem Wine station.

8.3 Field test

Until now, only the electrical characteristics of the designed sensor node have been tested. To test the designed sensor node completely, a full test of the design was done, including the proposed mechanical design and interconnection interface. The sensor node PCB was mounted in a real use case environment using the proposed mechanical design as shown in Figure 8.7. It was then left in the Politecnico di Torino's terrace, where the iXem labs test all of their prototypes. In this location a small vine is located, with proximity to an installed LoRaWAN gateway, and simulates the real use-case conditions of the iXem Wine stations. A noteworthy fact about the setup of this station was how much easier the assembly process was compared to the current generation stations.



Figure 8.7: Field Test: Setup

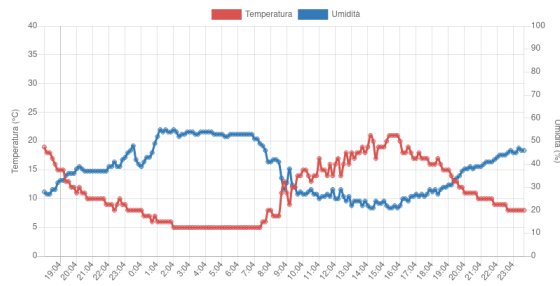


Figure 8.8: Field Test: Results

As we can see in Figure 8.8, the acquired data for rain, temperature, humidity, and battery level was transmitted throughout the test process without losing any packets (2 days, transmitting at 10 minute intervals). As opposed to the lab test, the temperature changed according to the time of day, and since there was no rain in the test days, it remained at 0mm during the test.

Sensor Node	Avg. SNR	Avg. RSSI
Current Gen	5.33	-93.6
New Gen	10.2	-90.7

Table 8.1: Comparison of SNR and RSSI of external and integrated antenna

Other important parameters that the TTN console allows us to monitor are the SNR and RSSI of any given uplink. When compared to a current generation sensor node with the external antenna we observed, as shown in Table 8.1, that the performance of the new integrated antenna is not only comparable but actually better than the external antenna. With these results we can conclude that the new design for the sensor node is able to perform all the operations that the current sensor node does, and that the designed antenna is able to transmit in the LoRaWAN EU868 parameters with good radiative characteristics.

Chapter 9

Conclusions and Future Work

In this chapter, the objectives set in section 1.5 will be reviewed and compared to the results of the research to determine if they were achieved through this work. Afterwards, some ideas and observations that emerged throughout the development of this thesis will be discussed. These could improve the iXem wine product even further, and could be applied in a new revision of the sensor node.

9.1 Conclusions

Referring to the research objectives and project requirements in section 1.5, we can conclude that all were completed successfully. Research on planar antenna topologies resulted in the design of an inverted-F antenna in section 7.2 integrated in the sensor node PCB that had good performance in all tests. Research on weatherproof enclosures and interconnection mechanisms led to the mechanical design proposed in chapter 6. And finally, the use of PCB design principles produced the prototype for the next generation of sensor node PCBs as shown in chapter 7, that performed correctly in both the controlled environment tests, as well as the use-case scenario tests.

The only thing left is to conclude if the proposed design was able to accomplish all design objectives and eliminate all of the shortcomings of the current generation sensor node, we must first review the initial evaluations that led to the development of this thesis. We can categorize the current generations shortcomings in 5 main categories: Assembly, modularity, installation, maintenance, and weather protection.

- **Assembly:** The new interconnection mechanism using the AOHUA metric

connectors, as well as profiting from the presence of the metric knockouts in the weatherproof enclosure, allowed to decrease the assembly complexity. Assembly times were reduced due to the ability to assemble the sensors, enclosure and PCB separately. Also the consistency of the assembly was increased significantly by eliminating the need to drill holes through the enclosure, which reduced the risk of compromising the weatherproof rating of the enclosure,

- **Modularity:** The use of the AOHUA metric connectors permits the sensor node and the sensors to be completely modular. The sensors can be plugged and unplugged to the enclosure directly, making the iXem stations a true plug-and-play system. New sensors can be installed even if the station is already mounted only using a screwdriver to remove the knockouts from the enclosure.
- **Installation:** The improved modularity allows all the parts of the sensor node to be assembled and transported separately. This improves the installation experience by allowing the technician to install an iXem Wine Station one part at a time and connect all of the sensors to the sensor node without the need of specialized tools. If the sensor node and all of its sensors are mounted using zip ties or other mounting mechanisms that can be installed by hand, then a technician would not need any tools at all since all interfaces between the sensors and sensor nodes can be plugged and unplugged by hand, without the need of opening the enclosure.
- **Maintenance:** The increased modularity and the change from cable glands to metric connectors allow iXem Wine stations to be maintained easily. In the case of a damaged sensor or PCB, the damaged part can be swapped easily without the need of any tools at all in the case of a damaged sensor, and only a screwdriver in the case of a damaged PCB.
- **Weather protection:** The new enclosure and connection interface, aided by the lack of the external antenna, allow for a consistent assembly, providing an IP66 rated protection from the weather, perfect for the use-case applications of the iXem Wine stations. Also, in the case of a damaged sensor, it can be unplugged from the sensor node and shipped to the lab for diagnosis, while leaving the rest of the sensor node working without compromising the PCB to the weather.

With this we can ascertain that all research and project objectives were achieved, concluding this thesis.

9.2 Improvement opportunities

The result of this thesis is intended as the prototype for the 6th generation sensor node of the iXem Wine stations. As a prototype, it can be improved further. Since the antenna's performance was already validated in this thesis, the SMA connector can be removed on the production version. Another hardware change is to expose more pins in the 1SJ module to be able to connect to more sensors. This board can also be used as a trustworthy basis for all kinds of applications using LoRaWAN®end devices. The modularity of the new design allows for flexibility in the applications with minimal hardware changes.

However, the biggest concern right now in the iXem Wine project is to review and rewrite the firmware of the sensor node, which was outside the scope of this thesis. The current version of the firmware has some bugs that lead to entire sensor nodes to become not operational, and as such are very important to eliminate. With a new firmware, coupled with the new hardware design, we expect to be able to deliver the most reliable version of the iXem Wine product.

Appendix A

Matlab code: generate radiation pattern from anechoic chamber data

```
1 %----- Phi 90 -----%
2
3 fid = fopen('DT/Dipole/Dipole_Phi90deg_VpolProbe.txt');
4 read = 0;
5 a837V = {}; a843V = {}; a849V = {}; a855V = {}; a861V =
   {}; a867V = {}; a873V = {}; a879V = {}; a885V = {};
   a891V = {}; a897V = {};
6
7 tline = 'a';
8 while ischar(tline)
9     tline = fgetl(fid);
10    if tline == '#'
11        read = 1;
12        continue;
13    elseif tline == '&' | tline == '@'
14        read = 0;
15        continue;
16    end
17    if read == 1
18        a = strsplit(tline, ';');
19        switch str2double(a(1))
```

```
20         case 837000000
21             a837V(end+1, :) = [a(2) a(3)];
22         case 843000000
23             a843V(end+1, :) = [a(2) a(3)];
24         case 849000000
25             a849V(end+1, :) = [a(2) a(3)];
26         case 855000000
27             a855V(end+1, :) = [a(2) a(3)];
28         case 861000000
29             a861V(end+1, :) = [a(2) a(3)];
30         case 867000000
31             a867V(end+1, :) = [a(2) a(3)];
32         case 873000000
33             a873V(end+1, :) = [a(2) a(3)];
34         case 879000000
35             a879V(end+1, :) = [a(2) a(3)];
36         case 885000000
37             a885V(end+1, :) = [a(2) a(3)];
38         case 891000000
39             a891V(end+1, :) = [a(2) a(3)];
40         case 897000000
41             a897V(end+1, :) = [a(2) a(3)];
42     end
43 end
44 end
45 fclose(fid);
46
47 fid = fopen('DT/Dipole/Dipole_Phi90deg_HpolProbe.txt');
48 read = 0;
49 a837H = {}; a843H = {}; a849H = {}; a855H = {}; a861H =
    {}; a867H = {}; a873H = {}; a879H = {}; a885H = {};
    a891H = {}; a897H = {};
50
51 tline = 'a';
52 while ischar(tline)
53     tline = fgetl(fid);
54     if tline == '#'
55         read = 1;
56         continue;
57     elseif tline == '&' | tline == '@'
58         read = 0;
```

```

59     continue;
60 end
61 if read == 1
62     a = strsplit(tline, ';');
63     switch str2double(a(1))
64         case 837000000
65             a837H(end+1, :) = [a(2) a(3)];
66         case 843000000
67             a843H(end+1, :) = [a(2) a(3)];
68         case 849000000
69             a849H(end+1, :) = [a(2) a(3)];
70         case 855000000
71             a855H(end+1, :) = [a(2) a(3)];
72         case 861000000
73             a861H(end+1, :) = [a(2) a(3)];
74         case 867000000
75             a867H(end+1, :) = [a(2) a(3)];
76         case 873000000
77             a873H(end+1, :) = [a(2) a(3)];
78         case 879000000
79             a879H(end+1, :) = [a(2) a(3)];
80         case 885000000
81             a885H(end+1, :) = [a(2) a(3)];
82         case 891000000
83             a891H(end+1, :) = [a(2) a(3)];
84         case 897000000
85             a897H(end+1, :) = [a(2) a(3)];
86     end
87 end
88 end
89 fclose(fid);
90
91 MagV = (sqrt(str2double(a861V(:, 1)).^2 + str2double(
    a861V(:, 2)).^2)/sqrt(-0.0911505222320557^2 +
    0.129815727472305^2));
92 MagH = (sqrt(str2double(a861H(:, 1)).^2 + str2double(
    a861H(:, 2)).^2)/sqrt(-0.0911505222320557^2 +
    0.129815727472305^2));
93 MagP90 = 10*log(sqrt(MagV.^2+MagH.^2));
94 MagP90(end+1) = MagP90(1);
95

```

```

96 Angle = linspace(0,360,181)';
97 tbl = table(Angle, MagP90);
98 figure('Name','Dipole Radiation Pattern - Phi90', '
    NumberTitle','off')
99 pol = polarpattern(tbl.Angle,tbl.MagP90,MagnitudeLim
    =[-30 5],TitleTop='Dipole Radiation Pattern - Phi90',
    LineWidth=3,TitleTopFontSizeMultiplier=1.5);
100
101 figure('Name','Radiation Pattern - Phi90', 'NumberTitle'
    , 'off')
102 lin = plot(tbl.Angle,tbl.MagP90);
103 title('Dipole Radiation Pattern - Phi90')
104
105 %----- Theta 90 -----%
106
107 fid = fopen('DT/Dipole/Dipole_Theta90deg_VpolProbe.txt')
    ;
108 read = 0;
109 a837V = {}; a843V = {}; a849V = {}; a855V = {}; a861V =
    {}; a867V = {}; a873V = {}; a879V = {}; a885V = {};
    a891V = {}; a897V = {};
110
111 tline = 'a';
112 while ischar(tline)
113     tline = fgetl(fid);
114     if tline == '#'
115         read = 1;
116         continue;
117     elseif tline == '&' | tline == '@'
118         read = 0;
119         continue;
120     end
121     if read == 1
122         a = strsplit(tline, ';');
123         switch str2double(a(1))
124             case 837000000
125                 a837V(end+1, :) = [a(2) a(3)];
126             case 843000000
127                 a843V(end+1, :) = [a(2) a(3)];
128             case 849000000
129                 a849V(end+1, :) = [a(2) a(3)];

```

```

130         case 855000000
131             a855V(end+1, :) = [a(2) a(3)];
132         case 861000000
133             a861V(end+1, :) = [a(2) a(3)];
134         case 867000000
135             a867V(end+1, :) = [a(2) a(3)];
136         case 873000000
137             a873V(end+1, :) = [a(2) a(3)];
138         case 879000000
139             a879V(end+1, :) = [a(2) a(3)];
140         case 885000000
141             a885V(end+1, :) = [a(2) a(3)];
142         case 891000000
143             a891V(end+1, :) = [a(2) a(3)];
144         case 897000000
145             a897V(end+1, :) = [a(2) a(3)];
146     end
147 end
148 end
149 fclose(fid);
150
151 fid = fopen('DT/Dipole/Dipole_Theta90deg_HpolProbe.txt')
152     ;
153 read = 0;
154 a837H = {}; a843H = {}; a849H = {}; a855H = {}; a861H =
155     {}; a867H = {}; a873H = {}; a879H = {}; a885H = {};
156     a891H = {}; a897H = {};
157
158 tline = 'a';
159 while ischar(tline)
160     tline = fgetl(fid);
161     if tline == '#'
162         read = 1;
163         continue;
164     elseif tline == '&' | tline == '@'
165         read = 0;
166         continue;
167     end
168     if read == 1
169         a = strsplit(tline, ';');
170         switch str2double(a(1))

```

```
168         case 837000000
169             a837H(end+1, :) = [a(2) a(3)];
170         case 843000000
171             a843H(end+1, :) = [a(2) a(3)];
172         case 849000000
173             a849H(end+1, :) = [a(2) a(3)];
174         case 855000000
175             a855H(end+1, :) = [a(2) a(3)];
176         case 861000000
177             a861H(end+1, :) = [a(2) a(3)];
178         case 867000000
179             a867H(end+1, :) = [a(2) a(3)];
180         case 873000000
181             a873H(end+1, :) = [a(2) a(3)];
182         case 879000000
183             a879H(end+1, :) = [a(2) a(3)];
184         case 885000000
185             a885H(end+1, :) = [a(2) a(3)];
186         case 891000000
187             a891H(end+1, :) = [a(2) a(3)];
188         case 897000000
189             a897H(end+1, :) = [a(2) a(3)];
190     end
191 end
192 end
193 fclose(fid);
194
195 MagV = (sqrt(str2double(a861V(:, 1)).^2 + str2double(
196     a861V(:, 2)).^2)/sqrt(-0.0911505222320557^2 +
197     0.129815727472305^2));
198 MagH = (sqrt(str2double(a861H(:, 1)).^2 + str2double(
199     a861H(:, 2)).^2)/sqrt(-0.0911505222320557^2 +
200     0.129815727472305^2));
201 MagT90 = 10*log(sqrt(MagV.^2+MagH.^2));
202 MagT90(end+1) = MagT90(1);
203 Angle = linspace(0,360,181)';
204 tbl = table(Angle, MagT90);
205 figure('Name','Dipole Radiation Pattern - Theta90', '
    NumberTitle','off')
```

```

203 pol = polarpattern(tbl.Angle,tbl.MagT90,MagnitudeLim
    =[-30 5],TitleTop='Dipole Radiation Pattern - Theta90
    ',LineWidth=3,TitleTopFontSizeMultiplier=1.5);
204
205 figure('Name','Radiation Pattern - Theta90', '
    NumberTitle','off')
206 lin = plot(tbl.Angle,tbl.MagT90);
207 title('Dipole Radiation Pattern - Theta90')
208
209 %----- Phi 0 -----%
210
211 fid = fopen('DT/Dipole/Dipole_Phi0deg_VpolProbe.txt');
212 read = 0;
213 a837V = {}; a843V = {}; a849V = {}; a855V = {}; a861V =
    {}; a867V = {}; a873V = {}; a879V = {}; a885V = {};
    a891V = {}; a897V = {};
214
215 tline = 'a';
216 while ischar(tline)
217     tline = fgetl(fid);
218     if tline == '#'
219         read = 1;
220         continue;
221     elseif tline == '&' | tline == '@'
222         read = 0;
223         continue;
224     end
225     if read == 1
226         a = strsplit(tline, ';');
227         switch str2double(a(1))
228             case 837000000
229                 a837V(end+1, :) = [a(2) a(3)];
230             case 843000000
231                 a843V(end+1, :) = [a(2) a(3)];
232             case 849000000
233                 a849V(end+1, :) = [a(2) a(3)];
234             case 855000000
235                 a855V(end+1, :) = [a(2) a(3)];
236             case 861000000
237                 a861V(end+1, :) = [a(2) a(3)];
238             case 867000000

```

```

239         a867V(end+1, :) = [a(2) a(3)];
240     case 873000000
241         a873V(end+1, :) = [a(2) a(3)];
242     case 879000000
243         a879V(end+1, :) = [a(2) a(3)];
244     case 885000000
245         a885V(end+1, :) = [a(2) a(3)];
246     case 891000000
247         a891V(end+1, :) = [a(2) a(3)];
248     case 897000000
249         a897V(end+1, :) = [a(2) a(3)];
250     end
251 end
252 end
253 fclose(fid);
254
255 fid = fopen('DT/Dipole/Dipole_Phi0deg_HpolProbe.txt');
256 read = 0;
257 a837H = {}; a843H = {}; a849H = {}; a855H = {}; a861H =
    {}; a867H = {}; a873H = {}; a879H = {}; a885H = {};
    a891H = {}; a897H = {};
258
259 tline = 'a';
260 while ischar(tline)
261     tline = fgetl(fid);
262     if tline == '#'
263         read = 1;
264         continue;
265     elseif tline == '&' | tline == '@'
266         read = 0;
267         continue;
268     end
269     if read == 1
270         a = strsplit(tline, ';');
271         switch str2double(a(1))
272             case 837000000
273                 a837H(end+1, :) = [a(2) a(3)];
274             case 843000000
275                 a843H(end+1, :) = [a(2) a(3)];
276             case 849000000
277                 a849H(end+1, :) = [a(2) a(3)];

```

```

278         case 855000000
279             a855H(end+1, :) = [a(2) a(3)];
280         case 861000000
281             a861H(end+1, :) = [a(2) a(3)];
282         case 867000000
283             a867H(end+1, :) = [a(2) a(3)];
284         case 873000000
285             a873H(end+1, :) = [a(2) a(3)];
286         case 879000000
287             a879H(end+1, :) = [a(2) a(3)];
288         case 885000000
289             a885H(end+1, :) = [a(2) a(3)];
290         case 891000000
291             a891H(end+1, :) = [a(2) a(3)];
292         case 897000000
293             a897H(end+1, :) = [a(2) a(3)];
294     end
295 end
296 end
297 fclose(fid);
298
299 MagV = (sqrt(str2double(a861V(:, 1)).^2 + str2double(
300     a861V(:, 2)).^2)/sqrt(-0.0911505222320557^2 +
301     0.129815727472305^2));
302 MagH = (sqrt(str2double(a861H(:, 1)).^2 + str2double(
303     a861H(:, 2)).^2)/sqrt(-0.0911505222320557^2 +
304     0.129815727472305^2));
305 MagP0 = 10*log(sqrt(MagV.^2+MagH.^2));
306 MagP0(end+1) = MagP0(1);
307
308 Angle = linspace(0,360,181)';
309 tbl = table(Angle, MagP0);
310 figure('Name','Dipole Radiation Pattern - Phi0', '
    NumberTitle','off')
311 pol = polarpattern(tbl.Angle,tbl.MagP0,MagnitudeLim=[-30
    5],TitleTop='Dipole Radiation Pattern - Phi0',
    LineWidth=3,TitleTopFontSizeMultiplier=1.5);
312
313 figure('Name','Radiation Pattern - Phi0', 'NumberTitle',
    'off')
314 lin = plot(tbl.Angle,tbl.MagP0);

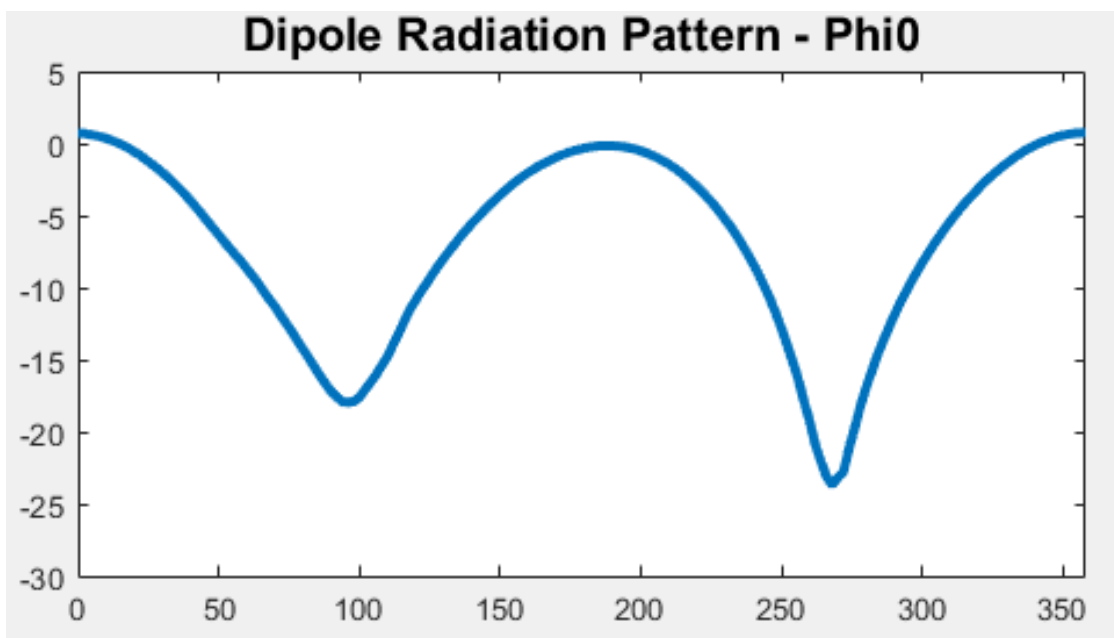
```

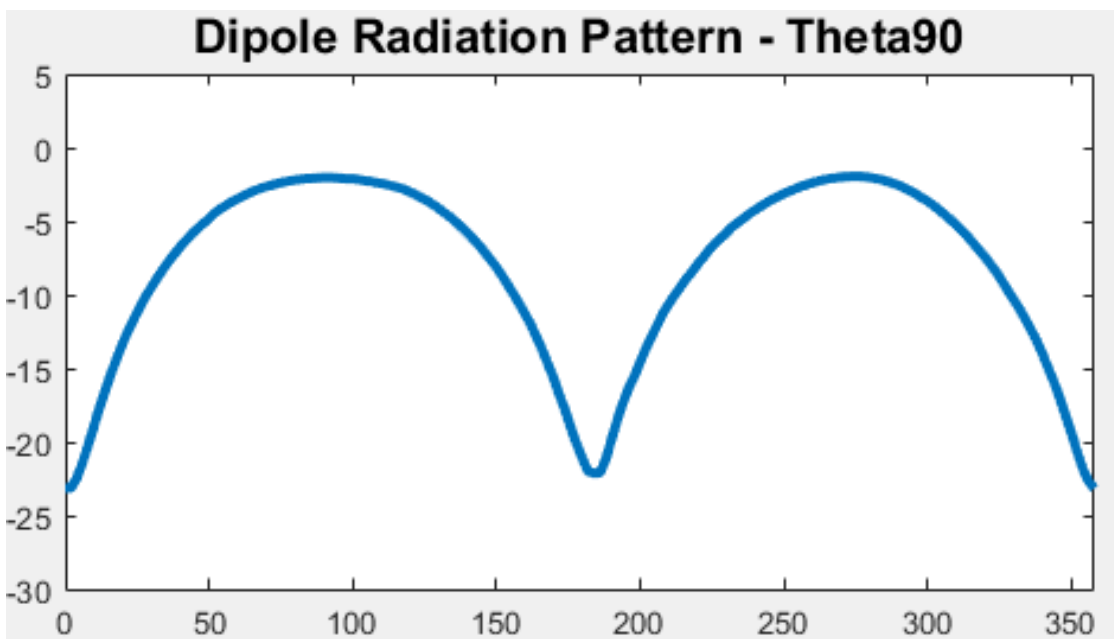
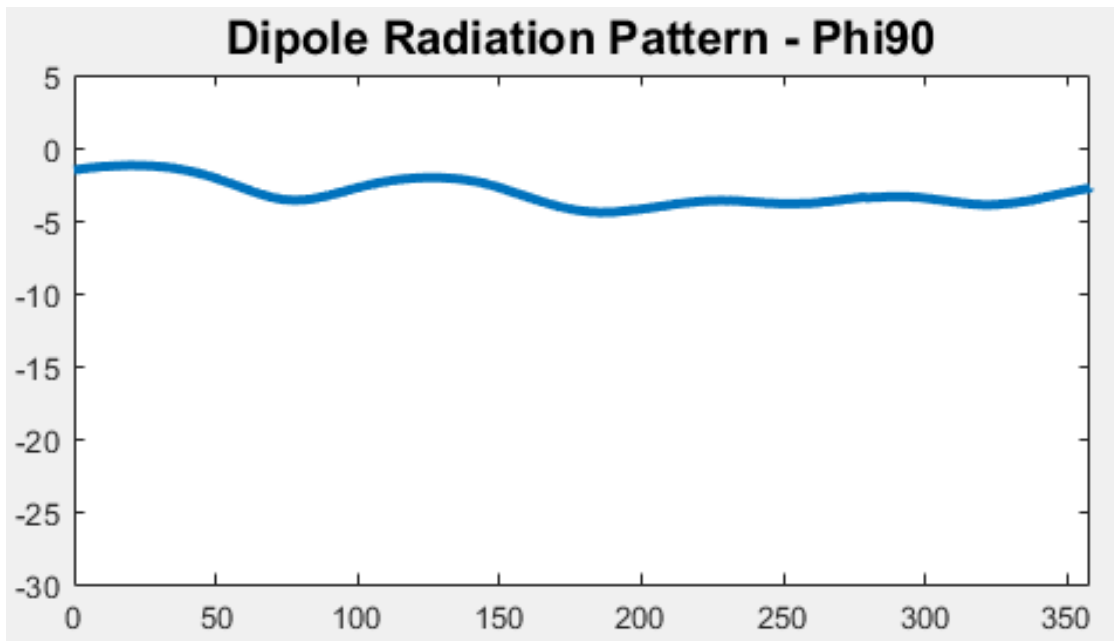
```
311 title('Dipole Radiation Pattern - Phi0')
312
313 %----- 3D Radiation
    -----%
314 figure('Name','Radiation Pattern - 3D', 'NumberTitle','
    off')
315
316 MagE=cat(1,MagP0,MagP90,MagT90,MagP0,flip(MagP90),flip(
    MagT90),flip(MagP0));
317 Phi=cat(1,zeros(181,1),90*ones(181,1),Angle,360*ones
    (181,1),270*ones(181,1),Angle,180*ones(181,1));
318 Theta=cat(1,Angle,Angle,90*ones(181,1),Angle,Angle,270*
    ones(181,1),Angle);
319 [xq,yq] = meshgrid(0:2:360, 0:2:360);
320 vq=griddata(Theta,Phi,MagE,xq,yq,'v4');
321 patternCustom(vq,Angle,Angle,"CoordinateSystem","polar")
    ;
```

Appendix B

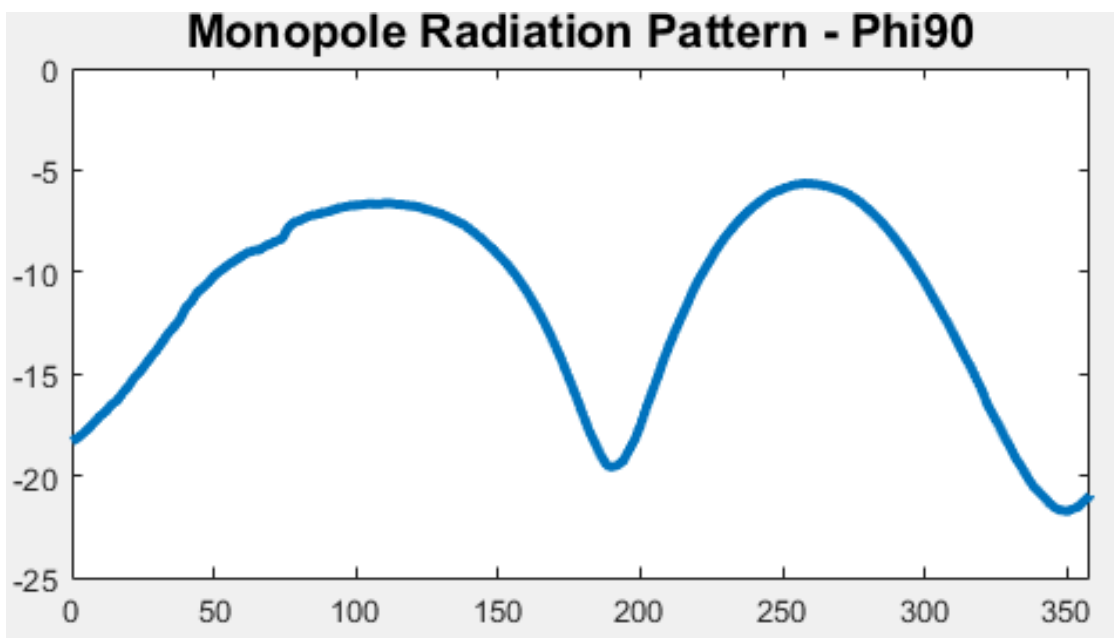
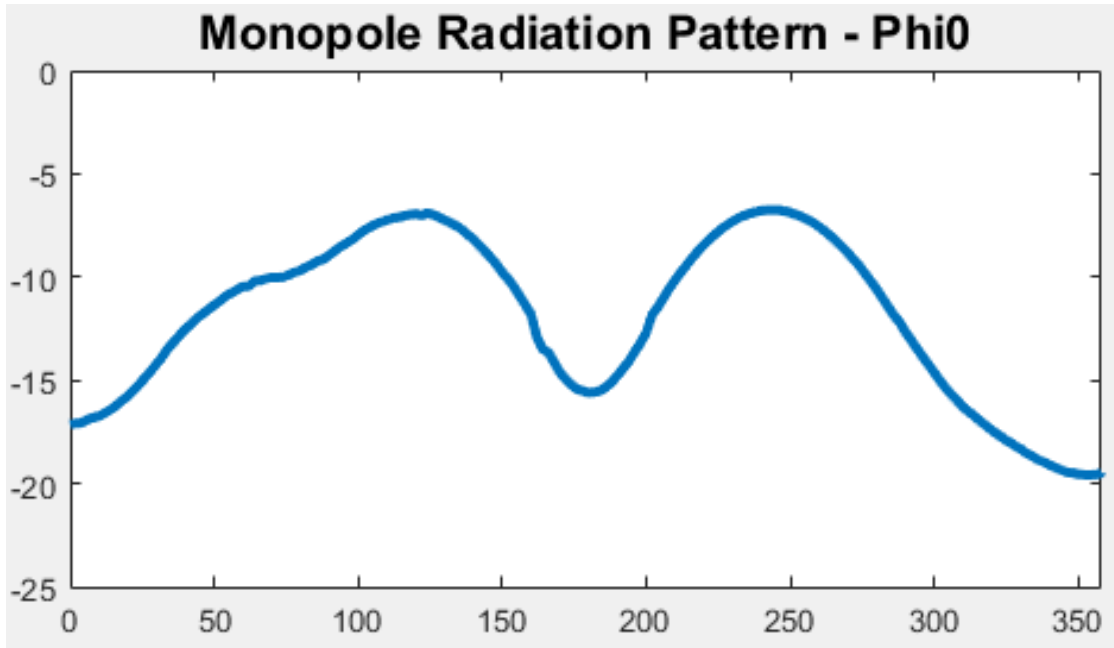
Radiation patterns: Cartesian representation

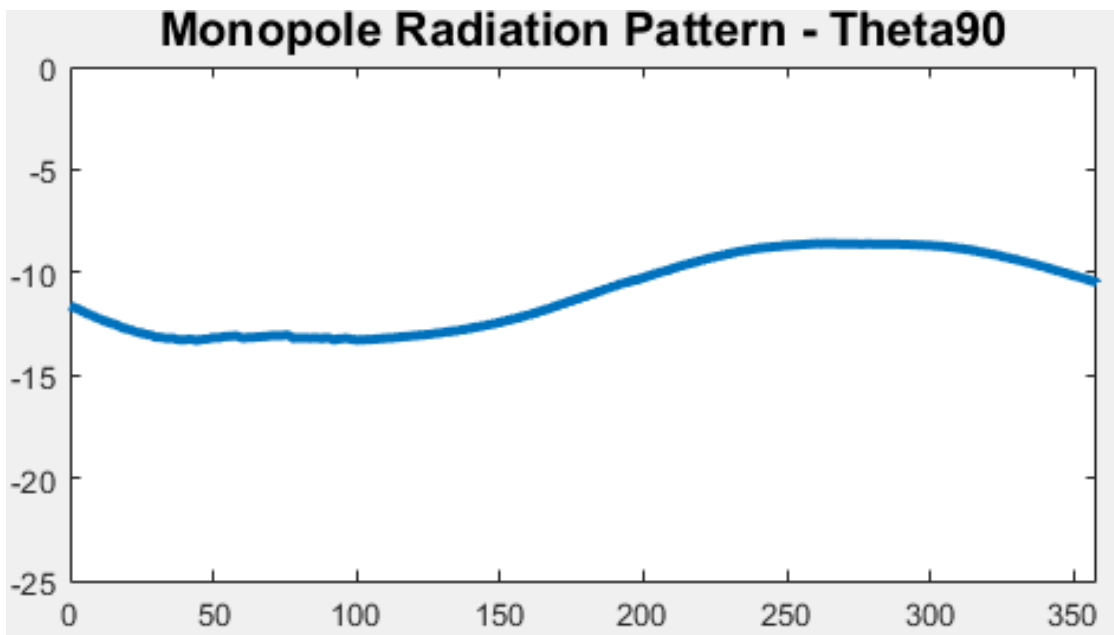
Dipole



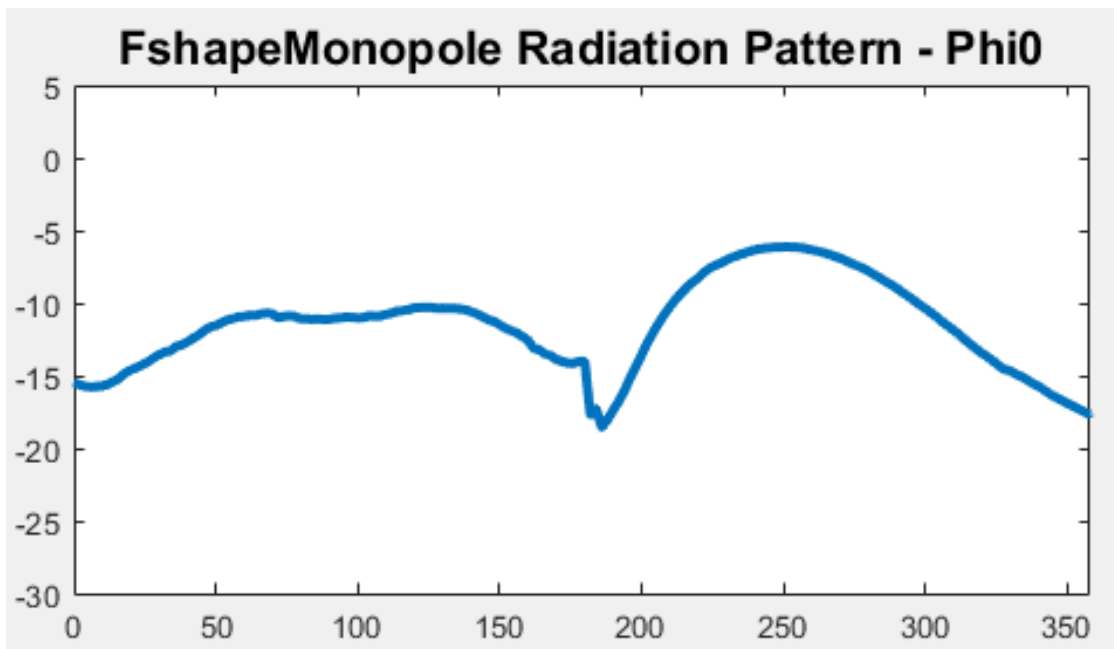


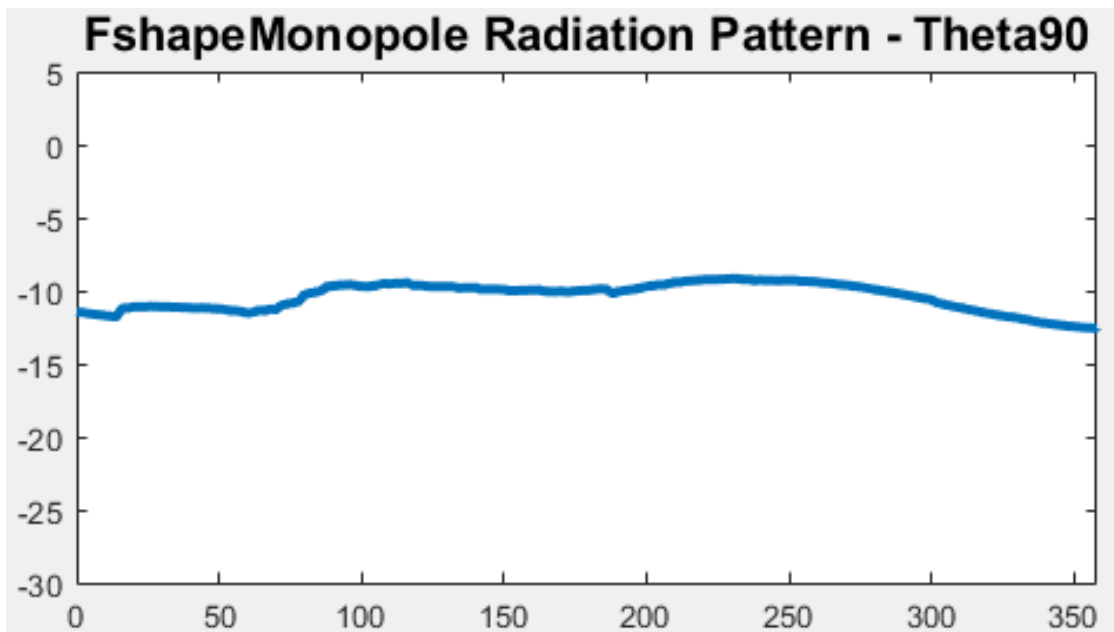
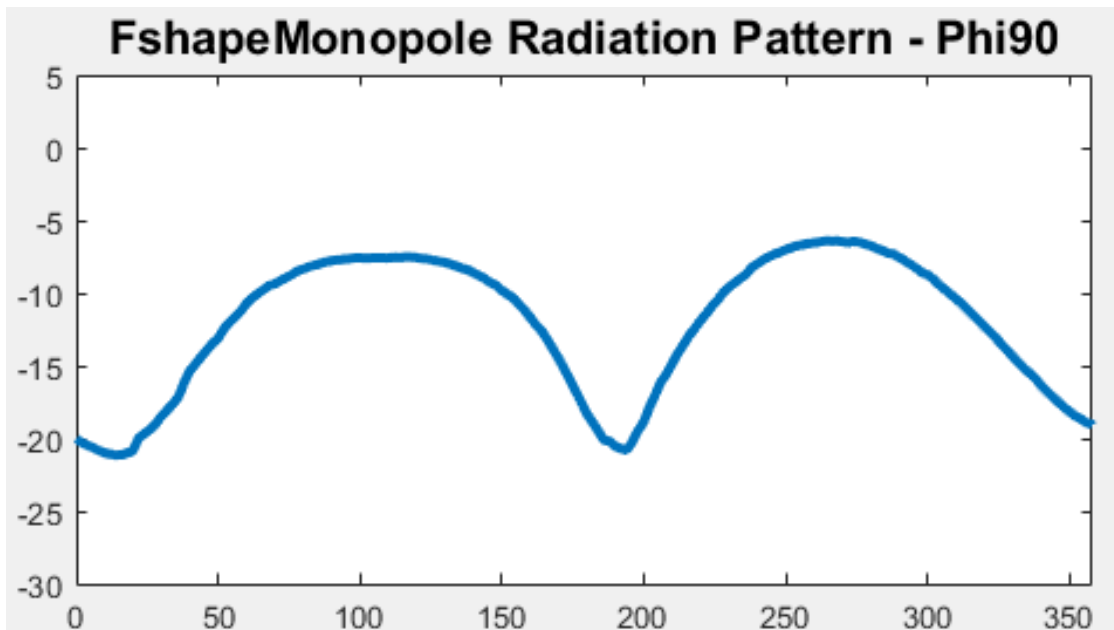
Monopole





Inverted-F

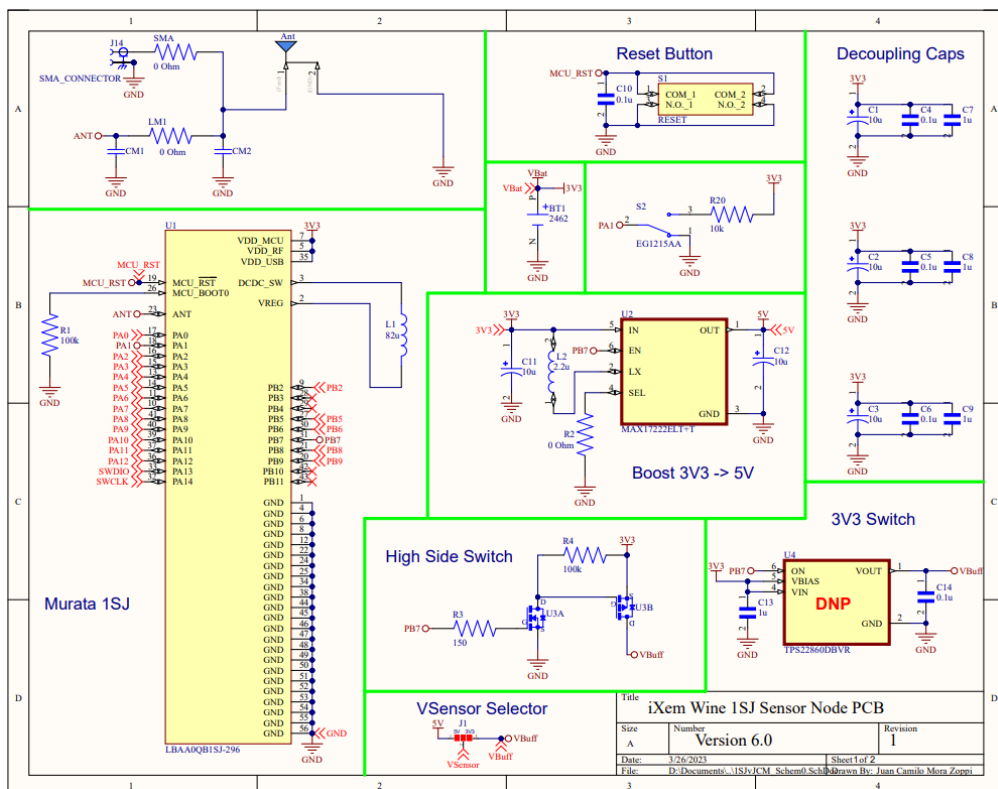




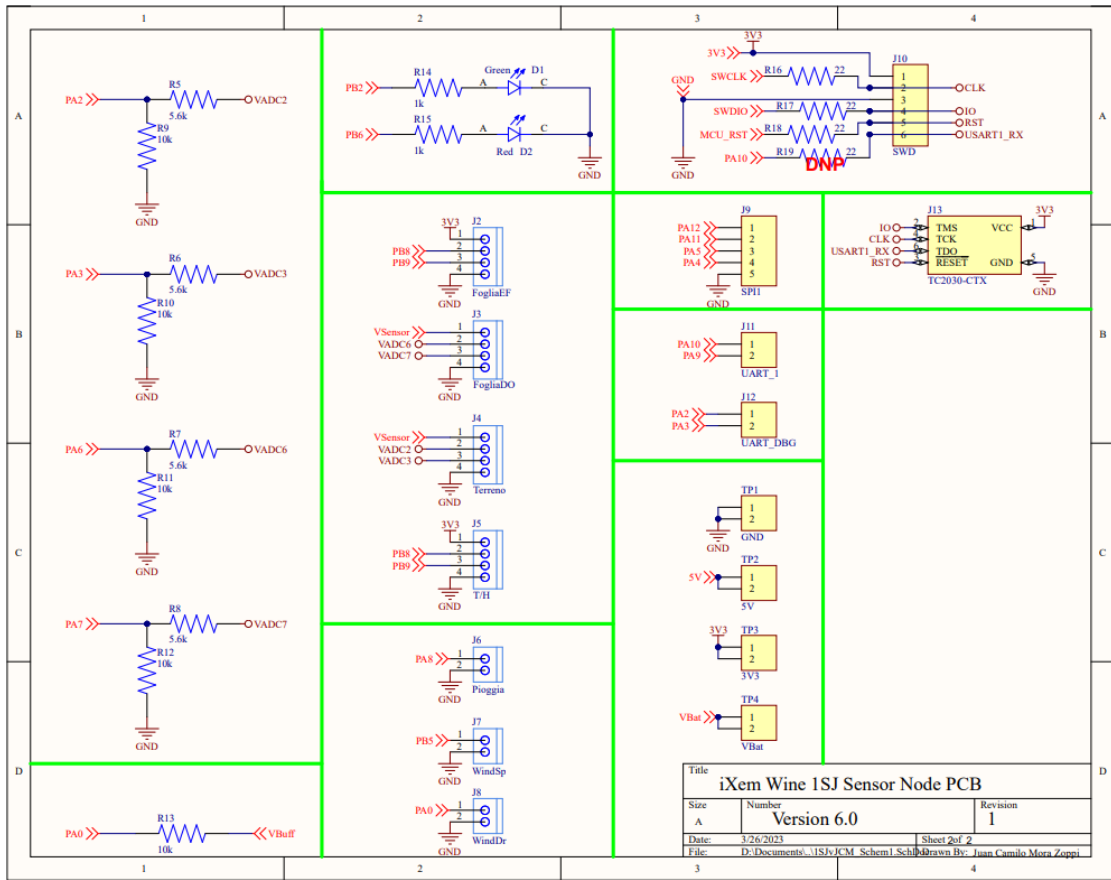
Appendix C

Sensor node PCB schematics and BOM

Schematics



Sensor node PCB schematics and BOM



BOM

	A	B	C	D
	Designator	Part Number	Quantity	Description
1	BT1	2462	1	Battery Holder (Open) AA 2 Cell PC Pin
2	C1, C2, C3, C11, C12	TAJA106K016YNJ	5	1ÅµF Molded Tantalum Capacitors 16V 1206 (3216 Metric) 110hm @ 100kHz
3	C4, C5, C6, C10, C14	CL05A104K05NNND	5	Cap Ceramic 0.1uF 16V X5R 10% SMD 0402
4	C7, C8, C9, C13	GRM155C81A105KA12J	4	SMD Capacitor X6S(EIA) with Capacitance: 1.0uF Tol. 10%. Rated Voltage: 10Vdc
5	D1	VLMG1300-GS08	1	Green LED Indication - Discrete 2V 0603 (1608 Metric)
6	D2	VLMS1300-GS08	1	Red 631nm LED Indication - Discrete 2V 0603 (1608 Metric)
7	J2	22232041	1	0022232041 4 pin molex male header. Mates with 0022012047 receptacle housing and 0008560109 crimp terminal.
8	J3	22232041	1	0022232041 4 pin molex male header. Mates with 0022012047 receptacle housing and 0008560109 crimp terminal.
9	J4	22232041	1	0022232041 4 pin molex male header. Mates with 0022012047 receptacle housing and 0008560109 crimp terminal.
10	J5	22232041	1	0022232041 4 pin molex male header. Mates with 0022012047 receptacle housing and 0008560109 crimp terminal.
11	J6	22232021	1	0022232021 2 pin molex male header
12	J13	TC2030-CTX	1	Tag Connect footprint for ARM JTAG. 10 pin ARM Cortex Debug Connector.
13	L1	LQH2MCN150K02L	1	Inductor Power Chip Unshielded Wirewound 82uH 10% 1MHz Ferrite 0.09A 9.75Ohm DCR 0806 T/R

15	L2	LPS4018-222MRB	1	COILCRAFT - LPS4018-103MRB - INDUCTOR, 10UH, 20%, 0.9A,
16	LM1, R2	ERJ-2GE0R00X	2	0 Ohm resistor
17	R1, R4	ERJPA2F1003X	2	100kohm resistor 1/4W 0402
18	R3	ERJ-2GEJ151L	1	RES SMD 150 OHM 5% 1/10W 0402
19	R5, R6, R7, R8	ERJ-U02D5601X	4	RES THKFLM ANTI-SULFUR 0402 5.6K OHM 0.005 SMD
20	R9, R10, R11, R12, R13, R20	ERJU02D1002X	6	RES SMD 10 kOHM 0402
21	R14, R15	ERJ2RKF1001X	2	RES SMD 1 kOHM 0402
22	R16, R17, R18	ERJ-2GEJ220L	3	RES SMD 22 OHM 5% 1/10W 0402
23	S1	TL3301AF260QG	1	E-SWITCH - TL3301AF260QG - SWITCH, TACTILE SPST 50mA, SMD GULL WING
24	U1	LBAA0QB1SJ-296	1	RF Modules Type 1SJ 868/915MHz PCB Whip Flex Ant
25	U2	MAX17222ELT+T	1	Boost Switching Regulator IC Positive Adjustable 1.8V 1 Output 500mA (Switch) 6-WDFN
26	U3	DMC2400UV	1	DUAL N/P CHANNEL FET

Bibliography

- [1] Maurizio Mambrini. «Il vino come patrimonio nazionale». In: *L'Enologo* 3 (2016), pp. 44–46 (cit. on p. 1).
- [2] iXem Labs. *Chi Siamo*. URL: <https://ixem.wine/chi-siamo/> (cit. on p. 2).
- [3] Wikipedia. *LoRa*. URL: <https://en.wikipedia.org/wiki/LoRa> (cit. on p. 2).
- [4] Semtech. *What is LoRa®?* URL: <https://www.semtech.com/lora/what-is-lora> (cit. on p. 2).
- [5] LoRa Alliance. *What is LoRaWAN®Specification*. URL: <https://loralliance.org/about-lorawan/> (cit. on p. 3).
- [6] The Things Industries. *Home | The Things Stack for LoRaWAN*. URL: <https://www.thethingsindustries.com/docs/> (cit. on p. 3).
- [7] The Things Industries. *Quick Start | The Things Stack for LoRaWAN*. URL: <https://www.thethingsindustries.com/docs/getting-started/quick-start/> (cit. on p. 4).
- [8] The Things Industries. *Integrations | The Things Stack for LoRaWAN*. URL: <https://www.thethingsindustries.com/docs/integrations/> (cit. on p. 4).
- [9] Lorenzo Vangelista. «Frequency Shift Chirp Modulation: The LoRa Modulation». In: *IEEE Signal Processing Letters* 24.12 (Dec. 2017), pp. 1818–1821 (cit. on pp. 12, 13, 15).
- [10] Ghafour Amouzad Mahdiraji and Ahmad Fauzi Abas. «Advanced Modulation Formats and Multiplexing Techniques for Optical Telecommunication Systems». In: *Trends in Telecommunications Technologies*. Mar. 2010. ISBN: 978-953-307-072-8. DOI: 10.5772/8494 (cit. on p. 12).
- [11] Wikipedia. *Constellation Diagram*. URL: https://en.wikipedia.org/wiki/Constellation_diagram (cit. on p. 13).
- [12] Wikipedia. *Chirp*. URL: <https://en.wikipedia.org/wiki/Chirp> (cit. on p. 13).

- [13] Tapparel Joachim. «Complete Reverse Engineering of LoRa PHY». In: *EPFL* (2020) (cit. on p. 14).
- [14] *SX1276-7-8-9 data sheet*. Camarillo, USA: Semtech Corporation, May 2020 (cit. on p. 15).
- [15] S. Ghoslya. *LoRa Decoding*. URL: http://www.sghoslya.com/p/lor_a_9.html (cit. on p. 16).
- [16] The Things Industries. *Regional Parameters | The Things Network*. URL: <https://www.thethingsnetwork.org/docs/lorawan/regional-parameters/> (cit. on pp. 18–20).
- [17] Wikipedia. *Antenna (Radio)*. URL: [https://en.wikipedia.org/wiki/Antenna_\(radio\)](https://en.wikipedia.org/wiki/Antenna_(radio)) (cit. on p. 21).
- [18] Wikipedia. *Electromagnetic induction*. URL: https://en.wikipedia.org/wiki/Electromagnetic_induction (cit. on p. 21).
- [19] Wikipedia. *History of Maxwell's equations*. URL: https://en.wikipedia.org/wiki/History_of_Maxwell%27s_equations (cit. on p. 22).
- [20] C.A. Balanis. «Antenna theory: a review». In: *Proceedings of the IEEE* 80.1 (1992), pp. 7–23. DOI: 10.1109/5.119564 (cit. on pp. 22–25).
- [21] Institute of Chemistry - The Hebrew Institute of Jerusalem. *Heinrich Rudolf Hertz*. July 2004 (cit. on p. 22).
- [22] Wikipedia. *Guglielmo Marconi*. URL: https://en.wikipedia.org/wiki/Guglielmo_Marconi (cit. on p. 22).
- [23] Wikipedia. *Monopole antenna*. URL: https://en.wikipedia.org/wiki/Monopole_antenna (cit. on p. 26).
- [24] Wikipedia. *Inverted-F antenna*. URL: https://en.wikipedia.org/wiki/Inverted-F_antenna (cit. on p. 27).
- [25] Gerald Artner, Robert Langwieser, and Christoph Mecklenbräuker. «A MID dipole antenna in LDS technology». In: Nov. 2016, pp. 1–4. DOI: 10.1109/TELFOR.2016.7818832 (cit. on p. 28).
- [26] Nordic Semiconductor. *1/4 printed monopole antenna for 2.45GHz*. Jan. 2005. URL: https://infocenter.nordicsemi.com/pdf/nwp_008.pdf (cit. on p. 29).
- [27] MPL AG. *IP Ratings (Ingress Protection)*. URL: <https://www.mpl.ch/info/IPratings.html> (cit. on p. 31).
- [28] Dassault Systemes. *CST STUDIO SUITE*. URL: <https://www.3ds.com/products-services/simulia/products/cst-studio-suite/> (cit. on p. 36).

- [29] Constantinos Votis, Vasilis Christofilakis, and Panos Kostarakis. «Geometry Aspects and Experimental Results of a Printed Dipole Antenna». In: *IJCNS* 3 (Jan. 2010), pp. 204–207. DOI: 10.4236/ijcns.2010.32029 (cit. on pp. 41, 45).
- [30] Antenna Theory. *Inverted-F Antenna (IFA)*. URL: <https://www.antenna-theory.com/antennas/aperture/ifa.php> (cit. on p. 67).
- [31] *microSplatch™ ANT-868-uSP410 Embedded 868 MHz LPWA Antenna data sheet*. Merlin, OR, USA: Linx Technologies. URL: https://www.mouser.it/datasheet/2/238/LNNC_S_A0013017218_1-2551025.pdf (cit. on p. 87).
- [32] Shenzhen Aohua Electric Corporation Ltd. *Assembly Waterproof Plug*. URL: https://www.waterproofplug.com/assembly-waterproof-plug_c1 (cit. on p. 92).
- [33] Shenzhen Aohua Electric Corporation Ltd. *M16 Assembly Waterproof Plug*. URL: https://www.alibaba.com/product-detail/AOHUA-electric-wire-panel-mount-male_1600423717354.html?spm=a2700.shop_plgr.41413.19.56311647mB3R98 (cit. on pp. 92, 94).
- [34] Spelsberg. *Empty enclosureTK PC 1309-6-tm*. URL: <https://www.spelsberg.com/industrial-housing/with-/-without-metric-knock-outs/13700901/> (cit. on pp. 93, 96).